

UNIVERSITÄT
DUISBURG
ESSEN

Open-Minded

University of Duisburg-Essen

Department of Chemistry

UV resonance Raman spectroscopy of artificial
supramolecular ligands with laser excitation
wavelengths between 244 - 300 nm

Dissertation

to obtain the degree

Dr. rer. nat.

From:

Tim Henrik Holtum

born in Mönchengladbach

Essen, March 2022

The work for this dissertation was conducted within the framework of project A9 of the CRC 1093 "Supramolecular Chemistry on Protein" at the chair of Physical Chemistry I, University of Duisburg-Essen, in the group of Prof. Dr. Sebastian Schlücker in the period from April 2018 to November 2021.

Gutachter: Prof. Dr. Sebastian Schlücker
Prof. Dr. Thomas Schrader
Vorsitzender: Prof. Dr. Matthias Epple

Tag der Disputation: 25.05.2022

DuEPublico

Duisburg-Essen Publications online

UNIVERSITÄT
DUISBURG
ESSEN

Offen im Denken

ub | universitäts
bibliothek

Diese Dissertation wird via DuEPublico, dem Dokumenten- und Publikationsserver der Universität Duisburg-Essen, zur Verfügung gestellt und liegt auch als Print-Version vor.

DOI: 10.17185/duepublico/76020

URN: urn:nbn:de:hbz:465-20220607-105917-2

Alle Rechte vorbehalten.

Eidesstattliche Erklärung

Hiermit erkläre ich, dass die vorliegende Dissertation

„UV resonance Raman spectroscopy of artificial supramolecular ligands with laser excitation wavelengths between 244 - 300 nm“

selbstständig verfasst wurde und keine anderen außer den angegebenen Hilfsmitteln und Quellen benutzt wurden. Ich versichere, dass die vorliegende Dissertation nur in diesem und keinem anderen Promotionsverfahren eingereicht wurde.

Essen, March 2022

Tim Henrik Holtum

Abstract

Ultraviolet resonance Raman (UVRR) has been proven to be a powerful vibrational spectroscopic tool for a selective, sensitive, and label-free monitoring of peptides and proteins by artificial supramolecular ligands like guanidiniocarbonyl pyrroles (GCPs). However, so far the use of UVRR spectroscopy is limited by the UV-excited autofluorescence of the aromatic amino acids or even from the ligand itself which can mask the UVRR signal. Two ways to remedy the autofluorescence issue are explored with the help of a pulsed tunable laser system; spectral separation by shifting the excitation wavelength and temporal separation by a so called Kerr gate. Three different artificial ligands were studied, the two oxoanion binders GCP-ethylamide and its analogue guanidiniocarbonyl indole (GCI) ethylamide and the molecular tweezers CLR01 which binds selectively to lysine and arginine. The molecular tweezers signify an attempt to extend the scope of UVRR spectroscopy to a new class of supramolecular ligands. An UVRR spectrum of CLR01 could be acquired, however, the Raman signal of the phosphate groups, which are significant for binding, are not enhanced. For GCP-ethylamide an excitation study was performed between 244 nm and 310 nm to determine the laser excitation wavelength for an optimal UVRR signal with minimal impeding autofluorescence. The GCP analogue GCI exhibits a resonance around 244 nm which allows for autofluorescence-free acquisition of UVRR spectra. Spectral changes upon binding are first shown for two test molecules: the aromatic benzoic acid and the ubiquitous tripeptide RGD (arginylglycylaspartic acid). First tests were also carried out with the proteins bovine serum albumin (BSA) and Survivin. For a more generic approach a Kerr gate operating in the UV spectral range was set up. The separation of UVRR signal from autofluorescence is independent from the used laser excitation wavelength and can be applied for all molecules. The Kerr gate is demonstrated to work for a laser excitation wavelength of 280 nm.

All UVRR measurements were supported by density functional theory (DFT) calculations for a tentative assignment of spectral bands and to evaluate the relevance of the identified vibrational modes to binding. However, the calculations are mostly limited to the case of normal Raman scattering and do not consider the resonance case. To test applicability and accuracy of DFT UVRR calculations, an UVRR excitation study across the resonance was performed for anthracene and compared with TD-DFT calculations of RR including Herzberg-Teller vibronic coupling, bulk solvent effects and anharmonic corrections.

Kurzzusammenfassung

Die UV-Resonanz-Raman (UVR)-Spektroskopie hat sich als eine mächtige schwingungs-spektroskopische Methode für die selektive, sensitive und markierungsfreie Verfolgung der Erkennung von Peptiden und Proteinen durch künstliche supramolekulare Liganden wie Guanidiniocarbonylpyrrole (GCPs) erwiesen. Jedoch ist die Anwendbarkeit der UVR-Spektroskopie limitiert durch die UV-angeregte Autofluoreszenz (AF) von aromatischen Aminosäuren oder sogar von den Liganden selbst, die das UVR Signal überdecken kann. Mit der Hilfe eines gepulsten, durchstimmbaren Lasersystems wurden zwei Ansätze untersucht, um die Probleme verbunden mit der AF zu beheben; die spektrale Trennung durch das Verschieben der Anregungswellenlänge und die zeitliche Trennung mit einem sogenannten Kerr-Schalter. Drei unterschiedliche künstliche supramolekulare Liganden wurden untersucht, die zwei Oxoanionen-Binder GCP-ethylamid und dessen Analogon Guanidiniocarbonylindol (GCI)-ethylamid sowie die molekulare Pinzette CLR01, die selektiv an Lysin und Arginin binden. Die molekulare Pinzette steht dabei für den Versuch, die Anwendbarkeit der UVR-Spektroskopie um eine weitere Klasse von supramolekularen Liganden zu erweitern. Ein UVR-Spektrum der molekularen Pinzette CLR01 konnte aufgenommen werden, jedoch sind die Raman-Signale der Phosphat-Gruppen von CLR01, die signifikant an der Bindung teilnehmen, nicht Resonanz-verstärkt. Für GCP-ethylamid wurde eine Anregungsstudie zwischen 244 nm und 310 nm durchgeführt um die Anregungswellenlänge zu identifizieren, für die ein klares UVR-Signal mit minimaler Störung durch die AF erreicht wird. Das GCP-Analogon GCI besitzt eine Resonanz im Bereich von 244 nm, was eine AF-freie Messung von UVR-Spektren ermöglicht. Spektrale Änderungen des UVR-Signals, die bei Bindungsvorgängen auftreten, wurden zuerst für zwei Testmoleküle gezeigt: die aromatische Benzoesäure und das verbreitete Tripeptid RGD (Arginyl-Glycyl-Asparaginsäure). Erste Untersuchungen zur Bindung wurden auch für die Proteine Rinderserumalbumin (RSA) und Survivin durchgeführt. Für eine allgemeinere Methode zur AF-freien UVR-Spektroskopie wurde ein Kerr-Schalter im UV-Bereich aufgebaut. Die Trennung vom UVR-Signal von der AF ist unabhängig von der verwendeten Anregungswellenlänge und kann daher für jedes Molekül verwendet werden. Die Funktion des Kerr-Schalters wurde bei einer Anregungswellenlänge von 280 nm demonstriert.

Alle UVR-Messungen werden durch Dichtefunktionaltheorie (DFT)-Berechnungen unterstützt, um eine vorläufige Zuordnung der spektralen Banden zu ermöglichen und die Relevanz der jeweiligen Schwingungen in Bezug auf die Bindung zu evaluieren. Die Berechnungen sind jedoch zumeist beschränkt auf die normale Raman-Streuung und berücksichtigen keine Resonanz-Effekte. Um Anwendbarkeit und Genauigkeit von DFT-Berechnungen der UVR-Streuung zu testen, wurde eine Anregungsstudie im Bereich einer elektronischen Anregung von Anthracen durchgeführt und mit zeitabhängigen (TD)-DFT-Berechnungen verglichen, die Herzberg-Teller-Kopplung, Lösungsmiteleinflüsse und anharmonische Korrekturen berücksichtigen.

Contents

1	Introduction	2
2	Fundamentals and theoretical Background	4
2.1	Molecular Recognition by supramolecular ligands	4
2.2	Resonance Raman scattering	8
2.3	Kerr effect and Kerr gate	12
3	State of the art	16
3.1	UVRR on supramolecular ligands	16
3.2	Kerr gating	17
3.3	DFT calculations of resonance Raman scattering	19
4	Materials and Methods	21
4.1	Experimental UVRR setup	21
4.2	UV-Vis absorption spectroscopy	23
4.3	Sample preparation	23
4.4	DFT parameters	24
5	Results and Discussion	25
5.1	UVRR excitation study of anthracene	25
5.2	UVRR of the molecular tweezers CLR01	34
5.3	UVRR excitation study of GCP-ethylamide	37
5.4	Binding of the carboxylate binder GCI	40
5.4.1	Binding studies with the proteins BSA and Survivin	44
5.5	Implementation of a Kerr gate in the UV	47
6	Outlook	51
6.1	UVRR spectroscopy on anthracene	51
6.2	IR spectroscopy on molecular tweezers	52
6.3	UV Kerr gate	53
7	Summary	54
8	Bibliography	57
A	Example for calculating resonance Raman spectra with Gaussian	61
B	Calculated normal Raman spectra for GCI	66

1 Introduction

The process of molecular recognition, meaning the highly selective interaction of two or more molecules by noncovalent bonding mechanisms, plays a central role in many biological processes like enzymatic reactions [1], immune response [2], or biochemical signal transduction [3]. Understanding the underlying mechanisms of molecular recognition for target molecules or proteins is the first step necessary in understanding biological processes and can pave the way for drug development. One way to achieve this understanding can be found in the field of supramolecular chemistry, which is governed by the same noncovalent forces as molecular recognition. This is also the basis of the cooperative research center (CRC) 1093 "Supramolecular Chemistry on Proteins", where the cooperation of several research groups, rooted in chemistry and biology, work together with the aim of understanding and influencing biological processes. In this context, artificial supramolecular ligands provide a tool to specifically target parts of a protein, where the most basic building blocks target specific residues of an amino acid. Mostly these ligands are classified based on the charge of the target molecule and are grouped as either anion [4] or cation [5] binders. While most of these ligands work well in organic solvents, the application to biological systems requires operation in aqueous media. For this purpose there are two classes of artificial ligands used in the CRC which provide the necessary binding affinity in polar solvents. Ligands binding to anions are based on the guanidiniumcarbonyl pyrrole (GCP) group developed by Schmuck et al. [6] which specifically binds to oxoanions, like the carboxylate group of glutamates and aspartates. For binding to cations, the molecular tweezers developed by Klärner and Schrader et al. [7] are used, which selectively binds to arginine and lysine. In recent years UV resonance Raman (UVR) spectroscopy has been established as sensitive, selective, and label-free method for probing the binding constant of GCP complexes [8–11]. With the help of density functional theory methods, the Raman spectrum can be calculated and the vibrational modes which are likely to be involved in binding can be identified. These modes relevant to binding can then be monitored in the UVR spectra and from changes upon complexation the binding constant can be deduced. While first UVR binding studies were limited to tetrapeptides, it was later shown to work for the leucine zipper protein as well. However, the binding partner had to be carefully chosen, as UV-excited autofluorescence from the aromatic amino acids [12] can mask the UVR spectrum. This is also the reason why the molecular tweezers could not be studied with UVR so far, as autofluorescence from the aromatic backbone of the tweezers hinders measurements. Therefore, this thesis aims to extend UVR spectroscopy to a more generic method for measuring binding constants by implementing methods to avoid autofluorescence from impeding UVR measurements of the supramolecular ligands. For this the work is mainly focused around the use of a tunable pulsed ps-second laser system to spectrally separate the UVR signal from the autofluorescence signal by shifting the excitation wavelength. Additionally, a method for temporal separation of UVR and autofluorescence, a so-called Kerr gate, is set up and shown to work at

280 nm laser excitation wavelength.

In chapter 2 fundamentals on the utilized supramolecular ligands and physical effects are described. In subchapter 2.1 the supramolecular ligands used in this thesis are introduced and their binding mechanism is briefly explained. Then a short theoretical description for resonance Raman scattering (subchapter 2.2) and the Kerr effect (subchapter 2.3) is given. Chapter 3 is used to place the content of this thesis in the current state of research of UVRR on supramolecular ligands (subchapter 3.1) and Kerr gates with application to RR and the UV spectral range (subchapter 3.2). Additionally, a short overview over the methods implemented in the Gaussian 16 DFT software for calculating RR spectra is given (subchapter 3.3). In chapter 4 the experimental setup for the UVRR scattering and UV-Vis absorption measurements are described, followed by a short description on how samples for measurements were prepared and what parameters were used in DFT calculations.

Chapter 5 represents the main part of this thesis where the first four subchapters are focused on UVRR studies of four different target molecules. First the polyaromatic hydrocarbon anthracene is studied as a model molecule and compared to DFT calculated UVRR spectra in order to test the suitability of the current methods for predicting UVRR spectra. Then the molecular tweezers are studied with an excitation wavelength below to aromatic autofluorescence. In subchapter 5.3 the focus is shifted to the GCP-based ligands, with an excitation study of GCP-ethylamide between 244 nm and 310 nm. Finally, a GCP analogue GCI is studied which allows for aromatic autofluorescence-free UVRR measurements with an excitation wavelength of 244 nm. For a GCI-ethylamide ligand, binding is first shown for the small test molecules of benzoic acid and the RGD peptide, then tested for the two proteins of bovine serum albumin and Survivin. The last subchapter 5.5 contains the implementation of the Kerr gate in the UV spectral region. Afterwards, in chapter 6 a short outlook is given on possible changes for future experiments. Finally, a short summary of the thesis is given in chapter 7.

2 Fundamentals and theoretical Background

2.1 Molecular Recognition by supramolecular ligands

The basis of molecular recognition is given by the "lock and key" concept proposed by Fischer in 1894 [13]. It states that for the interaction of an enzyme with a substrate, the structure of the active site (lock) has to be matched by the structure of the substrate (key) for an interaction to take place. This concept was later extended by the so called "induced-fit" theory [14] in which the substrate itself first induces a structural change in the enzyme or protein, to enable binding according to the "lock and key" principle. The molecular recognition relies on the interaction of multiple reversible, non-covalent intermolecular forces, such as hydrogen bonding, electrostatic effect, $\pi - \pi$ interactions, or van der Waals forces. These concepts can also be found in the host-guest chemistry in supramolecular chemistry [15].

These similarities between biology and chemistry have been a central point for the works within the collaborative research center (CRC) 1093 "Supramolecular Chemistry on Proteins". The CRC strives to develop novel concepts for protein recognition and modulation by supramolecular ligands to investigate the underlying principles involved in the protein-ligand and possible protein-protein interactions (PPIs). Since most PPIs are based only on the interaction of a few amino acids at the protein interface, the so called "hot spot", amino acid specific binding motifs are a promising tool for the coordination of the supramolecular ligand on the protein [16].

Within the CRC two main classes of binding motifs are used, one binding to the acidic amino acid side chains aspartate and glutamate and the other one binding to the basic amino acid side chains lysine and arginine. Both these classes will shortly be described in the following paragraphs.

Artificial aspartate and glutamate binder

The anion binder mainly used by the CRC is the guanidiniocarbonyl pyrrole (GCP) motif developed by C. Schmuck in 1999 [6, 17]. As an example, the structure of GCP ethyl amide is shown in figure 2.1. GCP is based on the guanidinium cation (shown in blue) which was already known for the binding to oxoanions, like carboxylate or phosphate, in organic solvents [4]. The guanidinium was extended by a pyrrole (red) linked by a carbonyl group (brown). The NH of the pyrrole provides an additional donor site for hydrogen bonding to increase the binding affinity. On the other side of the pyrrole other side chains, for example amino acids or like in figure 2.1 an ethyl group, can be linked by an amide bond (black). The NH of the amide provides yet another donor for hydrogen bonding which, together with the other hydrogen bonding sites from the pyrrole and the guanidinium, forms the carboxylate binding site (CBS). The complexation of GCP ethyl amide with a carboxylate is schematically displayed in figure 2.2. An additional hydrogen bond between the guanidinio- and carbonyl group helps to stabilize the planar conformation of the

GCP favorable to binding [18–20]. With the increased binding affinity, GCP proves to be an effective binder to oxo-anions even in polar, aqueous media [21], which is necessary for biological applications. However, another factor needed for biological application is specificity, since GCP will potentially bind to any free oxoanion. The required specificity can be achieved by further functionalization at the amide bond site (exchanging the ethyl amide (black) in figure 2.1). For example, an amino acid chain, complementary to the binding site, can be used which has been shown for the C-terminus of the amyloid β -peptide [17, 22]. Another option is to attach multiple GCP units to a scaffold which sterically restricts the GCP units in such a way that all GCP units can only bind at a specific spot on the protein [23].

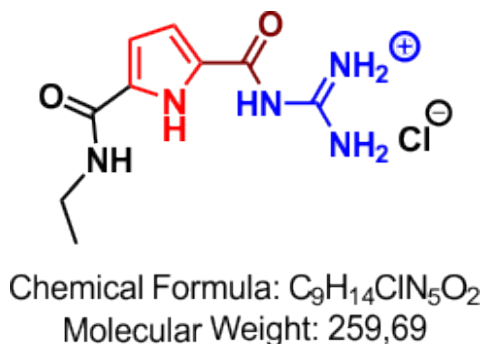


Figure 2.1: Schematic representation of the chemical structure of the guanidiniocarbonyl pyrrole ethyl amide with the substructures marked in different colors: ethyl amide in black, pyrrole ring in red, carbonyl in brown, and guanidinio in blue.

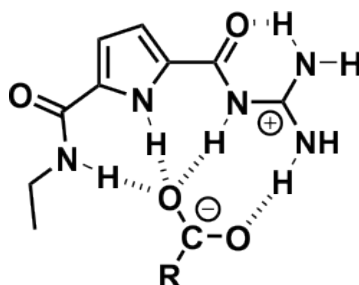
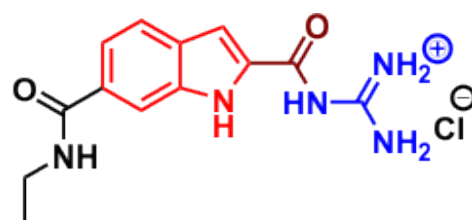


Figure 2.2: Schematic representation of the complexation of GCP ethyl amide with a carboxylate. Hashed bonds indicate hydrogen bonding.

Another variant of the GCP binding motif is guanidiniocarbonyl indole (GCI), for which the pyrrole ring has been exchanged with an indole ring [19, 20, 24]. The structure of GCI ethyl amide is shown in figure 2.3, with different colors for the different functional groups. The CBS is similar to that of GCP with the NH group from the indole replacing that of the pyrrole. However, the NH of the amide bond is too far away and will no longer be a part of the CBS. This will most likely lead to a somewhat decreased binding affinity. On the other hand, the indole group changes the optical properties of GCI as compared to GCP. Since indole is known to be fluorescent, e.g. in the aromatic amino acid tryptophan [12], GCI might be used as an intrinsic fluorescent marker in binding studies.



Chemical Formula: $C_{13}H_{16}ClN_5O_2$
Molecular Weight: 309,75

Figure 2.3: Schematic representation of the chemical structure of the guanidiniocarbonyl indole ethyl amide with the substructures marked in different colors: ethyl amide in black, indole ring in red, carbonyl in brown, and guanidinio in blue.

Artificial lysine and arginine binder

The binding motif selective to lysine and arginine is the molecular tweezers developed by Schrader and Klärner [7]. The structure of CLR01 is shown in figure 2.4 in a 2D (top) and 3D (bottom) representation. CLR01 consists of alternating connected benzene (red) and norbornadiene (blue) rings, adorned with two phosphate groups (black) on the central benzene ring. Due to the norbornadiene, CLR01 folds up to a tweezer like structure in 3D, hence the name molecular tweezers. The π -systems of the benzene rings lead to a torus-shaped electron rich cavity inside of the tweezers. The added phosphate groups make water solubility possible.

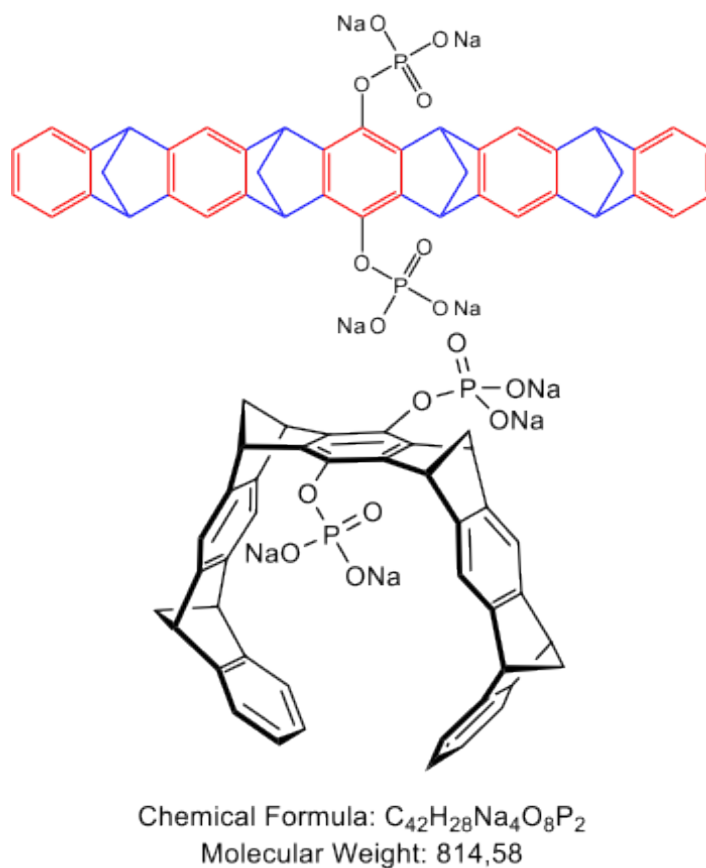


Figure 2.4: Schematic representation of the chemical structure of the molecular tweezers CLR01. On the top the structure is shown in 2D with the substructures marked with different colors: benzene rings in red, norbornadiene in blue, and phosphate groups in black. The bottom shows the 3D-structure.

For arginine or lysine, the side chain is threaded into the cavity of the tweezer while the positively charged end group is pointing towards one of the anionic phosphate groups. This kind of complexation is shown in figure 2.5 as the result from a Monte Carlo simulation of the binding between CLR01 and Ts-Arg-OEt, as an arginine target [7].

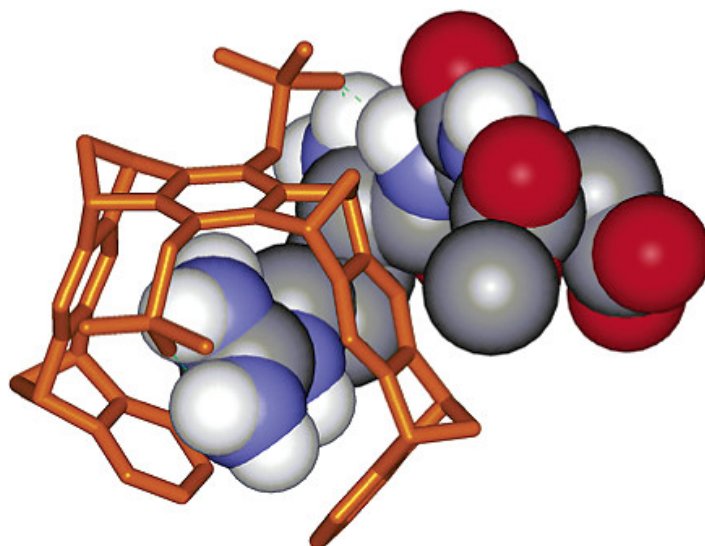


Figure 2.5: Monte Carlo simulation of the complex between molecular tweezer CLR01 and Ts-Arg-OEt. The arginine side chain is enclosed by the tweezer cavity and the phosphates coordinates with the amino and guanidino group. Reprinted with permission from [7]. ©2005 American Chemical Society.

The molecular tweezers themselves are already able to selectively influence protein interactions like the aggregation of amyloid β -protein associated with Alzheimer disease [25] or PPIs of 14-3-3 proteins [26,27]. Additionally, they are able to penetrate the cell [28], which is already a big step towards drug research. However, like the GCP motif, the molecular tweezers can be modified with additional side chains in order to enhance selectivity towards specific proteins, like Survivin [29]. The functionalization allows for a more flexible and specialized approach.

2.2 Resonance Raman scattering

Raman scattering is based on the Raman effect, which was first described by Smekal in 1923 [30] and later on experimentally discovered by Raman in 1928 [31]. It is a form of inelastic light scattering in which light is scattered at a different frequency than that of the incident light. The inelastic light scattering can be further differentiated into two categories: light scattered with a lower optical frequency, called Stokes scattering, and light scattered with a higher optical frequency, called Anti-Stokes scattering.

In classical theory, the Raman effect can be explained in the following way [32]: An electromagnetic wave \vec{E} incident on a molecule will create an induced dipole moment \vec{p}_{ind} . Considering only the first order interaction, \vec{p}_{ind} can be written as:

$$\vec{p}_{ind} = \alpha \cdot \vec{E}, \quad (2.1)$$

with the polarizability tensor α . The polarizability is a second rank tensor and describes the response of a material or molecule to an external field. In general, the polarizability depends on the nuclear coordinates and therefore on the molecular vibrations. To approximate the change of the polarizability due to vibrations of the molecule, each component of the polarizability tensor can be expanded in a Taylor series with respect to the normal coordinates of the vibrations:

$$\alpha_{\rho\sigma} = (\alpha_{\rho\sigma})_0 + \sum_k \left(\frac{\partial \alpha_{\rho\sigma}}{\partial Q_k} \right)_0 Q_k + \frac{1}{2} \sum_{k,l} \left(\frac{\partial^2 \alpha_{\rho\sigma}}{\partial Q_k \partial Q_l} \right)_0 Q_k Q_l \dots \quad (2.2)$$

where the subscript 0 indicates the evaluation at the equilibrium position, Q_k, Q_l are normal coordinates of the vibrations and the summations are over all normal coordinates. For a given normal coordinate k associated to the normal mode with frequency ω_k , the polarizability tensor can be written in first order as:

$$\alpha_k = \alpha_0 + \alpha'_k Q_k \quad (2.3)$$

where α_0 consists of the components $(\alpha_{\rho\sigma})_0$ and α'_k consists of the components $(\partial \alpha_{\rho\sigma} / \partial Q_k)_0$. Since the evaluation is close to the equilibrium position, a simple harmonic motion can be assumed for the normal coordinate Q_k in the form of:

$$Q_k = \frac{1}{2} Q_{k0} \left(e^{-i(\omega_k t + \delta_k)} + e^{i(\omega_k t + \delta_k)} \right) \quad (2.4)$$

with the amplitude Q_{k0} , the time t and the phase δ_k .

For the incident electric field \vec{E} the form of plane wave can be assumed:

$$\vec{E} = \frac{1}{2} \vec{E}_0 \left(e^{-i\omega_0 t} + e^{i\omega_0 t} \right) \quad (2.5)$$

where ω_0 is the optical frequency. Combining equations 2.3, 2.4, and 2.5 a new formulation for the induced dipole moment is possible:

$$\vec{p}_{ind} = \frac{1}{2} \alpha_0 \vec{E}_0 \left(e^{-i\omega_0 t} + e^{i\omega_0 t} \right) + \frac{1}{4} \alpha'_k \vec{E}_0 Q_{k0} \left(e^{-i[(\omega_0 \pm \omega_k)t \pm \delta_k]} + e^{i[(\omega_0 \pm \omega_k)t \pm \delta_k]} \right). \quad (2.6)$$

Or, in terms of trigonometric functions, it can be written as

$$\vec{p}_{ind} = \underbrace{\alpha_0 \vec{E}_0 \cos(\omega_0 t)}_{\text{Rayleigh}} + \frac{1}{2} \alpha'_k \vec{E}_0 Q_{k0} \left\{ \underbrace{\cos[(\omega_0 - \omega_k)t - \delta_k]}_{\text{Stokes}} + \underbrace{\cos[(\omega_0 + \omega_k)t + \delta_k]}_{\text{Anti-Stokes}} \right\}. \quad (2.7)$$

The first term marks the elastic scattering with the same frequency ω_0 as the incident frequency, also known as Rayleigh scattering. The second term describes the Raman scattering, which consists of two terms. The first term in the brackets describes Stokes scattering for which the optical frequency is red-shifted by the frequency of the k -th vibrational mode $(\omega_0 - \omega_k)$ and the second term describes Anti-Stokes scattering for which the optical frequency is blue-shifted $(\omega_0 + \omega_k)$ by the same vibrational frequency. Since the Raman term linearly depends on the derivative of polarizability tensor α'_k , it must be non-zero for Raman scattering to occur. For a given mode to be Raman-active that means the polarizability needs to change during vibration when passing through the equilibrium position ($Q_k = 0$).

While the classical description of the Raman effect proves useful for understanding normal Raman scattering, it is not applicable in the case of resonance Raman (RR) scattering, which was mainly

utilized in this thesis. If the excitation frequency is close to that of an electronic transition of the molecule, the Raman signal for specific modes can be greatly enhanced. In order to understand the selection criteria for RR scattering, a quantum mechanical approach is needed. The RR scattering process can be described as the transition from an initial state i to an intermediate state r followed by another transition to the final state f . In a sum-over-states formalism, the components of the polarizability tensor for the transition from initial to final state can be written as

$$(\alpha_{\rho\sigma})_{fi} = \frac{1}{\hbar} \sum_{r \neq i, f} \left\{ \frac{\langle f | \hat{p}_\rho | r \rangle \langle r | \hat{p}_\sigma | i \rangle}{\omega_{ri} - \omega_0 - i\Gamma_r} + \frac{\langle f | \hat{p}_\sigma | r \rangle \langle r | \hat{p}_\rho | i \rangle}{\omega_{ri} + \omega_0 + i\Gamma_r} \right\} \quad (2.8)$$

with the dipole moment operators \hat{p}_ρ and \hat{p}_σ , the difference frequency between the intermediate and initial state $\omega_{ri} = \omega_r - \omega_i$, and the damping constant Γ_r , which is related to the lifetime of the state r .

Following the Born-Oppenheimer approximation, electronic and nuclear states are weakly coupled and can be separated. For example, the intermediate state r can be separated in the following way:

$$|r\rangle = |e^r v^r\rangle = |e^r\rangle |v^r\rangle \quad (2.9)$$

where e^r and v^r are the electronic and vibrational quantum number for state r , respectively.

In the case of vibrational RR scattering some more simplifications can be employed. Near resonance ($\omega_{ri} \approx \omega_0$), the second term of 2.8 can be neglected, as it will be significantly smaller than the first term. Only considering vibrational scattering restricts the electronic state i and f to the ground state ($e^g = e^i = e^f$). This allows to rewrite equation 2.8 in the following way:

$$(\alpha_{\rho\sigma})_{e^g v^f : e^g v^i} = \frac{1}{\hbar} \sum_{e^r v^r \neq e^g v^i, e^g v^f} \frac{\langle v^f | \langle e^g | \hat{p}_\rho | e^r \rangle | v^r \rangle \langle v^r | \langle e^r | \hat{p}_\sigma | e^g \rangle | v^i \rangle}{\omega_{e^r v^r : e^g v^i} - \omega_0 - i\Gamma_{e^r v^r}}. \quad (2.10)$$

In principle, the Born-Oppenheimer approximation allows to separate the pure electronic dipole moments ($(p_\rho)_{e^g e^r} = \langle e^g | \hat{p}_\rho | e^r \rangle$) from the summation over the vibrational states. However, the transition dipole moment can exhibit a slight dependence on the nuclear coordinates, for example if the symmetry of a molecule changes due to a vibration [33]. This dependence can be introduced by a Taylor expansion of the electronic Hamiltonian \hat{H}_e with regards to the normal coordinates of vibration Q around the equilibrium position Q_0 :

$$\hat{H}_e(Q) = (\hat{H}_e)_0 + \sum_k \left(\frac{\partial \hat{H}_e}{\partial Q_k} \right)_0 Q_k + \frac{1}{2} \sum_{k,l} \left(\frac{\partial^2 \hat{H}_e}{\partial Q_k \partial Q_l} \right)_0 Q_k Q_l + \dots \quad (2.11)$$

with the normal coordinates Q_k, Q_l, \dots . Considering only the first order, this will change the electronic state e^r to a new perturbed state $e^{r'}$ which involves the coupling of the electronic state

e^r to a different electronic state e^s . For example the perturbed *ket* state can be written as

$$|e^{r'}(Q_0)\rangle = |e^r(Q_0)\rangle + \frac{1}{\hbar} \sum_{e^s \neq e^r} \sum_k \frac{h_{e^s e^r}^k}{\omega_{e^r} - \omega_{e^s}} Q_k |e^s(Q_0)\rangle \quad (2.12)$$

where $h_{e^s e^r}^k$ is defined by

$$h_{e^s e^r}^k = \langle \Psi_{e^s}(Q_0) | (\partial \hat{H}_e / \partial Q_k)_0 | \Psi_{e^r}(Q_0) \rangle, \quad (2.13)$$

and can be interpreted as a coupling integral for the vibronic coupling of the electronic states e^r and e^s . If this perturbation is applied to equation 2.10, an expression for the components of the polarizability tensor including weak vibronic coupling can be obtained. Following the representation scheme as introduced by Albrecht [34], the expression will be given as:

$$(\alpha_{\rho\sigma})_{e^g v^f; e^g v^i} = A + B + C + D \quad (2.14)$$

with

$$A = \frac{1}{\hbar} (p_\rho)_{e^g e^r}^0 (p_\rho)_{e^r e^g}^0 \sum \frac{\langle v_g^f | v_r^r \rangle \langle v_r^r | v_g^i \rangle}{\omega_{e^r v^r; e^g v^i} - \omega_0 - i\Gamma_{e^r v^r}} \quad (2.15)$$

$$B = \frac{1}{\hbar^2} (p_\rho)_{e^g e^s}^0 \frac{h_{e^s e^r}^k}{\omega_{e^r} - \omega_{e^s}} (p_\rho)_{e^r e^g}^0 \sum \frac{\langle v_g^f | Q_k | v_r^r \rangle \langle v_r^r | v_g^i \rangle}{\omega_{e^r v^r; e^g v^i} - \omega_0 - i\Gamma_{e^r v^r}} \quad (2.16)$$

$$+ \frac{1}{\hbar^2} (p_\rho)_{e^g e^r}^0 \frac{h_{e^r e^s}^k}{\omega_{e^r} - \omega_{e^s}} (p_\rho)_{e^s e^g}^0 \sum \frac{\langle v_g^f | v_r^r \rangle \langle v_r^r | Q_k | v_g^i \rangle}{\omega_{e^r v^r; e^g v^i} - \omega_0 - i\Gamma_{e^r v^r}}$$

$$C = \frac{1}{\hbar^2} \frac{h_{e^g e^t}^k}{\omega_{e^g} - \omega_{e^t}} (p_\rho)_{e^t e^r}^0 (p_\rho)_{e^r e^g}^0 \sum \frac{\langle v_g^f | Q_k | v_r^r \rangle \langle v_r^r | v_g^i \rangle}{\omega_{e^r v^r; e^g v^i} - \omega_0 - i\Gamma_{e^r v^r}} \quad (2.17)$$

$$+ \frac{1}{\hbar^2} (p_\rho)_{e^g e^r}^0 (p_\rho)_{e^r e^t}^0 \frac{h_{e^t e^g}^k}{\omega_{e^g} - \omega_{e^t}} \sum \frac{\langle v_g^f | v_r^r \rangle \langle v_r^r | Q_k | v_g^i \rangle}{\omega_{e^r v^r; e^g v^i} - \omega_0 - i\Gamma_{e^r v^r}}$$

$$D = \frac{1}{\hbar^3} (p_\rho)_{e^g e^s}^0 \frac{h_{e^s e^r}^k h_{e^r e^s'}^{k'}}{(\omega_{e^r} - \omega_{e^s})(\omega_{e^r} - \omega_{e^s'})} (p_\rho)_{e^s' e^g}^0 \sum \frac{\langle v_g^f | Q_k | v_r^r \rangle \langle v_r^r | Q_k' | v_g^i \rangle}{\omega_{e^r v^r; e^g v^i} - \omega_0 - i\Gamma_{e^r v^r}} \quad (2.18)$$

where for different electronic states the exclusions $e^r \neq e^g, e^s, e^{s'}$ and $e^t \neq e^g$ apply (see also figure 2.6).

The *A*-term describes the unperturbed system without any vibronic coupling. This term is also referred to as the Franck-Condon-term, since it is equal to the description derived from the Franck-Condon principle [35, 36]. The pure electronic transition dipoles $(p_\rho)_{e^g e^r}^0$ and $(p_\rho)_{e^r e^g}^0$ are zero, except for allowed dipole transitions. Therefore, only dipole-allowed transitions can yield a RR signal. The corresponding electronic transition is schematically displayed in figure 2.6 (a), together with the transitions related to the other terms. The sum signifies the overlap of the vibrational states and is also referred to as the Franck-Condon factor.

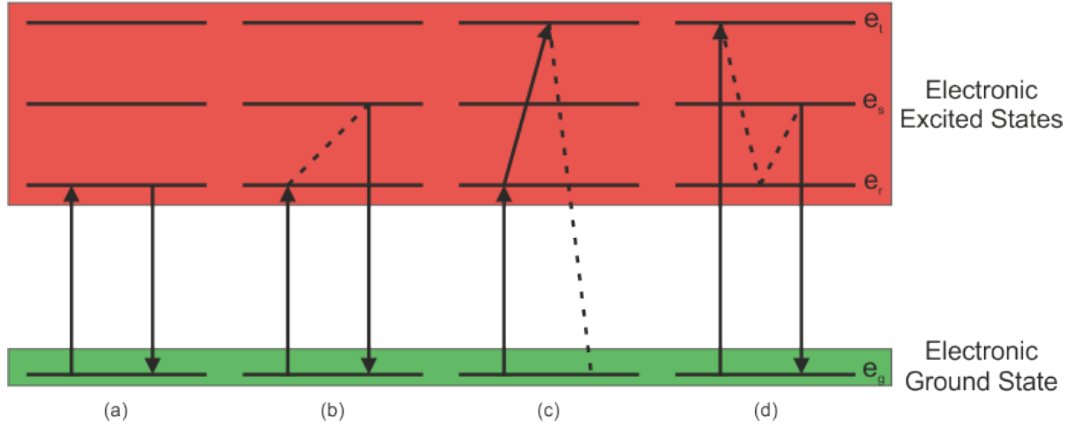


Figure 2.6: Schematic representation of the electronic transitions that are possible during RR scattering when considering Herzberg-Teller coupling: (a) pure dipole transition of the A -term; (b) transitions of the first term of the B -term; (c) transitions of the first term of the C -term; (d) transitions of the D -term.

The B -, C -, and D -term all arise from the vibrational coupling suggested by Herzberg and Teller [33], and are therefore also referred to as Herzberg-Teller terms. For the B -term there is a dipole transition, followed by vibronic coupling, followed by another dipole transition (cf. figure 2.6(b)). Both of the dipole transitions are back to the ground state, which means, that as for the A -term only dipole-allowed transitions from the ground state can contribute to a signal. The vibrational part includes not only the overlap integral ($\langle v_r^r | v_g^i \rangle$) but also a vibrational transition integral via Q_k ($\langle v_g^f | Q_k | v_r^r \rangle$). Since the transition integrals are along the axis of a normal mode Q_K , only fundamentals can be accessed by the B -term.

The C -term is defined by vibronic coupling of an excited state to the ground state (dashed line in figure 2.6(c)) as compared to the B -term where vibronic coupling of two excited states occurs. This allows for coupling of the ground state to an excited state which is dipole-forbidden. The vibrational component is the same as for the B -term.

The D -term relates to the vibronic coupling of the excited electronic state e^r to two other electronic excited states (cf. figure 2.6(d)). The vibrational part features two transition integrals. This can give rise to either first overtones (in case of $k = k'$) or combination modes (in case of $k \neq k'$).

2.3 Kerr effect and Kerr gate

A particular nonlinear optical effect, which is used in this thesis, is the optical Kerr effect. The Kerr effect was discovered in 1875 by John Kerr [37]. It is the change of the refractive index of a material induced by an electric field. This phenomenon can be utilized to create an optical gate, called Kerr gate, if a strong linearly polarized laser beam at frequency Ω is used to create a birefringence in a normally isotropic Kerr medium. As a consequence the Kerr medium acts as a wave plate to a second weaker linearly polarized laser beam at frequency ω where the polarization is rotated by 45° with respect to the first beam. Together with crossed polarizers before and after the Kerr medium, an optical gate can be created. A more detailed description of the setup and working principle of such a Kerr gate will be given in chapter 3.2 and the setup used in this thesis

is described in chapter 5.5. In this chapter a brief theoretical description of the optical Kerr effect as a nonlinear process will be given.

The Kerr effect is a nonlinear optical phenomenon. This means that the description of the induced dipole moment with a linear dependency on the electric field (as for the Raman effect, see equation 2.1) is no longer valid and higher orders of the electric field have to be considered. The induced dipole moment takes the form:

$$\vec{p}_{ind} = \chi_1 \vec{E} + \chi_2 \vec{E}^2 + \chi_3 \vec{E}^3 + \dots \quad (2.19)$$

where χ_1 , χ_2 , and χ_3 are the first, second, and third order susceptibility, respectively. An equivalent description with higher order polarizability tensors α is possible as well [38]. The polarizability describes the material response on a molecular level which is appropriate for the Raman effect, but requires the accurate knowledge of the local electric field. The susceptibility on the other hand is a macroscopic property to describe the material response of the bulk material which allows for a simpler description in terms of the applied field [39].

The most relevant case for this thesis is the Kerr effect in isotropic media which allows for considerable simplifications. Isotropic media possess inversion symmetry which means the second order susceptibility (χ_2) is zero as a spatial inversion of the electric field has to result in a spatial inversion of the induced dipole ($\vec{p}_{ind}(-\vec{E}) = -\vec{p}_{ind}(\vec{E})$). Additionally, the description of χ_3 can be reduced from the 81 elements of the fourth rank tensor to only three independent elements χ_3^{1122} , χ_3^{1212} , and χ_3^{1221} [40]. The superscripts 1 and 2 denote the spatial directions (e.g. for a Cartesian system, $1 = x$ and $2 = y$ for waves propagating in the z -direction).

In general, all effects involving χ_3 can be described as so called four-wave mixing process, meaning that by the interaction of three photons with frequencies ω_1 , ω_2 , and ω_3 , a fourth one is generated at the frequency $\omega_4 = \omega_1 + \omega_2 + \omega_3$ and the susceptibility is written as $\chi_3(-\omega_4, \omega_1, \omega_2, \omega_3)$. This form of the susceptibility is unique for certain processes and is used as a descriptor for the process, e.g. $\chi_3(-3\omega, \omega, \omega, \omega)$ for third harmonic generation. Note that the frequencies can be either positive or negative, where positive frequencies indicate incoming photons and negative frequencies reference outgoing photons.

The susceptibility for the Kerr effect in an isotropic medium, where a weak probe beam of frequency ω will be affected by the birefringence induced by an intense beam of linearly polarized light at frequency Ω , can be written as $\chi_3(-\omega, \omega, \Omega, -\Omega)$. In these terms, the i -th component of the nonlinear polarization $\vec{p}_3 = \chi_3 \vec{E}^3$ can be written as

$$\begin{aligned} (p_3)_i &= 6\chi_3^{1122}(-\omega, \omega, \Omega, -\Omega)E_i(\omega)E_j(\Omega)E_j^*(\Omega) \\ &\quad + 6\chi_3^{1212}(-\omega, \omega, \Omega, -\Omega)E_j(\omega)E_i(\Omega)E_j^*(\Omega) \\ &\quad + 6\chi_3^{1221}(-\omega, \omega, \Omega, -\Omega)E_j(\omega)E_j(\Omega)E_i^*(\Omega) \end{aligned} \quad (2.20)$$

where i and j are the Cartesian indices [40]. From this expression it can be seen that the strong field $\vec{E}(\Omega)$ creates a change in the susceptibility experienced by the weaker field $\vec{E}(\omega)$. The overall susceptibility in the form of a linear susceptibility χ_1 can be expressed as $\vec{p}_{ind} = (\chi_1 + \delta\chi) \vec{E}(\omega)$,

where the components of $\delta\chi$ are defined as:

$$\begin{aligned}\delta\chi^{ij} &= 6\chi_3^{1122}(-\omega, \omega, \Omega, -\Omega)|\vec{E}(\Omega)|^2\delta^{ij} \\ &+ 6\chi_3^{1212}(-\omega, \omega, \Omega, -\Omega)E_i(\Omega)E_j^*(\Omega) \\ &+ 6\chi_3^{1221}(-\omega, \omega, \Omega, -\Omega)E_j(\Omega)E_i^*(\Omega).\end{aligned}\quad (2.21)$$

This induced susceptibility creates a change in the refractive index n for the probe beam $\vec{E}(\omega)$. With the relation $n = \sqrt{1 + \chi}$, the change in refractive index for parallel polarization is as follows:

$$\delta n_{\parallel} = \frac{3}{n_0} [\chi_3^{1122}(-\omega, \omega, \Omega, -\Omega) + \chi_3^{1212}(-\omega, \omega, \Omega, -\Omega) + \chi_3^{1221}(-\omega, \omega, \Omega, -\Omega)] |\vec{E}(\Omega)|^2 \quad (2.22)$$

and for perpendicular polarization

$$\delta n_{\perp} = \frac{3}{n_0} \chi_3^{1122}(-\omega, \omega, \Omega, -\Omega) |\vec{E}(\Omega)|^2. \quad (2.23)$$

Overall this leads to a net difference of the refractive index in direction of the polarization of the strong field $\vec{E}(\Omega)$ of

$$\Delta n = \frac{3}{n_0} [\chi_3^{1212}(-\omega, \omega, \Omega, -\Omega) + \chi_3^{1221}(-\omega, \omega, \Omega, -\Omega)] |\vec{E}(\Omega)|^2 = n_2 I(\Omega) \quad (2.24)$$

which is also referred to as the nonlinear refractive index n_2 proportional to the intensity $I(\Omega)$. Overall, the Kerr effect in isotropic media only depends on two elements of the χ_3 tensor: χ_3^{1212} and χ_3^{1221} .

However, since the susceptibility only describes macroscopic effects, it does not give insight on the mechanisms involved in the interactions. A full description of the underlying effects would exceed the scope of this thesis, but a short overview will be given.

In general, electronic and nuclear contributions can be differentiated. The electronic contribution can be understood in terms of an distortion of the electronic cloud by the applied field and can be approximated by introducing anharmonicity into the model of harmonic oscillator [39, 41]. For the pulse durations in the order of picoseconds used in this thesis, the electronic contribution can be seen as instantaneous. In essence, the electronic contribution to the induced dipole ($\vec{p}_{ind}^e(t)$) can then be written as

$$\vec{p}_{ind}^e(t) = \frac{\sigma}{2} \vec{E}^3(t) \quad (2.25)$$

where σ is a material parameter tied to the linear susceptibility [42, 43].

For the nuclear contributions, there are more possible processes involved, for example molecular reorientation or molecular redistribution. For all these nuclear contributions, the induced dipole moment can be written in the form

$$\vec{p}_{ind}^n(t) = \vec{E}(t) \int a(t-s) \vec{E}^2(s) ds + \int \vec{E}(t) \cdot \vec{E}(s) b(t-s) \vec{E}(s) ds \quad (2.26)$$

where a and b are the nuclear response functions for the isotropic and anisotropic contributions,

respectively. Here the integrals have to be considered since the molecular processes are in general slower than the electronic ones and the response is no longer quasi-instantaneous [42, 43].

As it can be expected, the nuclear contributions are mainly relevant in liquids, where it can prove the dominant mechanism, as for example for carbon disulfide (CS_2) [42, 43]. In optical glasses, however, the nuclear contributions are small and can mostly be neglected [43, 44].

3 State of the art

3.1 UVRR on supramolecular ligands

In the biochemical context, UVRR mainly focuses on protein and peptides as subjects of study [45–47]. This is due to the resonance of the amide bond in the deep UV region (around 190 nm). Therefore the amide bands are enhanced and changes in the protein secondary structure can be monitored. However, this method will always yield signal from the entire protein, which can make the assignment of observed changes challenging. Another approach is to use a specific chromophore which is selectively enhanced in UVRR spectroscopy. This allows for high selectivity, as only the chromophore will produce significant UVRR signal. This allows to monitor changes in the direct surrounding inducing changes in the UVRR spectrum of the chromophore. In this context a ligand-based UVRR technique was introduced within the CRC 1093 in order to measure and evaluate the binding between molecules. For this technique the binding motif of the ligand acts as the chromophore for the UVRR spectroscopy, which essentially allows for a label-free detection method. So far, the studies have been focused on artificial supramolecular ligands based on the GCP motif (compare chapter 2.1). The experiments are UVRR spectroscopic titration measurements in which the concentration of the GCP ligand is kept constant and the peptide/protein concentration is continuously increased. Since the peptide/protein is not in electronic resonance with the excitation laser wavelength, its signal is negligible and the UVRR signal of the GCP motif should remain constant, apart from changes induced by the binding. After proper data processing by smoothing, background correction, and normalization, the spectra can be analyzed by multivariate techniques such as non-negative matrix factorization (NMF) [9,10,48] or multivariate curve resolution alternating least squares (MCR-ALS) [11]. In this fashion the ratio of bound to unbound ligand can be determined and through curve fitting with a sigmoidal function the binding constants can be determined which are comparable to those determined with other methods such as UV/Vis absorption spectroscopic titration [9].

The result of these binding studies can then be further used as input data for molecular docking simulation which yield the most likely structure of the ligand protein complex. This was shown for the binding of a trivalent GCP based ligand with the leucine zipper motif [11]. However, the leucine zipper protein had to be carefully chosen for this applications, as it only incorporates one aromatic amino acid. This is because the aromatic amino acids, as well as other aromatic compounds, generate autofluorescence in the range from ca. 260-420 nm due to the UV excitation [12]. If the UV-excited autofluorescence spectrally coincides with the UVRR signal, it can easily mask the latter.

UV-excited autofluorescence constitutes a problem for the other prominent ligand used in the CRC 1093, that is the supramolecular tweezers, as well. The molecular tweezers, which bind specifically to lysines and arginines, have shown great promise in the interaction and inhibition of

several proteins and are even known to be able to enter cells [28, 29, 49].

Unfortunately, the molecular tweezers have so far not been measured by UVR spectroscopy, since the UV-excited autofluorescence of the molecular tweezers itself masks the UVR spectrum for the excitation wavelengths of 275 nm and 266 nm which were used for the GCP-based ligands.

To avoid this disturbing UV-excited autofluorescence, both from protein and ligand, two different methods can be explored. The first option is to shift the excitation wavelength to lower wavelengths. This spectrally separates the UVR signal from the autofluorescence. However, this demands another relevant electronic resonance from the ligand or molecule at lower wavelengths in order to meet the required resonance condition for UVR scattering.

The second method is to exploit the different timescales of UVR scattering and fluorescence emission. Whereas UVR scattering is a quasi instantaneous process, fluorescence is a longer process with rise times of up to nanoseconds [50]. For pulsed excitation, this allows to separate the Raman scattering from the fluorescence signal by means of a temporal gating technique, as for example Kerr gating, which will be described in the following chapter. The benefit of this method would be completely generic, as there is no restriction for the proteins or ligands of interest.

3.2 Kerr gating

One way to separate the UVR signal from fluorescence is to reject the fluorescence on the temporal scale as it is longer lived compared to the quasi instantaneous UVR scattering. To achieve this kind of temporal rejection a so called Kerr gate which uses the Kerr effect (see chapter 2.3), i. e. an electric-field-induced birefringence. By focusing a sufficiently strong pulsed laser beam in an optical medium a change in the refractive index along the polarization axis is induced during the pulse. If this Kerr-effect-inducing pulse (Kerr pulse or gating pulse) is temporally and spatially overlapped with the UVR signal, the optical axis of the UVR signal is rotated as long as polarization of the Kerr pulse and UVR signal are not parallel. With the help of cross-polarizers the turned UVR signal can then be separated from the fluorescence signal.

The first application of a Kerr gate for resonance Raman scattering with a gating pulse of ca. 3 ps has been shown by Matousek et al. in 1999 [51]. The general setup is shown in figure 3.1. The UVR scattering from the sample is polarized by the polarizer P and collimated by L₁. Then it is focused in the Kerr medium by L₂ where it is overlapped with the gate pulse. After the Kerr medium the light is recollimated by lens L₃ and focused into the spectrometer by L₄. Before the light reaches the spectrometer the gate pulse is blocked by a shortpass filter F₁, a cross-polarizer rejects the light for which the polarization was not rotated and finally the longpass filter F₂ rejects the Rayleigh scattered light. This describes the general setup of a Kerr gate. If no Kerr pulse is present the entire signal is rejected by the cross-polarizer and if a Kerr pulse is present, only light which is temporally overlapped with the Kerr pulse is transmitted.

The Kerr gate in reference [51] was used to reject the strong fluorescence of the laser dye 4-dicyanomethylene-2-methyl-6-p-dimethylaminostyryl-4-H-pyran from the spectra of S₁ p-quarterphenyl in dioxane. With the two polarizers in parallel position only a fluorescence signal with ca. 200 000 counts can be observed, while with the polarizers crossed and the gate pulse present, discrete Raman bands with a maximum of ca. 200 counts were measured.

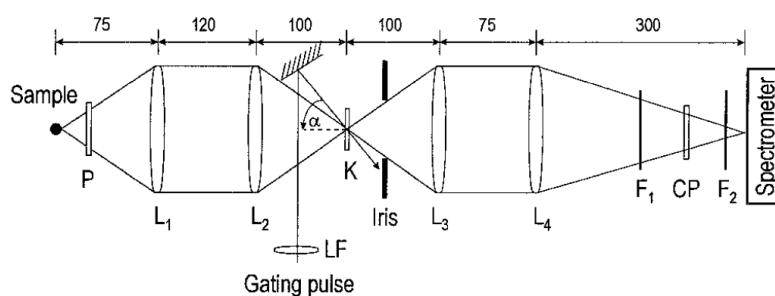


Figure 3.1: Schematic setup of a ps-Kerr gate; P, polarizer; L, lenses; K, Kerr medium; F_1 , shortpass filter blocking gate pulse; CP, cross-polarizer; F_2 , longpass filter blocking Rayleigh scattering; LF, focusing lens for the gate pulse. Reproduced from [51].

The performance of the Kerr gate is mainly limited by the polarizers and the Kerr medium. Firstly, both polarizers and Kerr medium need to be transparent for the required spectral region, which is mostly not a problem in the visible region, but can be demanding in the UV region. For the polarizers the extinction ratio is the most important parameter since it yields the maximum fluorescence suppression of the Kerr gate. Another important aspect is the thickness of the polarizer as it introduces group velocity dispersion which might exceed the response time of the gate over the desired spectral range of interest, especially for shorter wavelengths. This forces the use of thin polarizers such as nanoparticle or wire-grid polarizers [51–53] at the cost of either a limited usable spectral region or a smaller extinction ratio as compared to crystal polarizers, such as calcite Glan-Taylor polarizers. One way to realize a thinner broadband polarizer with high extinction ratio has been shown in [54] where a segmented Glan-Taylor polarizer was used. By stacking two Glan-Taylor polarizers on top of each other, the thickness could be halved from 41 mm to 20 mm while keeping the same aperture of 41x41 mm. However, the transmission of the combined polarizer was 14 % lower compared to a single larger polarizer, as there were losses on the contact plain of the two polarizers. Therefore, this concept does not seem scalable for even thinner polarizers.

The other performance-determining component is the Kerr medium. Depending on the nonlinear refractive index the rotation of the UVRR signal that can be achieved for a given power of the Kerr pulse and length of the Kerr medium changes. If the achieved rotation is not 90° , part of the UVRR signal is blocked by the cross-polarizers.

A commonly used Kerr medium is the liquid carbon disulfide (CS_2) [51, 55] since it is transparent in the visible spectral range and exhibits a high nonlinear refractive index of ca. $310 \times 10^{-16} \frac{cm^2}{W}$. However, an absorption band at $\lambda_{max} = 320 \text{ nm}$ [56] makes CS_2 an unsuitable Kerr medium for applications in the UV. Benzene can be used as a Kerr medium to extend the usable spectral range further into the UV [52]. However, the nonlinear refractive index of benzene is with ca. $160 \times 10^{-16} \frac{cm^2}{W}$ only about of half that of CS_2 .

To simplify the design and extend the Kerr gate to the entire non-vacuum UV region down to ca. 200 nm solid state Kerr media are needed. Several glasses and crystals have well documented nonlinear refractive indices [57, 58] and some have been tested specifically with regards to application as a Kerr medium [53, 59]. The nonlinear refractive indices of solids are significantly lower than for the two liquids discussed before, since for solid state media the nuclear

contribution to the nonlinear refractive index (cf. 2.3) is little to none. With regards to UV application especially fused silica (FS) and yttrium aluminum garnet (YAG) are of interest and were tested [53]. Both show transparency down to 200 nm, but for YAG the transmission starts decreasing around 300 nm, whereas the transmission of FS remains high. The nonlinear refractive index of YAG (ca. $6 \times 10^{-16} \frac{\text{cm}^2}{\text{W}}$) is higher than for FS (ca. $2 \times 10^{-16} \frac{\text{cm}^2}{\text{W}}$). However, due to a higher white light threshold in FS compared to YAG, i. e. in FS the intensity to generate white light is higher, the difference in nonlinear refractive index can be compensated by using a higher intensity gating pulse for FS. Another option for a Kerr medium with high transparency down to vacuum UV is calcium fluoride (CaF_2), although the nonlinear refractive index is a bit smaller than for FS with a value of ca. $1.7 \times 10^{-16} \frac{\text{cm}^2}{\text{W}}$.

3.3 DFT calculations of resonance Raman scattering

The assignment of peaks in vibrational Raman spectra is generally assisted by the calculations of the normal modes by means of density functional theory (DFT) [60]. For normal vibrational resonance Raman (RR) scattering, i. e. both initial and final state are in the electronic ground state (cf. 2.2), the wavenumber values are the same as in normal Raman scattering. However, the intensities of the individual modes can differ significantly. Hence, the calculation of the actual RR spectra can be needed for an unambiguous vibrational mode assignment.

To calculate the RR spectra the implementation in Gaussian 16 [61] can be used, which calculates the spectrum by means of DFT and its time-dependent extension (TD-DFT) [62] as it needs to calculate the excited electronic state of the resonance. The implemented method includes full treatment of Herzberg-Teller vibronic coupling and subsets thereof. You are able to choose to only consider the Franck-Condon (FC) terms, corresponding to the direct transition integrals (Albrecht A-term, cf. 2.2), or the Herzberg-Teller (HT) terms, corresponding to only vibronically coupled transitions (Albrecht B-, C-, and D-term) Alternatively, full treatment is possible as well considering both FC and HT terms (FCHT) [63–67]. Changes in the different basis sets of the ground and excited state are considered by a Duschinsky transformation [68], which is a linear transformation between the basis sets of the initial (\mathbf{Q}_I) and final state (\mathbf{Q}_F) by a Duschinsky matrix (\mathbf{J}) and a shift vector (\mathbf{K}):

$$\mathbf{Q}_I = \mathbf{J}\mathbf{Q}_F + \mathbf{K}. \quad (3.1)$$

For the actual calculation of the transition integrals there are two general modes implemented, a time-independent (TI) [65] and a time-dependent (TD) [66] one.

The TI method is based on a sum over states formalism. Looking at the expression for the components of transition polarizability $\alpha_{\rho\sigma}$ close to resonance (cf. chapter 2.2):

$$\alpha_{\rho\sigma} = \frac{1}{\hbar} \sum_{r \neq i, f} \frac{\langle f | \hat{p}_\rho | r \rangle \langle r | \hat{p}_\sigma | i \rangle}{\omega_{ri} - \omega_0 - i\Gamma_r} \quad (3.2)$$

where $\langle f |$ and $| i \rangle$ are the final and initial vibrational states, $| r \rangle$ and $\langle r |$ are the vibrational states in the electronically excited state, \hat{p}_ρ and \hat{p}_σ are the components of the transition dipole moment

between the ground and excited electronic states, ω_{ri} is the eigenfrequency difference between the electronically excited vibrational states and the initial state ($\omega_{ri} = \omega_r - \omega_i$; resonance frequency), ω_0 is the incident/excitation frequency and Γ_r is the phenomenological dampening constant. With the TI method this expression needs to be calculated for all, possibly infinite, states r . This requires a prescreening of the transitions, to evaluate which transitions actually contribute a significant amount to the Raman intensity. The prescreening method [63,69,70] used in Gaussian 16 is based on an initial ordering of the transitions in so-called classes, which depend on the number of simultaneously excited modes in the final state. The first class (C_1) corresponds to fundamentals and overtones, the second class (C_2) on 2-modes combinations, the third class (C_3) on 3-modes combinations and so on. Only for the first two classes actual calculations are carried out, where every transition of these classes to states with a lower or equal number of quanta up to maximum C_1^{max} for C_1 and C_2^{max} for C_2 is calculated. From these calculated transitions, the transition probability and intensity is saved and used to estimate the probability and intensity for transitions to higher classes as C_3 and above. As a result, a vector is generated, which specifies the maximum number of quanta, that can be reached for each eigenmode. Additionally, the calculated intensities of the transitions can be compared to the total intensity, which can be calculated from equation 3.2 analytically by use of the closure relation, to test the quality of the prescreening. This prescreening method has proven effective for medium to large size molecules [63,69], however for higher temperatures, when the multiple initial states have to be considered, the computational cost for a sum-over-states methods increases sharply.

This temperature problem does not apply to the TD method [66,67]. The idea for this method is to turn the summation in equation 3.2 into a time-dependent integral by a Fourier transform:

$$\alpha_{\rho\sigma} = \frac{i}{\hbar^2} \int_0^\infty \langle f | \hat{p}_\rho e^{-i\hat{H}'t/\hbar} \hat{p}_\sigma | i \rangle e^{i(\omega_i + \omega_0)t - \Gamma t} dt \quad (3.3)$$

where the parameters are the same as above plus the time evolution operator $e^{-i\hat{H}'t/\hbar}$ and the simulation time t . With this formalism, all initial and final states are implicitly included in the calculation. This makes a prescreening unnecessary and it is independent of temperature effects, since all modes are always considered, as compared to the TI method. However, the implicit nature of the inclusion makes it impossible to assign the contribution of a transition to overall band-shape of the calculated Raman spectrum.

The implemented methods have been tested mainly against simple aromatic radicals, as the benzyl, phenyl, and phenoxy radicals [64,66], for fundamental transitions up to D_3 which implies excitation wavelengths above 300 nm. For shorter wavelengths, which are utilized for studying supramolecular ligands with UVRR (cf. chapter 3.1), only a single UVRR spectrum of anthracene was examined [66]. Therefore, further comparative studies of calculated and experimental UVRR spectra are necessary in order to gauge the general applicability of calculated UVRR spectra to our studies.

4 Materials and Methods

4.1 Experimental UVRR setup

For all UVRR measurements a home-built setup was utilized. The laser system is based on an amplified Yb:KGW laser (Pharos PH1, Light Conversion) which provides two outputs with a wavelength of 1030 nm, a pulse energy of 300 μJ , and a repetition rate of 10 kHz. One output is compressed to ca. 180 fs, the other output is uncompressed with ca. 150 ps and 111 cm^{-1} bandwidth. The compressed output can be utilized as the gating pulse for a Kerr gate (cf. 5.5), whereas the uncompressed output is used to generate the UV excitation pulses. The uncompressed output is fed to a second harmonic bandwidth compressor (SHBC, Light conversion), in which the pulses are split in two beams which are then inversely chirped and overlapped in a BBO crystal to generate sum-frequency. This yields narrow bandwidth (ca. 8 cm^{-1} and 3 ps) second-harmonic pulses with a wavelength of 515 nm. The second-harmonic beam is then used to pump a three-stage optical parametric amplifier (OPA) (Orpheus PS, Light Conversion). For this purpose the beam is split in three parts by two beam-splitters. Additionally, the positively chirped residual pulses from the SHBC are recompressed inside of the OPA and focused into a sapphire crystal to generate white-light in the range from 450 nm to 1200 nm.

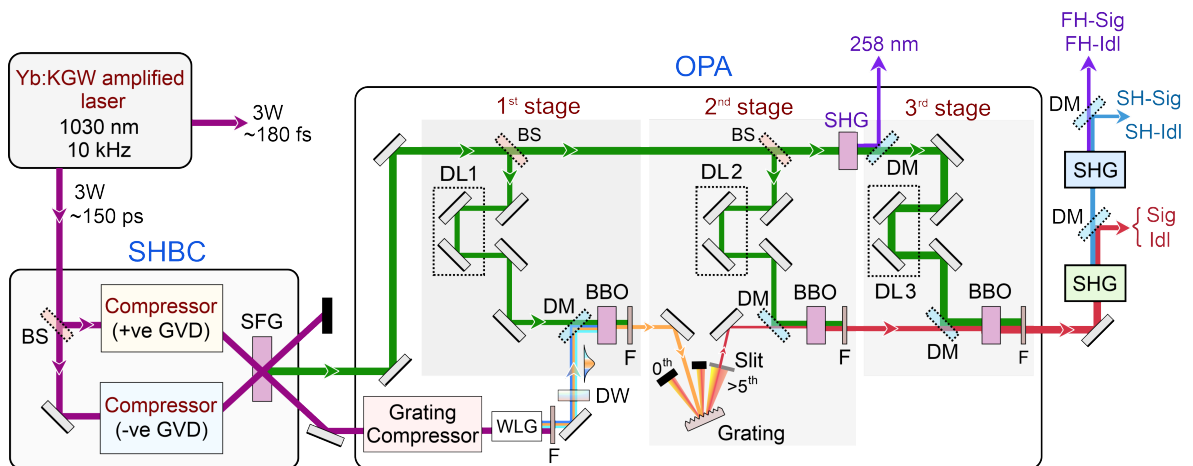


Figure 4.1: Schematic depiction of the tunable UV laser light source. From the base laser system (Pharos PH1) a narrow bandwidth second harmonic beam is generated in the SHBC, which is then used to pump the OPA (Orpheus PS) to generate tunable narrow bandwidth laser pulses in the range from 630-2600 nm. Two sequential second harmonic generation stages afterwards extend the tuning range down to 210 nm. SHBC, second harmonic bandwidth compressor; BS, beam-splitter; GVD, group velocity dispersion; SFG, sum-frequency generation; OPA, optical parametric amplifier; DW, dispersion window; F, filter; DM, dichroic mirror; DL, delay line; SHG, second-harmonic generation; Sig, signal; Idl, idler. Taken from reference [71].

The OPA can be separated in three individual stages in which the first two stages serve to select

the wavelength and create a narrow-bandwidth pulse, and the third stage is a pure amplification stage. Before the first stage, the white-light is dispersed by a dispersion window to separate the wavelengths within the white-light pulse. Then the white-light and the pump beam are collinearly overlapped in a BBO crystal. By adjusting the delay between white-light and pump pulse and the phase-matching angle of the crystal, the wavelength which is amplified can be selected. In the second stage, a grating is used to create a narrow-bandwidth pulse. The beam from the first stage is sent to the grating and the dispersed light is then selected by a slit in a high diffraction order ($> 5^{th}$ order, depending on the wavelength) and again overlapped in a BBO crystal with the pump beam. In the third stage the beam is then again overlapped in a BBO crystal to amplify the narrow-bandwidth pulses. As a result, the OPA provides narrow-bandwidth pulses ($< 15 \text{ cm}^{-1}$) tunable in the range from 630-1020 nm (signal) and 1040-2600 nm (idler). After the OPA, two second-harmonic generation crystals (Lyra, Light Conversion) are used to consecutively produce the second- and fourth-harmonic of the OPA output. These two Lyra units extend the tunability of the laser system down to 210 nm with an average power of $> 10 \text{ mW}$. Additionally, the OPA generates an output with 258 nm and an average power of ca. 50 mW by direct second-harmonic generation of the pump beam before the third stage.

The UV light is then focused on the sample. Here two illumination schemes were utilized. For the measurements with anthracene, the laser light was loosely focused with a plan-convex fused silica lens ($f=200 \text{ mm}$) into a quartz cuvette ($2 \times 10 \text{ mm}$, Hellma).

For the measurements with the supramolecular ligands in aqueous solution, a home-built free-flow system was used to minimize possible photo bleaching. For a schematic depiction see figure 4.2. The free-flow system is a closed-loop system driven by a peristaltic pump. The upper reservoir consist of an air filled one-way syringe. The air in the syringe serves to flatten the pressure oscillation from the peristaltic pump. A cut injection needle with an outer diameter of 0.8 mm attached to the syringe serves as the output nozzle. In this fashion, a laminar flow column of ca. 10 mm is formed in the focal plane of the laser light. The laser light was focused by two cylindrical lenses ($f=200 \text{ mm}$ and $f=100 \text{ mm}$) to create a line focus that matches the laminar flow column. The line focus reduced the incident intensity on the sample to further reduce photo bleaching.

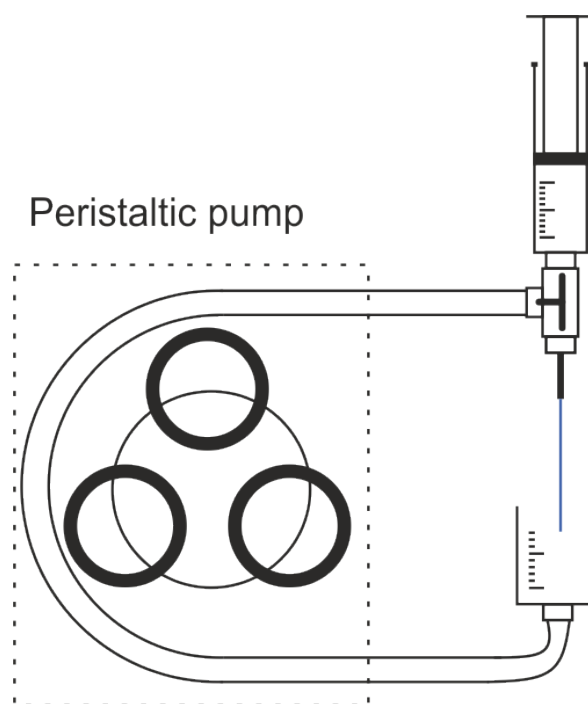


Figure 4.2: Schematic depiction of the home-built free-flow system. The closed-loop system is driven by a peristaltic pump. The syringe on the top acts as a closed air reservoir to flatten the pressure oscillation of the pump. The liquid is driven through a cut injection needle creating a liquid column in the air, which is collected by a cut-off syringe.

For both illumination schemes, the cuvette and the free-flow, the scattered light was collected in 90° geometry by a two inch fused silica lens with a focal length of 100 mm and subsequently focused into the UV-optimized spectrometer (SpectraPro.500i, Acton Research Corp.) by a two inch lens with a focal length of 200 mm. The spectrometer was equipped with a grating with 2400 grooves/mm blazed at 240 nm and a cryogenically-cooled and UV-optimized CCD sensor (PyLoN:2KBUV, Princeton Instruments).

The collection setup used for the Kerr gate setup is shown and described in chapter 5.5.

4.2 UV-Vis absorption spectroscopy

All UV-Vis absorption measurements were measured with a Perkin-Elmer Lambda 650 spectrophotometer. The spectrophotometer has two lamps, one deuterium lamp for the UV and a tungsten halogen lamp for the Vis region. The lamps are swapped at a wavelength of 319.2 nm. The spectra were acquired in 0.5 nm steps with an integration time of 0.2 s of the photomultiplier tube. Before each acquisition a baseline spectrum was recorded and subtracted. The samples were in a quartz cuvette with 2 mm optical path length and inserted into the front holder of the UV-Vis spectrophotometer for measurements.

4.3 Sample preparation

All supramolecular ligands were synthesized by collaboration partners from organic chemistry in the chemistry department of our university. Daniel Sebena (former Schmuck group, then

Voskuhl group) synthesized both the guanidiniocarbonyl pyrrole and -indole ethyl amide and Philipp Rebmann (Schrader Group) synthesized the molecular tweezers CLR01. The ligands were cleaned by preparative HPLC and lyophilized afterwards. For the UVRR measurements the ligands were solvated in appropriate buffer solution. For GCP and GCI a 6 mM BisTris (**Bis**(2-hydroxyethyl)amino-**tris**(hydroxymethyl)-methane) at pH 6 was used and for the molecular tweezers CLR01 pure water was used.

Bovine serum albumin (BSA) was obtained from Sigma Aldrich in lyophilized form (purity > 98%). The Survivin protein was prepared by Annika Meiners (Knauer Group). Both proteins and the mixtures with GCI were solvated in a low salt HEPES (4-(2-hydroxyethyl)-1-piperazineethanesulfonic acid) with 2.5 mM HEPES, 10 mM NaCl, 1 mM MgCl₂, and 50 μM TCEP (**tris**(2-carboxyethyl)**phosphine**) at pH 6.5 in order to ensure the stability of Survivin.

All ligands and the Survivin protein were provided as part of cooperations within the CRC 1093 with the projects A1/A10 (GCP and GCI; Daniel Sebens), A3 (molecular tweezers; Philipp Rebmann) and B5 (Survivin; Annika Meiners).

Anthracene was obtained from Sigma Aldrich in analytical standard quality.

4.4 DFT parameters

All DFT and TD-DFT calculations were performed with the Gaussian 16 [61] program suite. For the different molecules, different functionals, basis-sets and correction methods were used.

The most intensive calculations were done for anthracene. Here, all calculations were done with the SNSD [72] basis set, a double- ζ basis set built upon the G-31G(d,p) Pople basis set, and the B3LYP functional. Solvent effects were considered with the integral equation formalism polarizable continuum model (IEF-PCM) with the standard values available within Gaussian 16. For the TD-DFT calculations, the first 20 excited electronic states were considered. All vibronic calculations (one-photon absorption and RR spectra) were done with the time-independent formalism (meaning a sum-over-states approach) and the adiabatic Hessian method (both ground and excited state at their respective minimum within the harmonic level). For the anharmonic corrections, two different formalisms of second-order vibrational perturbation theory were utilized. For the ground state, meaning the normal Raman spectrum, the generalized second-order vibrational perturbation theory (GVPT2) was used. Corrections to the UVRR spectrum were considered by hybrid degeneracy-corrected second order vibrational perturbation theory (HDCPT2). Example files for the calculations of the resonance Raman spectra are given in appendix A.

Calculations of the molecular tweezers CLR01 were done with the B3LYP functional, the 6-31G(d,p) basis set, and the conductor-like polarizable continuum model (C-PCM) for water.

For the calculation of the Raman spectrum and normal modes of guanidiniocarbonyl indole (GCI) the B3LYP functional with inclusion of the D3 version of Grimme's dispersion was used together with the triple- ζ 6-311++G(d,p) Pople basis set. Additionally, the calculations were checked with the double hybrid B2PLYP functional.

5 Results and Discussion

5.1 UVRR excitation study of anthracene

In this chapter a comparative study between DFT calculated and measured UVRR spectra is shown. DFT calculations of normal Raman spectra are routinely used to augment and explain the experimentally observed Raman spectra. However, in case of resonance Raman scattering, additional effects become relevant because of the involvement of the excited state, which is not considered in the calculation of normal Raman spectra. The calculation of the resonance Raman spectra, although available in the current version of Gaussian, is not commonly as it entails much more complex calculations. Here the implementation for the DFT calculation of resonance Raman spectra is tested against experimental UVRR spectra of a test molecule in order to gauge the applicability of DFT calculated UVRR spectra for future UVRR measurements. As a test molecule anthracene was chosen, as it is a small and rigid molecule with a high symmetry (D_{2h}) and a delocalized π -system. The size and rigidity keep the computational cost low since a smaller number of atoms means less basis functions and the rigidity leads to a low number of transitions which significantly contribute to the spectrum; this simplifies the calculations in a sum-over-states formulation the calculation is based on. The symmetry leads to a higher number of overtone and combination modes in the vibrational spectrum, which in turn leads to more bands that can be analyzed. Finally, the delocalized π -system makes anthracene highly Raman-active, which makes the acquisition of the UVRR spectra easier.

The first step for the comparison study between experimental and DFT computed UVRR spectra of anthracene is to find a suitable solvent. First, the solvent has to be transparent in the spectral region of interest, meaning close to the resonance. Second, the solvent should exhibit negligible interaction with the analyte. This will simplify the DFT calculation, as it allows to account for the solvent by means of a simple PCM as compared to an explicit solvent model. Third, the overlap of bands from Raman spectra of the solvent and the UVRR spectrum of anthracene should be minimal. To satisfy the first point, three UV-transparent solvents, acetonitrile, dichloromethane and cyclohexane, were chosen to test for the second and third point. The second point can be analyzed by the UV-absorption spectrum.

Figure 5.1 shows the UV absorption spectra of a 100 μ M anthracene solution in acetonitrile (black), dichloromethane (red), and cyclohexane (blue). The spectra are similar for all solvents with a distinctive maximum corresponding to the electronic $S_0 \rightarrow S_9$ transition and a shoulder at lower wavelengths. The maximum absorption is at circa 251 nm for acetonitrile, 253 nm for cyclohexane, and 255 nm for dichloromethane. Since the spectra are similar for all three solvents we can expect the interaction of solvent and analyte to be negligible and therefore the use of a PCM for the DFT calculations is justified.

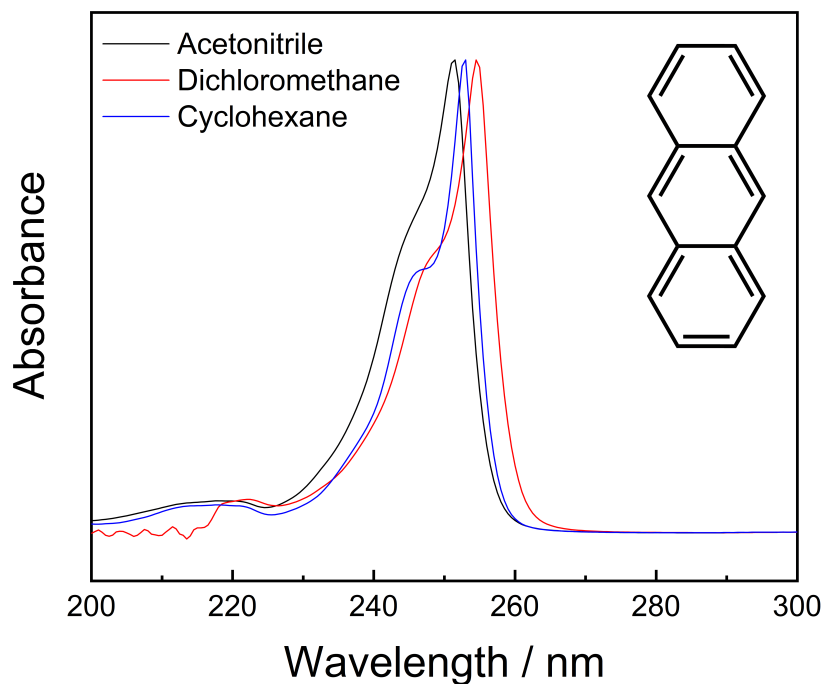


Figure 5.1: UV absorption spectra of 100 μM solutions of anthracene in acetonitrile (black), dichloromethane (red), and cyclohexane (blue) together with the molecular structure of anthracene.

To test for overlap of the Raman bands of the solvent and the analyte (third requirement), the actual UVRR spectra in the respective solvents have to be considered. In figure 5.2 the UVRR spectra of the 100 μM anthracene solutions in acetonitrile (top), dichloromethane (middle), and cyclohexane (bottom) excited at their respective resonance wavelengths are displayed in the region from 300 cm^{-1} to 3200 cm^{-1} together with the Raman spectra of the neat solvents. For the solution in acetonitrile there are several Raman peaks in the fingerprint region from 500 cm^{-1} to 1800 cm^{-1} with the most prominent peaks around 750 cm^{-1} and 1400 cm^{-1} . Other strong peaks can be observed around 389 cm^{-1} , 2250 cm^{-1} , 2938 cm^{-1} , and 2999 cm^{-1} . Contributions from the solvent in the fingerprint region are mainly the peaks around 1374 cm^{-1} and 1441 cm^{-1} , attributed to the CH_3 s- and d-deformation mode, respectively [73]. These two modes partially overlap with the 1400 cm^{-1} peak of anthracene, but do not obscure it. The solvent exhibits a peak around 378 cm^{-1} , attributed to the CCN bend, which is shifted by 12 cm^{-1} from the band observed in the solution. This shift is most likely due to an overlap of the solvent band with a peak from anthracene, which is expected around 390 cm^{-1} . The peaks observed in the high-wavenumber region are pure solvent peaks attributed to the CN stretch at 2250 cm^{-1} and the CH_3 s- and d-stretch at 2938 cm^{-1} and 2999 cm^{-1} , respectively. For dichloromethane as the solvent, a strong overlap of the solvent bands with the bands of the anthracene solution is apparent. The anthracene peak expected around 750 cm^{-1} is completely obscured by two DCM peaks around 705 cm^{-1} and 741 cm^{-1} , attributed to CCl_2 stretching. The other strong anthracene peak around 1400 cm^{-1} is only visible as a shoulder to the 1424 cm^{-1} DCM peak of the CH_2 scissor vibration. For the solution in cyclohexane the main peaks are observed around 390 cm^{-1} , 755 cm^{-1} , and 1404 cm^{-1} .

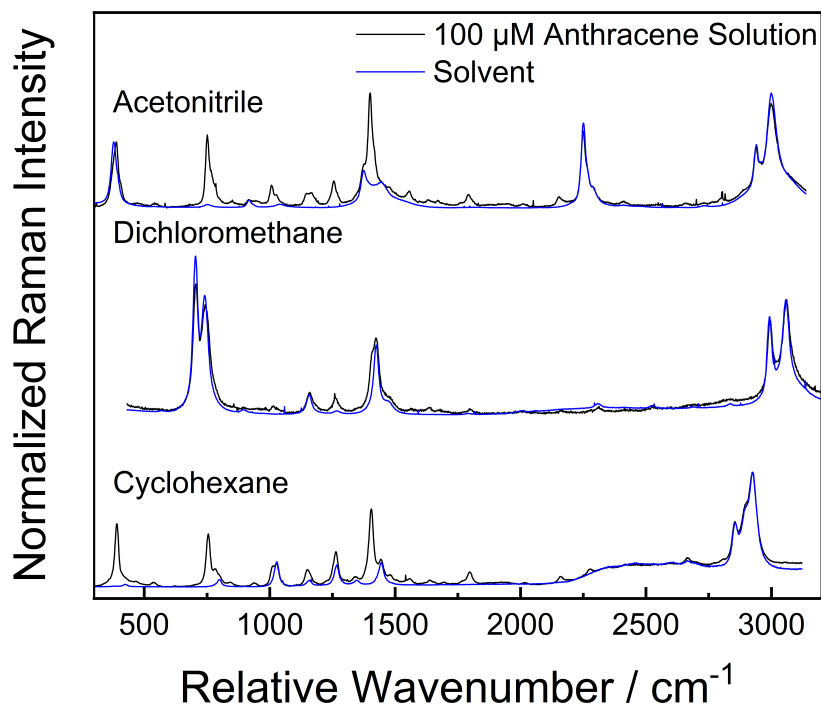


Figure 5.2: UVRR spectra of 100 μM anthracene solution (black) in acetonitrile (top), dichloromethane (middle) and cyclohexane (bottom) excited at their respective electronic resonance together with the normal Raman spectra of the neat solvents (blue).

In the fingerprint region the influence of solvent is lowest for acetonitrile. Thus acetonitrile was used for the following experiments.

The results of DFT calculations displayed in this chapter were obtained in a cooperation with Julien Bloino and Vincenzo Barone from the SMART lab at the Scuola Normale Superiore (SNS) in Pisa. The methods used are described in chapter 4.4 and the results were published together with the experimental results in reference [74].

In order to calculate the UVRR spectrum of anthracene, first the normal Raman spectrum has to be calculated. Figure 5.3 shows DFT calculated and experimental Raman spectra of anthracene in the spectral region of 500 cm^{-1} to 2000 cm^{-1} . The DFT calculated Raman spectrum is shown, once in the harmonic approximation (blue) and once with anharmonic corrections (red). Since anthracene has D_{2h} symmetry the modes can easily assigned to one of the four irreducible representations of the point group. Additionally, the mutual exclusion principle is applicable and only the modes which are symmetric with regard to the center of inversion (*i*) (so called *g*-modes; $i=+1$ in the character table) are Raman-active. In the harmonic approximation one dominant peak at 1431 cm^{-1} can be observed, which corresponds to a totally symmetric (a_g) in-plane mode. Other peaks at 760 cm^{-1} , 1289 cm^{-1} , and 1591 cm^{-1} can also be classified as a_g modes. The 760 cm^{-1} peak arises from a ring-breathing mode involving the entire three-ring-system, whereas the peak at 1289 cm^{-1} is associated with a ring-breathing mode mainly involving the central phenyl ring. The peak at 1594 cm^{-1} again involves CC stretching delocalized over all three phenyl rings. The eigenvectors of the four modes described here are also displayed in figure 5.4.

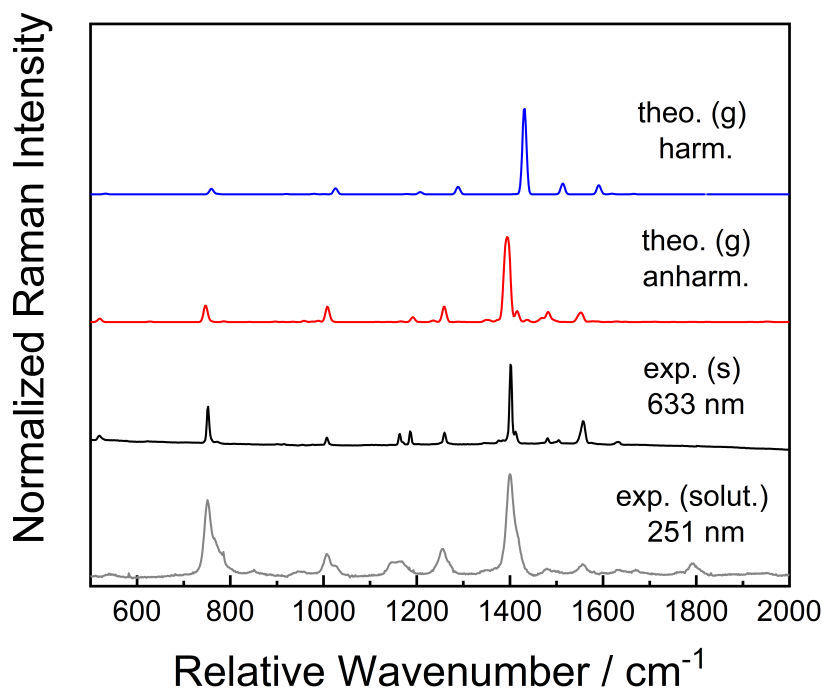


Figure 5.3: DFT calculated normal Raman spectra without (blue) and with (red) anharmonic corrections together with the experimental normal Raman spectrum excited at 633 nm and the UVRR spectrum excited at 251 nm. Taken from reference [74].

The only observable peak that is not due to an a_g mode is the peak at 1208 cm^{-1} , which corresponds to a b_{3g} mode. When applying anharmonic corrections to the calculated spectrum (figure 5.3, red curve), all dominant peaks discussed above are shifted to smaller wavenumbers: $760 \rightarrow 747\text{ cm}^{-1}$, $1208 \rightarrow 1192\text{ cm}^{-1}$, $1289 \rightarrow 1258\text{ cm}^{-1}$, $1431 \rightarrow 1394\text{ cm}^{-1}$, and $1594 \rightarrow 1552\text{ cm}^{-1}$. Apart from the wavenumber shift, additional bands can be observed, such as the peak at 1415 cm^{-1} next to the dominant peak at 1394 cm^{-1} . Comparing this with the experimental Raman spectrum of anthracene in the solid state (black curve), this shoulder is also observed at 1412 cm^{-1} next to the main peak at 1402 cm^{-1} . In general the mean error between the experimental and calculated Raman spectrum is below 5 cm^{-1} . Lastly, the UVRR spectrum of a $100\text{ }\mu\text{M}$ solution of anthracene in acetonitrile is shown in gray with the solvent peaks subtracted. Compared to the normal Raman spectrum, the wavenumber positions of the peaks in the UVRR spectrum are similar, with peaks at 751 cm^{-1} , 1255 cm^{-1} , 1401 cm^{-1} , and 1556 cm^{-1} . The relative intensities however change, with a stronger signal for the peak at 751 cm^{-1} and a lower signal for the peak at 1556 cm^{-1} , compared to the main peak at 1401 cm^{-1} . Additionally, in the UVRR spectrum a peak at 1791 cm^{-1} can be observed which is present in neither the calculated nor the experimental normal Raman spectra. This peak is most likely due to an overtone/combination mode. Only due to the vibronic coupling of the two modes it becomes intense enough to be visible in the UVRR spectrum (see D -term in chapter 2.2).

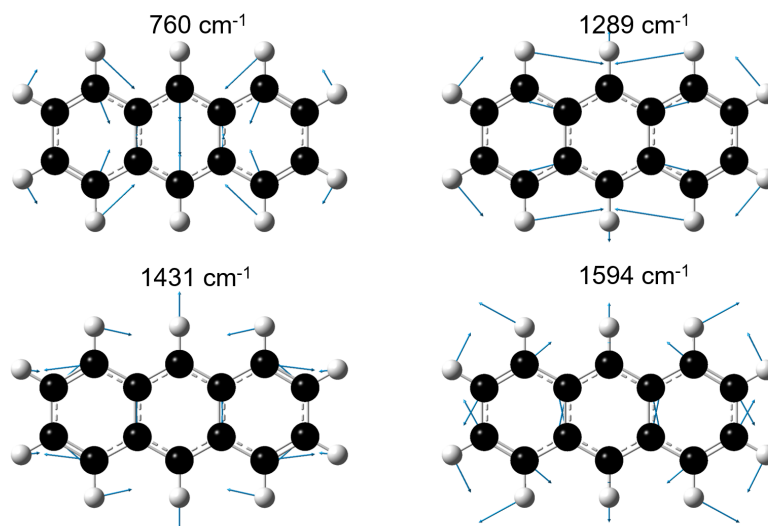


Figure 5.4: DFT calculated eigenvectors of selected normal modes at 760 cm^{-1} , 1289 cm^{-1} , 1431 cm^{-1} and 1594 cm^{-1} . Taken from reference [74].

The next step for the calculation of UVRR spectra is to calculate the excited state with TD-DFT methods. A first step to test the TD-DFT calculation can be done by examining the one-photon absorption spectrum. Figure 5.5 shows the normalized experimental and TD-DFT calculated absorption spectra of anthracene in acetonitrile in the spectral range of $37000 - 47000\text{ cm}^{-1}$ ($\approx 270 - 213\text{ nm}$). The experimental spectrum, as described above, exhibits a maximum at 39800 cm^{-1} (251 nm) with a shoulder on the higher-wavenumber (lower wavelength) side. The DFT calculated vibronic spectra at both, the Franck-Condon (FC) (orange) and the Franck-Condon Herzberg-Teller (FCHT) (blue) level of theory (cf. chapter 3.3), exhibit similar characteristics, albeit with an overall wavenumber shift of approximately 1400 cm^{-1} (10 nm) with an absorption maximum around 41150 cm^{-1} . This difference between the experimental and TD-DFT calculated absorption spectrum can be considered relatively small for this kind of TD-DFT calculations, especially taking into account that the examined transition is to a higher excited state, i.e. from S_0 to S_9 . Comparing the calculated spectra at the FC and FCHT level of theory, the FC spectrum exhibits a pronounced peak on the higher wavenumber side, whereas the FCHT spectrum reproduces the higher wavenumber shoulder of the experimental spectrum more closely. This suggests that the Herzberg-Teller contributions are required for an accurate description of vibronic effects, which is to be expected, as the oscillator strength of the electronic transition is low with $f = 0.031$, meaning the electronic transition dipole moment is of the same order of magnitude as its derivatives. The observed shoulder is associated with several vibrational transitions, but the main contribution is from the $|0\rangle \rightarrow |1_{41}\rangle$, $|0\rangle \rightarrow |1_{46}\rangle$, and $|0\rangle \rightarrow |1_{55}\rangle$ transitions, which correspond to the previously discussed 760 cm^{-1} , 1431 cm^{-1} and 1594 cm^{-1} normal modes, respectively (cf. figure 5.4).

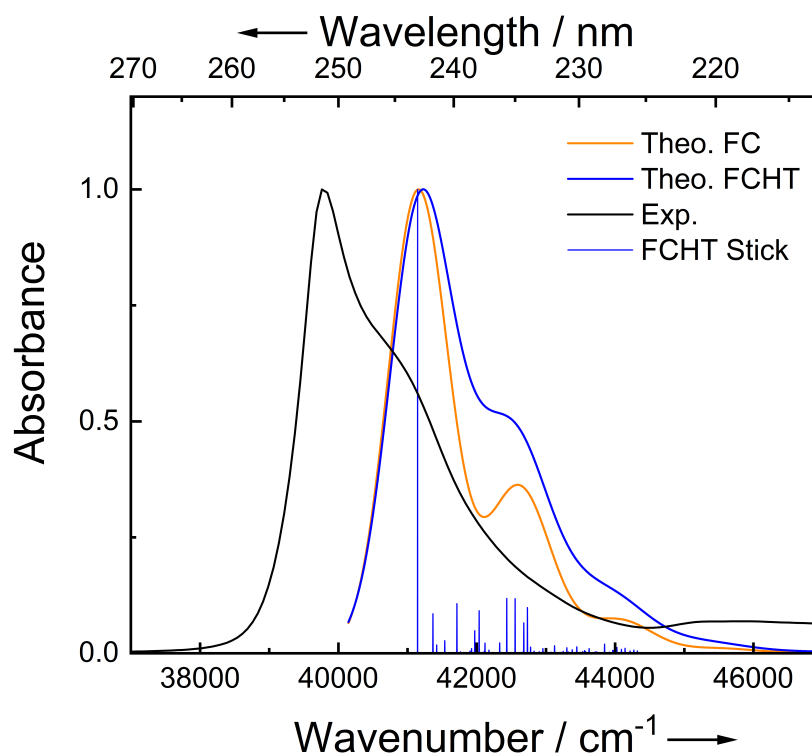


Figure 5.5: Experimental UV absorption spectrum of anthracene in acetonitrile (black) together with the calculated one-photon absorption spectra at the Franck-Condon (FC)(orange) and the FC Herzberg-Teller (FCHT)(blue) method in the range from 37000-47000 cm^{-1} . Taken from reference [74].

Figure 5.6 compares the vibronic UVRR spectrum calculated at different levels of theory with the experimental UVRR spectrum. At first only the direct dipole transitions are considered with the FC method (orange). In this case only peaks corresponding to totally symmetric a_g modes are enhanced and observable in the UVRR spectrum. The most intense peak is around 1590 cm^{-1} which stands in contrast to the experimental spectrum (black) for which the most intense peak is around 1400 cm^{-1} . With the FCHT method the coupling between the electronic and nuclear motion is considered as well (blue curve). By the inclusion of this vibronic coupling also non-totally symmetric modes (mostly b_{2g}) with similar intensities as the a_g modes can be observed in the calculated spectrum. The necessity for the inclusion of HT effects was already expected from the analysis of the one-photon absorption spectra. Additionally, the relative intensities of the a_g modes change as well and the most intense peak is now around 1432 cm^{-1} . By considering a second vibrational quantum to be present in the calculation (FCHT 2^{nd} Q, red), overtone and combination bands can be observed as well. Most notably are the peaks at 1666 cm^{-1} and 1826 cm^{-1} , which arise from combinations of a_g and b_{1g} modes. The latter of the two combination peaks corresponds to the experimentally observed peak at 1794 cm^{-1} . In a final step, additional anharmonic corrections are applied to the calculated spectrum (FCHT 2^{nd} Q anharmon., violet). This results in an excellent agreement of the peak positions of the experimental and calculated UVRR spectrum. For example, for the prominent modes shown in figure 5.4 the deviation is below 4 cm^{-1} as compared to more than 30 cm^{-1} in the harmonic approximation. For the intensities, however, the difference between experimental and calculated values is much larger. While the dominant band in the experimental spectrum around 1401 cm^{-1} is well reflected

in the calculations, the band around 1556 cm^{-1} (exp.)/ 1552 cm^{-1} (FCHT 2^{nd} Q anharm) is strongly overestimated and comparable in intensity to the 1401 cm^{-1} band. Conversely, for the 754 cm^{-1} band the anharmonic corrections results to an intensity increase, but the intensity is strongly underestimated in the calculated spectrum. Additionally, some strong peaks in the calculated spectrum are not reflected in the experimental spectrum, such as the bands at 572 cm^{-1} and at 843 cm^{-1} . This mismatch between experimental and calculated spectrum can, at least in part, be attributed to general problems of TD-DFT with the description of higher excited states, such as S_9 in this case, which will translate into errors in the calculations of transition integrals necessary to describe the UVRR spectrum.

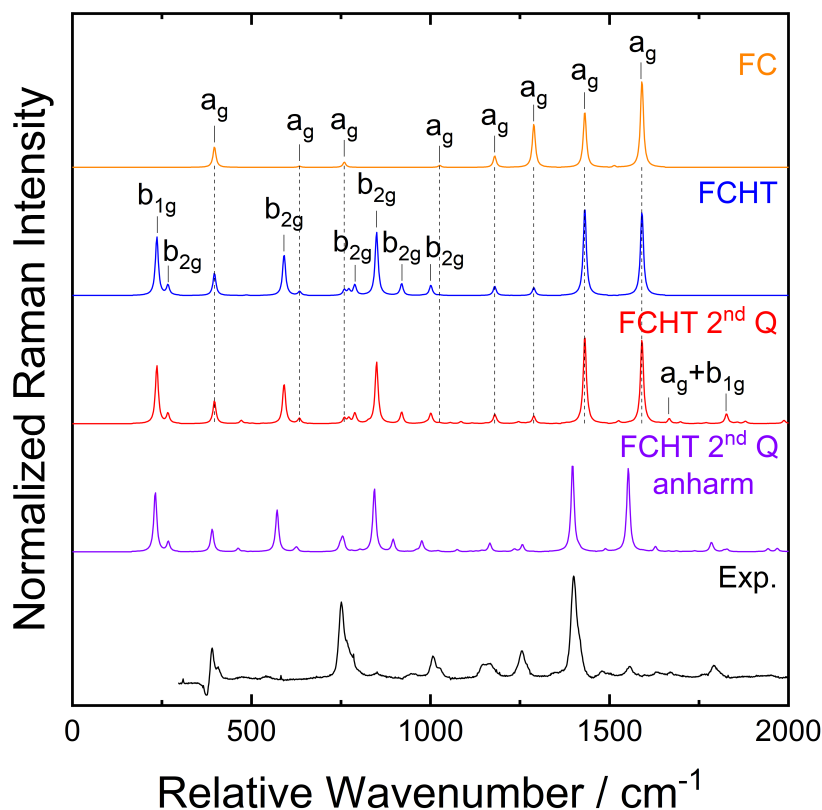


Figure 5.6: Calculated ultraviolet resonance Raman spectra calculated by different methods; Franck-Condon (FC)(orange), Franck-Condon Herzberg-Teller (FCHT)(blue), FCHT with inclusion of an additional vibrational quantum (FCHT 2^{nd} Q)(red), and FCHT 2^{nd} Q with anharmonic corrections (FCHT 2^{nd} Q anharm)(violet). The experimental UVRR spectrum excited at 251 nm and with solvent bands subtracted (black) is shown for comparison. Taken from reference [74].

In the last step, UVRR excitation spectroscopy in the range from 253 nm to 244 nm was performed. The spectral region was chosen as to scan across the resonance at 251 nm and still have enough resonance enhancement for reasonable signal quality. Closer to the resonance at 251 nm spectra were obtained in 1 nm steps of the excitation wavelength from 253 nm to 248 nm and from 248 nm to 244 nm in 2 nm steps. The eight obtained experimental UVRR spectra (black) are shown in the range from $500 - 2000\text{ cm}^{-1}$ in figure 5.7 together with the corresponding DFT calculated vibronic UVRR spectra (blue). For reference the Raman spectrum of the used solvent acetonitrile obtained with an excitation wavelength of 251 nm is displayed in red.

For an excitation wavelength of 253 nm, the features of the UVRR spectrum closely resemble

the ones observed for the resonance condition, i. e. the main peak around 1405 cm^{-1} and another strong peak around 755 cm^{-1} , but with lower intensities. Decreasing the laser excitation wavelength towards the resonance condition at 251 nm leads to an intensity increase for all observable bands. When moving to even lower wavelengths, changes in intensity differ depending on the peak position. The peak at 755 cm^{-1} exhibits a steady, but slow decrease in intensity for moving the excitation wavelength from 251 nm to 244 nm . For the peaks at 1259 cm^{-1} , 1405 cm^{-1} , and 1561 cm^{-1} the intensities decrease at first when moving the excitation wavelength from 251 nm to 249 nm , but then the intensities of the peaks increase again when moving from 249 nm to 246 nm . These peaks correspond to the transitions which were identified to carry a major contribution to the lower wavelength/higher wavenumber shoulder in the one-photon absorption spectrum (see fig. 5.5). When lowering the excitation wavelength even further to 244 nm the intensity of the peaks decreases again. For the calculated UVRR spectrum the increase and decrease of all Raman peaks around the resonance condition is similar when moving from 253 nm to 250 nm . For even lower wavelengths, the intensities of most peaks decreases, however single peaks show a great increase around certain wavelengths. In this fashion single peaks are strongly enhanced for a specific excitation wavelength: the peak at 572 cm^{-1} exhibits enhancement at 248 nm , the peak at 844 cm^{-1} at 246 nm , and the peak at 1256 cm^{-1} at 244 nm excitation wavelength. These increased intensities are expected to be due to vibronic coupling, as the wavenumber value of the peaks roughly matches the wavenumber shift from the resonance. For the peak at 1256 cm^{-1} the wavenumber shift from resonance is ca. 1143 cm^{-1} assuming the resonance to be at 251 nm .

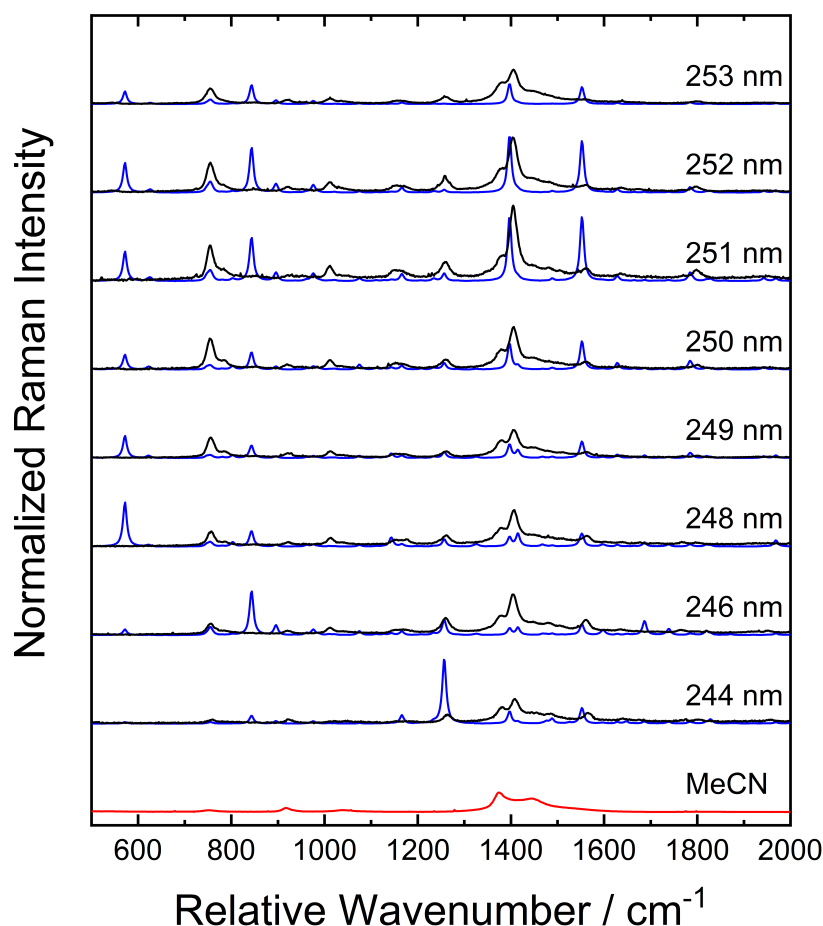


Figure 5.7: Experimental ultraviolet resonance Raman (UVR) spectra (black) at excitation wavelengths between 253 nm and 244 nm together with calculated UVR spectra (blue) with Franck-Condon and Herzberg-Teller (FCHT) with second vibrational quanta and anharmonic wavenumber correction. Raman spectrum of the solvent acetonitrile (red) on the bottom. Taken from reference [74].

To better elucidate and compare the observed changes, the experimental (black, exp.) and the calculated (red, theo.) Raman excitation profile (REP) of the peaks at 755 cm^{-1} , 1258 cm^{-1} , 1405 cm^{-1} , and 1561 cm^{-1} are displayed in figure 5.8. The decrease of intensity towards a minimum at 249 nm and a maximum around 246 nm for all peaks except the one at 755 cm^{-1} becomes obvious. Curiously, the calculated REP of the peak at 755 cm^{-1} matches more closely with the experimental REP of the peak at 1258 cm^{-1} . This mismatch can be due to small errors in the determination of the laser excitation wavelength of the experimental resonance condition, since the calculated values are scaled to match this condition and a variation of 0.5 nm results in a wavenumber shift of ca. 80 cm^{-1} .

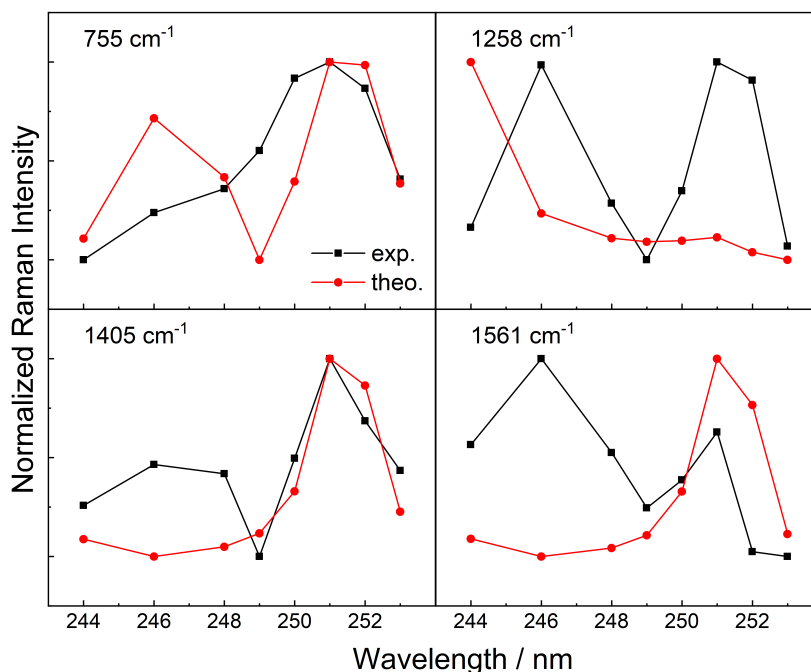


Figure 5.8: Experimental and calculated Raman excitation profile anthracene in acetonitrile for the peaks at 755 cm^{-1} , 1258 cm^{-1} , 1405 cm^{-1} , and 1561 cm^{-1} . Taken from reference [74].

In conclusion, the qualitative changes observed in the experimental UVRR spectra are replicated well by the calculated UVRR spectra when close to the resonance. This allows for better assignment of the individual peaks as compared to using just the calculated normal Raman spectrum. Additionally, peaks only present in the resonant case, such as the peak due to overtones around 1791 cm^{-1} , can only be assigned with the help of the FCHT 2^{nd} Q spectrum, which proves the necessity for vibronic calculations in this case. Also, when looking at the REP the calculated spectra show some similarities which help interpret the measured spectra. However, there are still significant discrepancies in the intensities of most modes apart from the main mode around 1400 cm^{-1} , which can at least in part be attributed to problems describing the highly excited state S_9 . Errors in the description of the excited state will then also translate into errors of the transition integrals required for calculation of the UVRR intensities. Therefore it seems better to study lower excited states in the future. However, considering the rather cheap methods used here (B3LYP functional and double- ζ basis set), the agreement between experimental and calculated spectra can still be seen as very satisfactory and all the calculations can be carried out in the base version of Gaussian.

5.2 UVRR of the molecular tweezers CLR01

The next chapters contain studies of supramolecular binding motifs prevalent in the work of the CRC 1093 “Supramolecular Chemistry on Protein”. The main goal of CRC 1093 is to achieve specific interaction with proteins by artificial ligands, for example, using a supramolecular ligand to block a specific protein domain to inhibit protein function. The main anchor point for these supramolecular ligands are the binding motifs, which bind specifically to certain amino acids. In case of the molecular tweezers by group A3 (Schradler), they bind to the basic amino acids, mostly

lysine but also arginine. The GCP and GCI motif by group A1/A10 (Schmuck/Voskuhl) bind to the acidic amino acids aspartate and glutamate.

The main focus in the following chapters is on the one hand to investigate the applicability of UVRR spectroscopy as label-free, sensitive and specific probing tool for the molecular tweezers and the GCI binding motif. On the other hand for GCP, where the general applicability has already been shown, the focus is on improving and expanding the usability of UVRR spectroscopy, especially with regard to autofluorescence generated by the UV excitation.

The first class of the supramolecular binding motifs studied is the molecular tweezers, which so far were not studied by UVRR spectroscopy.

Figure 5.9 shows the UV-absorption spectrum of the molecular tweezers CLR01 in water. The molecular tweezers exhibits absorption in the entire spectral region below 300 nm. A first absorption band can be observed in the region from 250 nm to 300 nm with a maximum around 280 nm. This absorption is attributed to $\pi \rightarrow \pi^*$ transitions of the aromatic rings. Below 250 nm the absorption increases significantly with a maximum around 220 nm, mostly due to transitions which also involve σ orbitals of the organic structure.

In order to get adequate resonance enhancement and not face occlusion of the Raman signal by autofluorescence from aromatic groups, excitation wavelengths below 250 nm seem to be best suited.

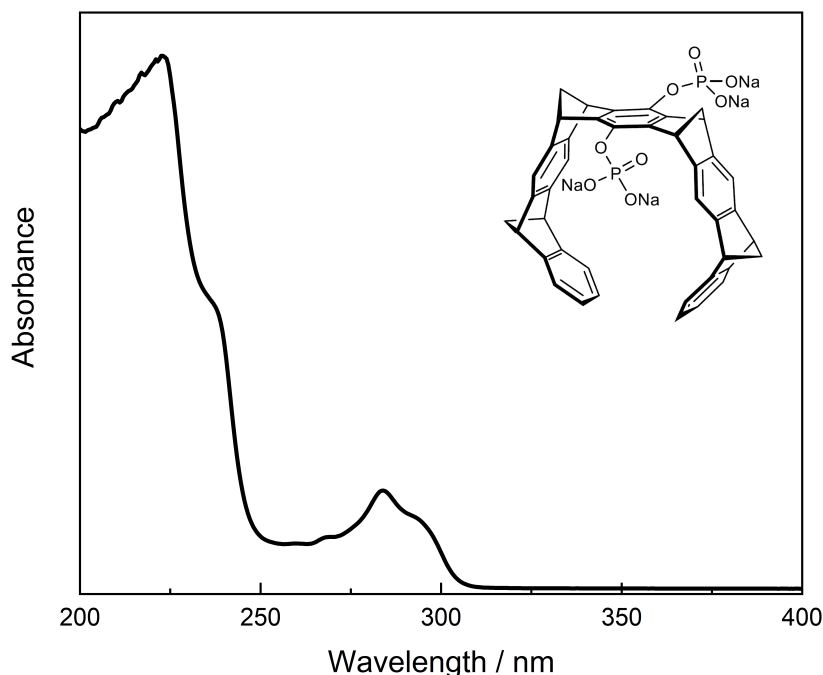


Figure 5.9: UV absorption spectrum of a 500 μM solution of the molecular tweezers CLR01 in water together with the molecular structure of CLR01.

Figure 5.10 shows a UVRR spectrum of a 500 μM solution of the molecular tweezers CLR01 in water measured with a laser excitation wavelength of 244 nm. Four prominent peaks can be observed. The peak at 903 cm^{-1} is associated with norbornadiene stretching, the peak at 1227 cm^{-1} is due to several CH modes across the entire molecule, the peak at 1291 cm^{-1} is mostly due to ring breathing of the central benzene ring to which the phosphates connect. Finally,

the peak at 1604 cm^{-1} is related to ring modes which involve all benzene rings of the molecule.

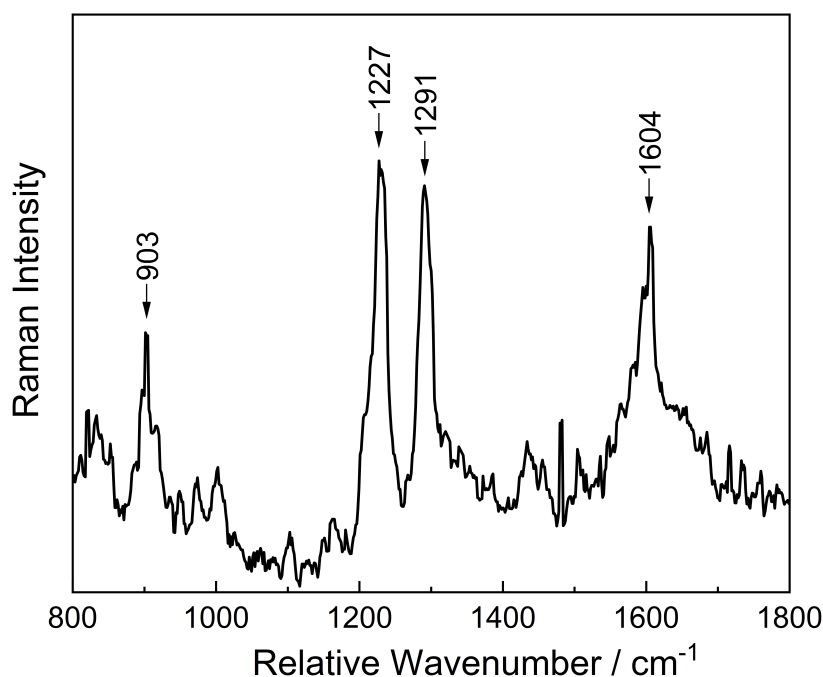


Figure 5.10: UVRR spectrum of the molecular tweezers CLR01 with a concentration of $500\text{ }\mu\text{M}$ in water excited at 244 nm . Prominent peaks marked with the corresponding wavenumber. Taken from reference [75].

Unfortunately, peaks directly associated with the phosphate groups are not observed. This is problematic, as the phosphate groups play a major role for binding. To gauge if it is possible to resolve bands associated with the phosphate groups, the calculated (blue) and experimental (black) Raman spectrum are shown in figure 5.11. Additionally, selected modes either associated with the phosphates or the organic structure of CLR01 are displayed as lines in the spectrum. The match between the experimental and calculated spectrum is reasonably well and corresponding peaks can easily be identified. When taking a special look at the phosphate modes, it can be observed that they are always relatively close to modes from the organic structure and are comparatively small in intensity, especially for the modes around 1034 cm^{-1} . Therefore, monitoring the phosphate modes with normal Raman seems difficult. Unfortunately, UVRR does not seem to be a suitable tool, as the resonance for the phosphate groups is in the deep UV, where also the resonance of peptide and other basic bonds become significant.

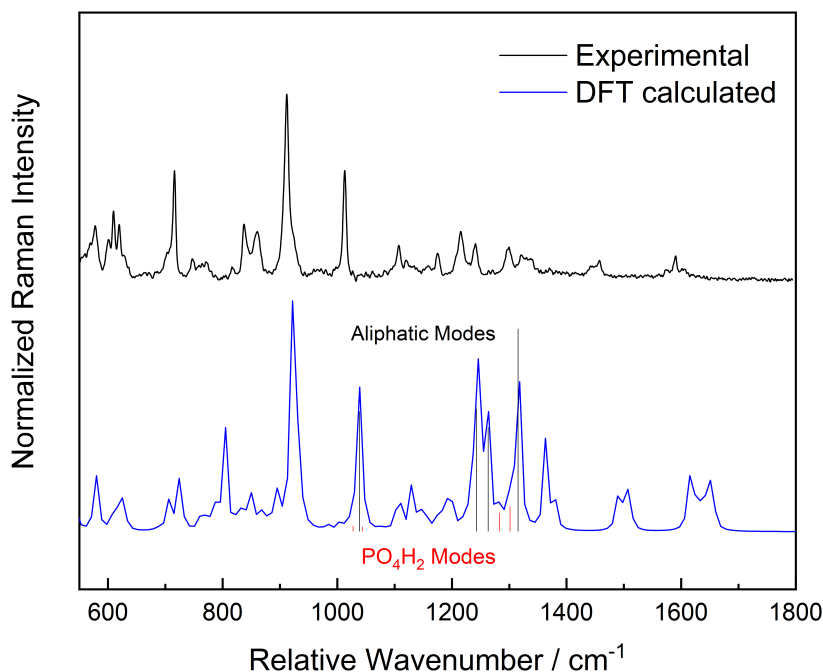


Figure 5.11: Experimental normal Raman spectrum of the molecular tweezers CLR01 in lyophilized form excited at 632.8 nm together with the DFT calculated Raman spectrum of CLR01. Selected eigenmodes associated with the phosphate groups (PO_4H_2) and close-by aliphatic groups are shown as lines with relative intensities in red and black, respectively.

Overall, it was possible to acquire a UVRR spectrum of the molecular tweezers and assign the observed bands to vibrations of the organic structure of the molecule. Unfortunately, no modes related to the phosphate groups were observed in the UVRR spectrum which is most likely to the small Raman activity of the phosphate groups compared to the Raman activity of the organic structure. Since the phosphate groups play a significant role in the binding of the molecular tweezers, the inability of UVRR spectroscopy to detect vibrations associated with the phosphates means that UVRR spectroscopy is not well suited for monitoring the binding of the molecular tweezers.

5.3 UVRR excitation study of GCP-ethylamide

The second class of supramolecular ligands studied in this thesis are based on the guanidiniocarbonyl pyrrole (GCP) binding motif. As a simple test molecule for this ligand class, GCP ethyl amide was examined to test for the optimal excitation wavelength for acquiring UVRR spectra. Figure 5.12 shows the UV-absorption spectrum of a 200 μM GCP ethyl amide solution in the range from 200 nm to 375 nm together with its molecular structure. Two prominent absorption bands are observable in the spectrum with maxima around 215 nm and 298 nm. These bands are attributed to $\pi \rightarrow \pi^*$ electronic transitions of the GCP chromophore. For spectroscopic monitoring of GCP binding to peptides and proteins by UVRR scattering, excitation wavelengths in the region around the 298 nm absorption peak are better suited, since only the aromatic, and not all, amino acids should absorb in this spectral region. The dotted lines in figure 5.12 represent the excitation wavelengths for which UVRR spectra were acquired.

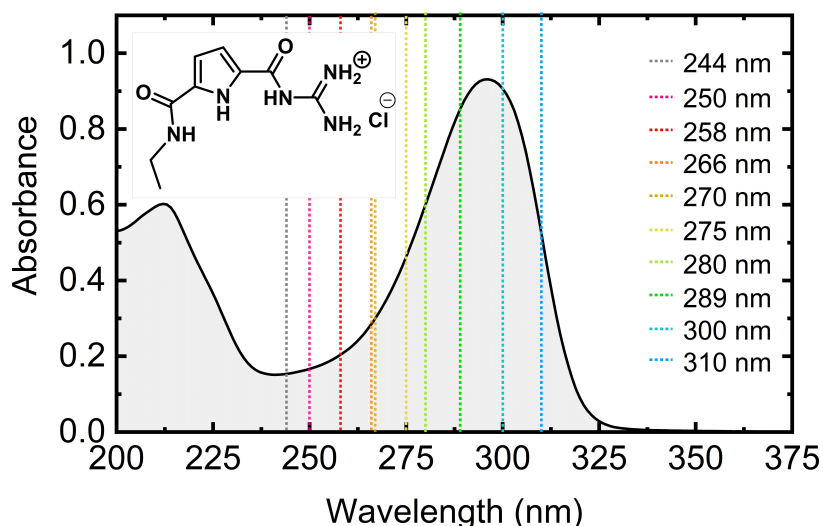


Figure 5.12: UV absorption spectrum of 200 μM GCP ethyl amide in 6 mM BisTris buffer at pH 6. The dotted lines indicate the excitation wavelengths for which UVRR spectra were acquired. The inset shows the molecular structure of GCP ethyl amide. Taken from reference [71].

The corresponding UVRR spectra in the fingerprint region ranging from 800 cm^{-1} to 1800 cm^{-1} are displayed in figure 5.13. The laser power was kept constant for wavelengths between 244 nm and 289 nm. To keep the acquisition time constant and the CCD camera away from saturating, the laser power was lowered for the excitations at 300 nm and 310 nm. For an excitation wavelength of 244 nm, the absorbance as well as the UVRR signal is the lowest. No clear UVRR bands are observed. The broad band around 1640 cm^{-1} is associated with the deformation mode of water molecules present as solvent. However, no fluorescence signal or other significant background is present in the spectrum. Upon increase of the laser excitation wavelength the signal level increases as the absorbance increases as well. Although no clear peaks are observable until a laser excitation wavelength of 266 nm is reached. The peaks observed at 266 nm laser excitation matches peaks observed in other works [9,11,76]. The three peaks in the 900 cm^{-1} to 1100 cm^{-1} region belong to different deformation modes of the pyrrole ring of the GCP motif. The peak at 1400 cm^{-1} is associated to a symmetric ring vibration of the pyrrole. Important for the monitoring of binding is the peak at 1470 cm^{-1} which has contributions from C-N stretching and N-H bending in the guanidinio group and the pyrrole ring. The isolated peak at 1697 cm^{-1} is from a C=O stretch mode of the carbonyl-group connecting the guanidinio group with the pyrrole ring. Another important feature to remark is the background signal that can be observe starting from ca. 1300 cm^{-1} . This already marks the onset of fluorescence signal.

When increasing the excitation wavelength further to 270 nm and 275 nm the UVRR signal is still well resolved, but the background signal is increasing as well. Moving the excitation wavelength even closer towards the resonance condition, the spectral region of the UVRR bands can still be seen, but the signal quality is getting worse as fluorescence is becoming more and more dominant. For excitation wavelengths of 300 nm and 310 nm the UVRR spectrum is completely overtaken by the fluorescence and no Raman signal is observable. Hence, no spectra were taken for even higher excitation wavelengths.

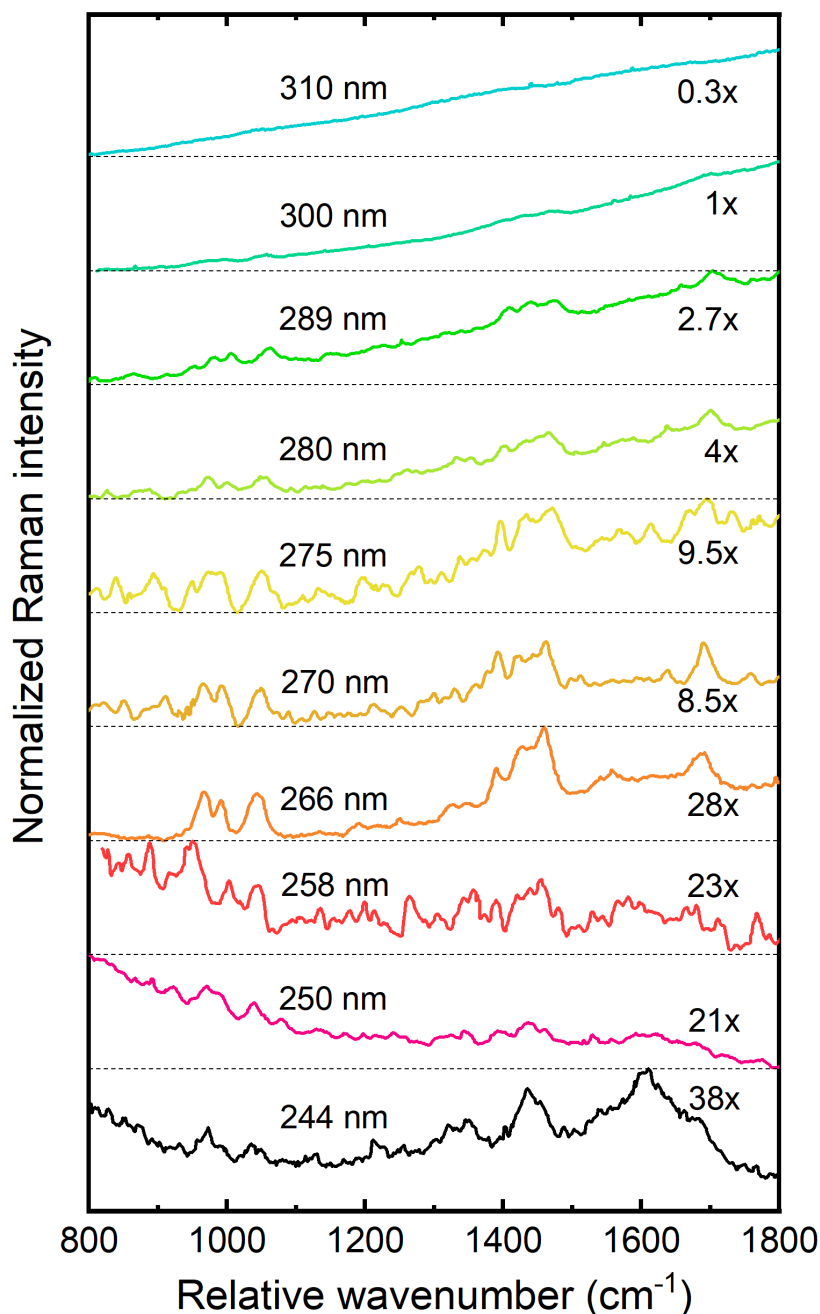


Figure 5.13: UVR spectra of GCP ethyl amide at several laser excitation wavelengths between 244 nm and 310 nm as indicated in figure 5.12. Taken from reference [71].

To sum up the results of the GCP excitation study: the optimal laser excitation wavelength was determined to be at 266 nm. For shorter excitation wavelength the resonance enhancement is too low to acquire good quality UVR spectra. For excitation wavelengths above 275 nm the autofluorescence from the chromophore becomes increasingly dominant and precludes the measurement of good quality UVR spectra as well. This implies that measurement of binding of GCP to proteins is not possible in the present state, as fluorescence from aromatic amino acids will occlude UVR spectrum for laser excitation wavelengths above 260 nm and the use of shorter excitation wavelengths is also not possible, as no or not enough signal enhancement is present for GCP to take spectra with adequate quality. To tend to this problem, there are two options which will be discussed in the following. One is to modify the GCP motif in order to change the optical

properties and have a resonance below 240 nm to get enough resonance enhancement for high quality UVRR spectra. The second option is to employ active fluorescence suppression by means of a Kerr gate in the UV.

5.4 Binding of the carboxylate binder GCI

In the previous chapter it was shown, that in the present state, GCP is unfortunately not ideally suited for binding studies with arbitrary proteins, as the UV-excited autofluorescence from aromatic amino acids and GCP itself can obscure the UVRR signal. In this chapter a new binding motif based on the GCP ligand with different optical properties but ideally the same binding characteristics is studied in order to circumvent the fluorescence problem.

Most of the results discussed in this chapter have been published in reference [24]. Guanidiniocarbonyl indole (GCI) is an analogue to the known GCP binding motif where the pyrrole ring has been substituted by an indole ring. It is expected to have similar binding constants, but with changed optical properties. Figure 5.14 shows the UV-absorption spectrum of 200 μM GCI- and GCP ethyl amide in BisTris buffer. Compared to GCP ethyl amide the absorption bands of GCI ethyl amide are shifted to higher wavelengths, due to the larger conjugate system of the indole ring. The absorption maxima observed at 244 nm and 320 nm (GCP: 215 nm and 298 nm) are assigned to $\pi \rightarrow \pi^*$ transitions. These absorption characteristics should allow for an effective excitation at 244 nm to obtain UVRR spectra without disturbing UV-excited autofluorescence.

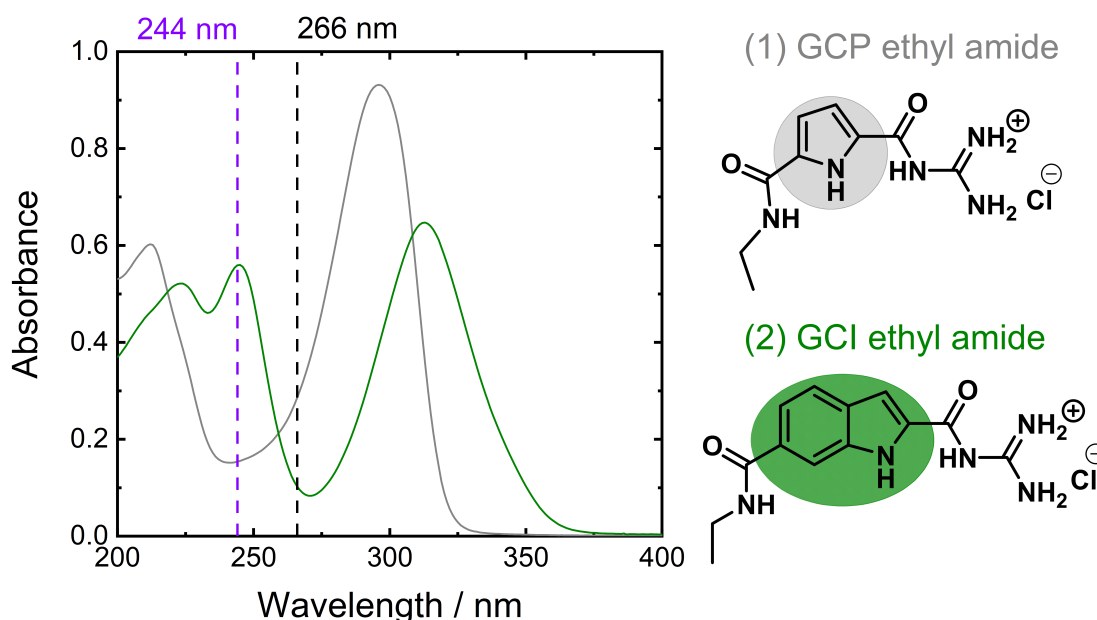


Figure 5.14: UV absorption spectra of GCP ethyl amide (grey) and GCI ethyl amide (green) both for 200 μM solutions in 6 mM BisTris buffer at pH 6, together with their respective schematic molecular structures. The dotted lines indicate the laser excitation wavelengths for which UVRR spectra were acquired. Taken from reference [24].

To vibrationally characterize GCI and test its suitability for UVRR binding studies, UVRR spectra were acquired at 244 nm and 266 nm laser excitation, displayed in figure 5.15. For both excitation

wavelengths several peaks can be observed, with the strongest peak being at 1355 cm^{-1} . As expected from the absorption spectrum, the UVR R signal strength at 266 nm laser excitation wavelength is lower (approximately half the signal compared to 244 nm). Additionally, at 244 nm two additional peaks can be observed at 996 cm^{-1} and 1405 cm^{-1} which are not present in the spectrum excited at 266 nm . Furthermore, the peak at 1490 cm^{-1} is distinctively more pronounced for an excitation wavelength of 244 nm .

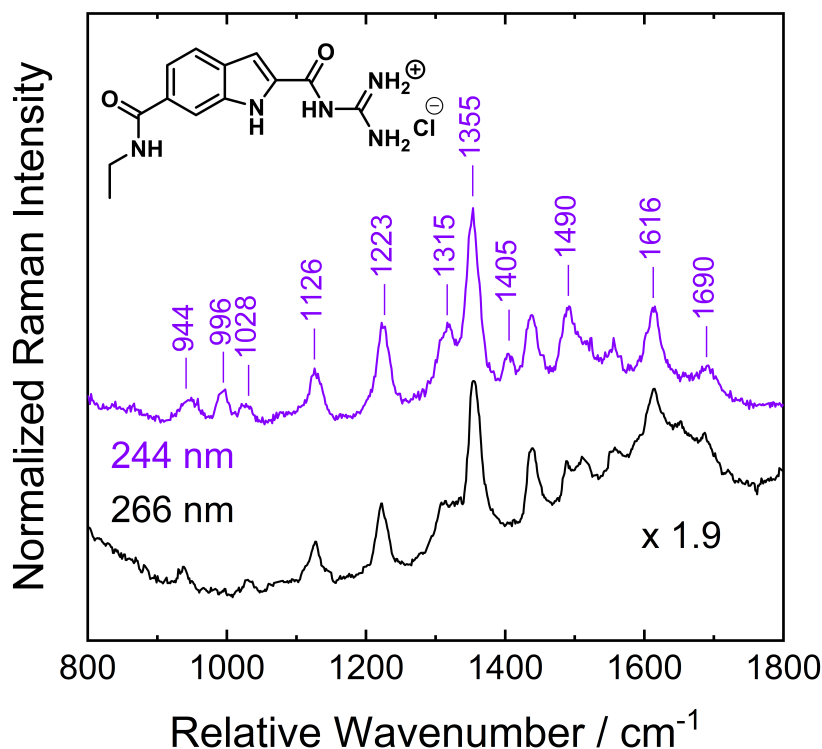


Figure 5.15: UVR R spectra of GCI ethyl amide at $200\text{ }\mu\text{M}$ concentration in 6 mM BisTris buffer at pH 6 excited at 244 nm (violet) and 266 nm (black) together with the schematic molecular structure of GCI ethyl amide. Taken from reference [24].

In order to get a peak assignment of the experimental UVR R spectrum DFT calculations were performed. The calculated normal Raman spectrum and spectral data can be found in appendix B. The peaks were assigned mostly based on wavenumber value of the peak, since only the normal Raman spectrum was calculated. Figure 5.16 shows the calculated eigenvectors of six selected modes at 1035 cm^{-1} (a), 1358 cm^{-1} (b), 1405 cm^{-1} (c), 1502 cm^{-1} (d), 1618 cm^{-1} (e) and 1695 cm^{-1} (f). These modes exhibit involvement of the guanidinio group, which is mainly involved in the supramolecular binding. Hence, upon binding changes are expected mainly for these modes. The mode at 1035 cm^{-1} shows contributions of symmetric C-N stretching and asymmetric N-H bending in form of a rocking motion of the guanidinio group. The mode at 1358 cm^{-1} is an amide III-like mode with C-N stretching and N-H bending located at the guanidinio group. At 1405 cm^{-1} the vibration is a stretching mode of the indole ring with additional N-H bending at the guanidinio group. The mode at 1502 cm^{-1} can be described as in-plane stretch of the indole ring as well as N-H bending across the entire molecule. The mode at 1616 cm^{-1} consist of C-N stretching and N-H bending located solely at th guanidinio group. Finally, the modes at 1695 cm^{-1} is the amide I-like C=O stretch of the carbonyl group connecting the indole ring with

the guanidinio group.

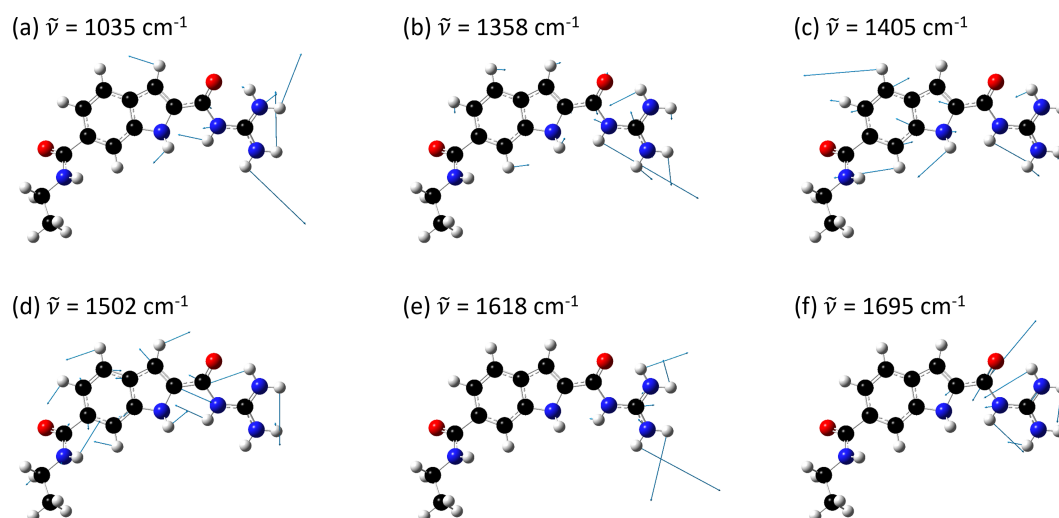


Figure 5.16: DFT calculated eigenvectors of selected eigenmodes of GCI ethyl amide. Taken from reference [24].

In a next step, the suitability for binding studies was evaluated by measuring the UVRR spectra of GCP ethyl amide with two different carboxylates. First, benzoic acid (BA) which serves as an aromatic model system because it is likely to show some resonance Raman enhancement and at higher wavelengths autofluorescence which might inhibit acquiring UVRR spectra. Second, arginylglycylaspartic acid (RGD) as a biologically relevant peptide which is a major amino acid sequence in proteins of the extracellular matrix.

Figure 5.17 shows the UVRR spectrum of a 1:1 mixture of GCI and BA, both at a concentration of 200 μM (blue) together with the neat spectra of GCI (black, bottom) and BA (black, top). The spectrum of the mixture shows similar features as the neat GCI spectrum. However, for some peaks a change in intensity can be observed. The most prominent changes are observed at 1355 cm^{-1} , 1490 cm^{-1} and 1596 cm^{-1} and are marked by dotted lines in the figure. For comparison, the difference spectrum of GCI and the GCI + BA mixture is displayed in the middle. The peak at 1596 cm^{-1} does not belong to a mode of GCI, but is attributed to the ring stretching mode of BA. However, the peaks at 1355 cm^{-1} and 1490 cm^{-1} correspond to previously discussed modes of GCI, which involve C-N stretching and N-H bending of the guanidinio group (cf. figure 5.16 (b) and ring stretching of the indole ring (cf. figure 5.16 (d)), respectively. The observed intensity changes for these two bands indicate binding of the carboxylate of BA by GCI, but since only small changes are observed, the binding is not expected to be particularly strong.

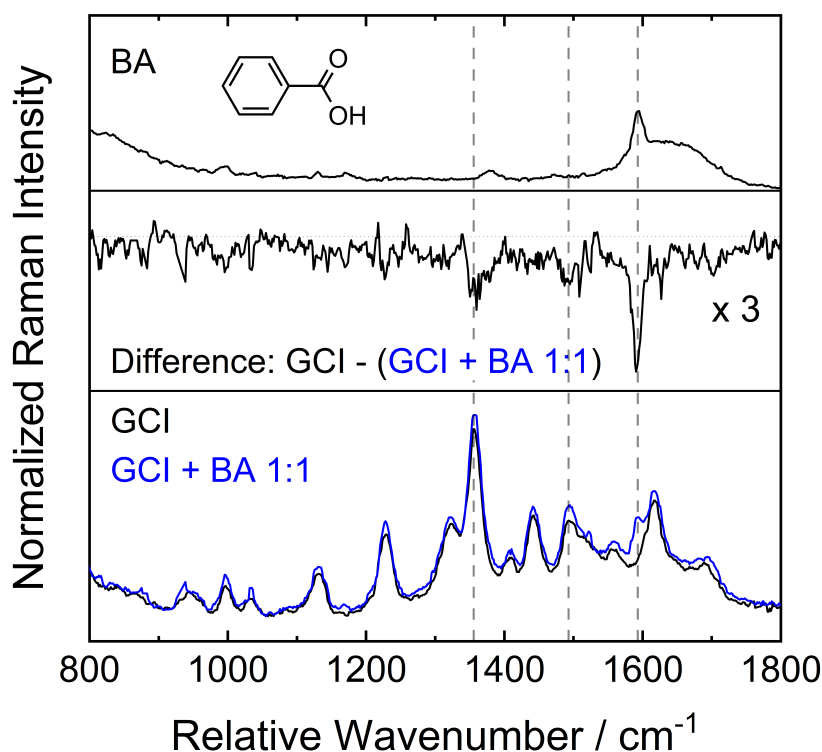


Figure 5.17: UVR spectra of benzoic acid (BA, top) and GCI (black) and a GCI:BA 1:1 mixture (blue) on the bottom. In the middle the corresponding difference spectrum is shown to highlight the changes. The dotted lines indicate the most prominent changes. Taken from reference [24].

The second binding experiment of GCI with RGD is shown in figure 5.18. The 1:1 mixture is displayed in blue whereas the neat spectra of GCI (bottom) and RGD (top) are displayed in black. The RGD spectrum shows no peaks apart from the broad peak around 1640 cm^{-1} attributed to the bending mode of water. This was to be expected since the electronic resonance condition for RGD is well below 244 nm and RGD does not receive any resonance enhancement for an excitation wavelength of 244 nm .

The mixture spectrum shows the same characteristics as the neat GCI spectrum, but several peaks show an increased intensity. The difference spectrum (middle) helps in identifying the peaks which exhibit an intensity increase. Strong peaks are observed at 1033 cm^{-1} , 1120 cm^{-1} , 1225 cm^{-1} , 1310 cm^{-1} , 1355 cm^{-1} , 1405 cm^{-1} , 1450 cm^{-1} , 1501 cm^{-1} , 1616 cm^{-1} , and 1695 cm^{-1} . Many of these peaks belong to the modes described before (cf. figure 5.16), which were expected to be involved in binding. Consequently, the modes associated with the 1120 cm^{-1} , 1225 cm^{-1} , 1310 cm^{-1} and 1450 cm^{-1} peak are also expected to be involved in binding. The stronger intensity changes, as compared to the GCI + BA mixture spectrum, suggest that RGD is a stronger binding partner for GCI than BA. This could be expected, as RGD has two carboxylic groups available for binding whereas BA only has one.

Overall, these two examples show that GCI is a promising candidate to probe supramolecular binding by UVR spectroscopy. GCI can be efficiently excited at 244 nm where the UV-excited autofluorescence of aromatic amino acids does not interfere with the UVR spectrum. Additionally, the mixture spectra show clear changes of peak intensities when a binding partner is present.

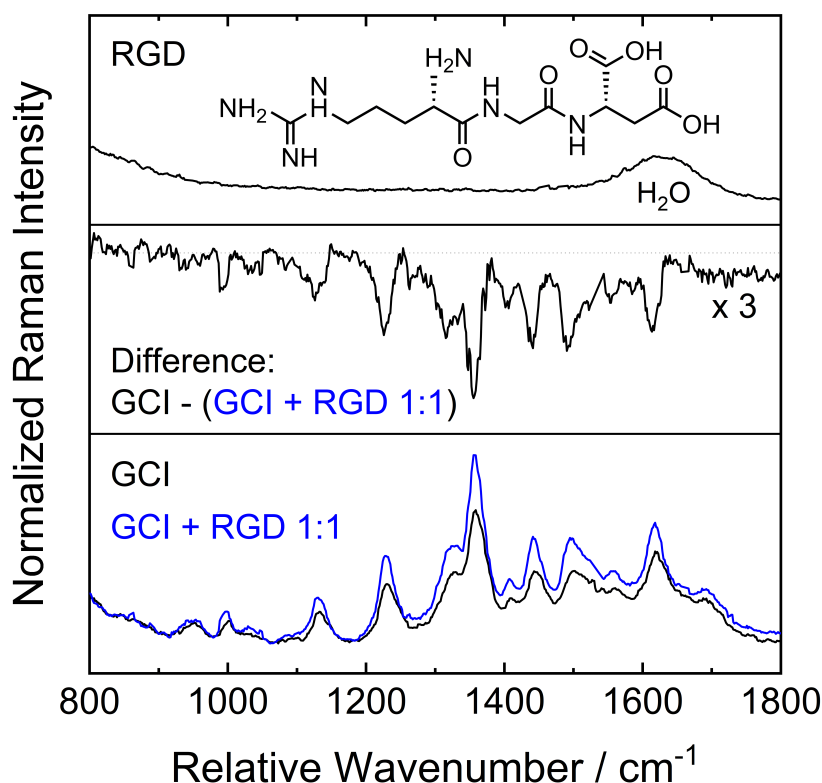


Figure 5.18: UVRR spectra of arginylglycylaspartic acid (RGD, top) and GCI (black) and a GCI:BA 1:1 mixture (blue) on the bottom. In the middle the corresponding difference spectrum is shown to highlight the changes. Taken from reference [24].

5.4.1 Binding studies with the proteins BSA and Survivin

After the initial test of the GCI and the binding to small peptides, the next step is to test the possibility of monitoring the binding to larger biological molecules. Therefore, this chapter deals with preliminary studies of the binding of GCI to two different proteins: bovine serum albumin and Survivin.

UVRR binding studies with proteins faces, in general, two major problems arising from the aromatic amino acids. One is the UV-excited autofluorescence, which has already been mentioned previously. This can be circumnavigated with excitation wavelengths below 250 nm. The other problem arising is the absorption of the aromatic amino acid which starts to rise below 250 nm. The absorption can be in the order of the chromophore which leads to stronger reabsorption of the UVRR scattered light. This can only be compensated by either using lower concentration of protein and chromophoric ligand, which in turn requires high enough Raman activity of the chromophore, or by using longer excitation wavelengths, which necessitates active fluorescence suppression by, for example, a Kerr-gate (cf. 3.2).

The first protein tested for GCI binding is bovine serum albumin (BSA) (PDB: 3V03). BSA consists of 583 amino acids and a molecular weight ca. 66.5 kDa, which is significantly larger than the leucine zipper motive which has been previously studied by UVRR spectroscopy [11]. The second protein studied is Survivin (PDB: 1E31) which is smaller than BSA, with a chain length of 142 amino acid and a molecular weight of ca. 16.5 kDa.

Figure 5.19 shows the UV-absorption spectra of 100 μM solutions of GCI, BSA, and Survivin in HEPES buffer in the range from 200 nm to 400 nm. Both proteins show similar absorption characteristics with a first absorption band between 250 nm and 300 nm and a second stronger absorption band between 250 nm and 200 nm. The absorption maxima are at 232 nm and 279 nm for BSA and at 219 nm and 283 nm for Survivin. These absorption bands correspond mostly to the absorption of tryptophan, which exhibits absorption maxima around 220 nm and 280 nm. As being the larger protein, the absorption of BSA is generally higher than for Survivin. At 244 nm BSA exhibits an absorbance of 0.59 and Survivin has an absorbance of 0.25. This is comparable of to the absorbance of 200 μM solution of GCI at 244 nm of 0.56. Therefore measuring UVRR spectra of GCI mixtures with BSA or Survivin at equal concentrations is expected to exhibit major contributions from proteins. In order to minimize these contributions, the UVRR spectra should be measured with mixtures containing higher equivalents of GCI than protein. At least for the monovalent ligand studied here, this also accounts for the fact that the proteins have multiple possible binding sites, e.g. Survivin has 19 glutamates and 7 aspartates, which together with the C-terminus equals to 27 possible binding sites.

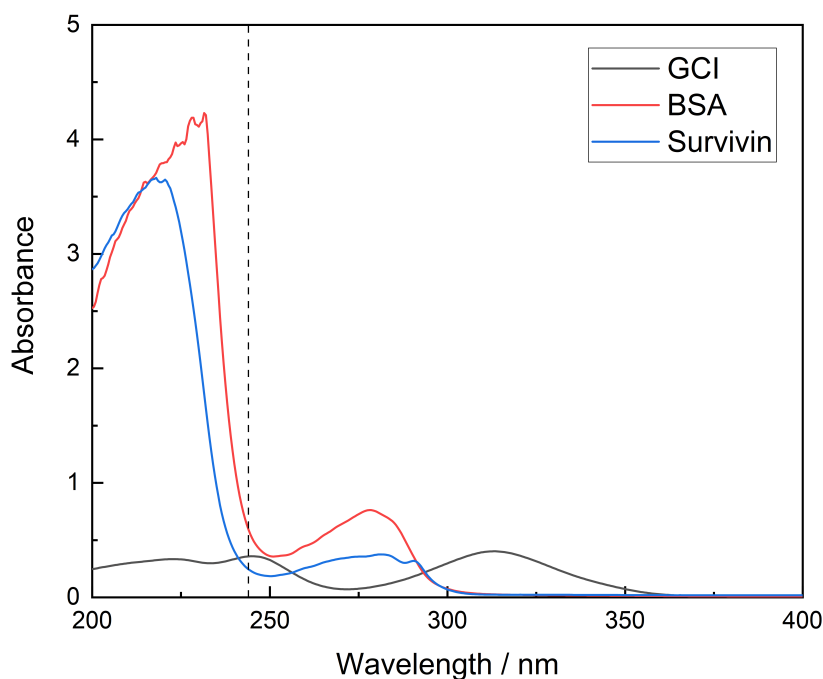


Figure 5.19: UV absorption spectra of GCI ethyl amide, BSA, and Survivin at 100 μM concentration in HEPES buffer at pH 6.5. The dotted line indicates the 244 nm laser excitation wavelength employed for the excitation of UVRR spectra.

The UVRR spectra of GCI (black) and BSA (red) and 4:1 (violet) and 12:1 (blue) mixtures thereof are shown in figure 5.20. The UVRR spectrum of BSA shows several distinctive peaks, with the most prominent being an amide-I peak around 1610 cm^{-1} . Contributions from amide-II and amide-III, observable as the peaks at 1439 cm^{-1} (amide-II) as well as 1334 cm^{-1} and 1167 cm^{-1} (amide-III), is considerably smaller. All of these peaks overlap with peaks in the UVRR spectrum of GCI. Additionally, multiple overlapping peaks are observed around 843 cm^{-1} . For the 4:1 mixture the UVRR spectrum largely resembles the UVRR spectrum of GCI, but the peak at 1355 cm^{-1} is strongly decreased and equal in intensity to the peak at 1315 cm^{-1} . This is in contradiction

to the measurements of the GCI and RGD mixture, where an increase in the intensity of the peaks was observed. Additionally, the intensity of the peak at 1615 cm^{-1} is increased compared to the UVR spectrum of just GCI. The same features are observed for the 12:1 mixture with slightly higher intensity of the peak at 1355 cm^{-1} and lower intensity of the peak at 1615 cm^{-1} . Overall, the signal quality for the mixtures is lower than for the spectra of the single components, with lower signal levels and higher background. This is, however, not observed in the displayed spectra, as they are baseline corrected and normalized to better compare the spectra. Therefore it is not possible to determine if the observed changes are in fact due to binding, or just results of secondary effects such as re-absorption or noise.

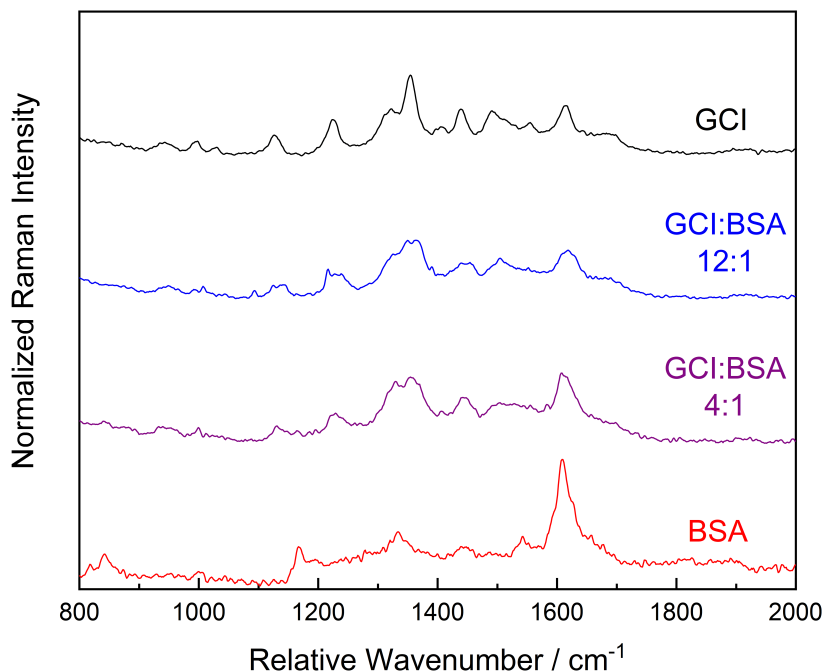


Figure 5.20: UVR spectra of GCI ethyl amide (black) and BSA (red) and of 4:1 (violet) and 12:1 (blue) mixtures of GCI and BSA in HEPES buffer at pH 6.5 excited with 244 nm laser radiation.

Finally, the monitoring the binding of GCI to Survivin with UVR was tested. Figure 5.21 shows the UVR spectra of GCI (black) and Survivin (red) and 14:1 and 104:1 mixtures of thereof. The overall intensity in the UVR spectra of Survivin is significantly lower than for BSA which is most likely simply due to the smaller chain length of Survivin. For Survivin the most prominent peak is again an amide-I peak at 1607 cm^{-1} . Other peaks are observed at 1543 cm^{-1} and 1339 cm^{-1} . The equivalents of the mixture spectra were chosen, so the ratio of GCI to carboxylates is approximately 0.5:1 for the 14:1 and 4:1 for the 104:1 mixture. This titration-like measurement was used to be able to gauge the binding strength and ideally determine a binding constant, if the signal quality is good enough. Both the 14:1 and the 104:1 mixture spectra closely resemble the UVR spectrum of GCI. The intensity of the 14:1 mixture spectrum is slightly lower than the intensity of the GCI spectrum. The spectrum of the 104:1 mixture exhibits intensities equal to that of the pure GCI spectrum. However, it is again not certain, if these minute changes are actually due to binding, or due to stronger re-absorption in the mixture spectra. To be able to confirm, if the observed decrease in intensity is due to binding or not, the experiment will have to be repeated several more times. Although, from the spectroscopy standpoint it might be more promising to directly use

multi-armed ligands, as they are expected to have a stronger UVRR signal, as there are multiple chromophores per molecule. With the higher UVRR signal per molecule, smaller concentrations can be measured and the influence of the protein minimized. However, a multi-armed ligand requires more extensive preparative work from the colleagues from organic chemistry, as the steps in the synthesis are increased. This can significantly lower the availability of such multi-armed ligands.

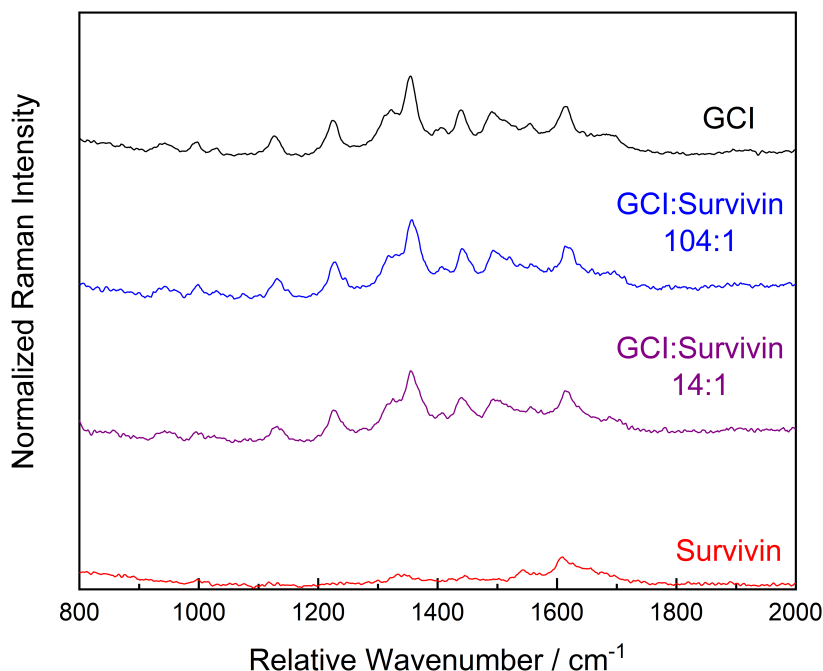


Figure 5.21: UVRR spectra of GCI ethyl amide (black) and Survivin (red) and of 14:1 (violet) and 104:1 (blue) mixtures of GCI and Survivin in HEPES buffer at pH 6.5 excited with 244 nm laser radiation.

5.5 Implementation of a Kerr gate in the UV

In this chapter the other method for the separation of UVRR signal from the autofluorescence mentioned in chapter 5.3, the Kerr gate, is explored. Since the main classes of supramolecular ligands of interest exhibit resonance around 280 nm (molecular tweezer) and 290 nm (GCP), the Kerr gate should optimally work in these spectral ranges.

The Kerr gates which are published so far are restricted mainly to the Vis or higher UV region (> 350 nm, cf. chapter 3.2) but a Kerr gate working in the deeper UV region faces several difficulties. For one, the dispersion has to be carefully considered, as it generally gets stronger for shorter wavelengths and with the temporal gating of the Kerr gate this results in restricted spectral transmission as well. This means mostly reflective optics should be utilized and transmissive optics, which cannot be replaced, should be as optically thin as possible. Therefore wire grid polarizers instead of Glan-Taylor polarizers were chosen for the setup of the Kerr gate, specifically ProFlux UVD240A polarizers from Moxtek were used. These broadband polarizers are only ca. 2.2 mm thick and have a specified contrast ratio, i. e. the ratio of the transmitted intensities in parallel and perpendicular polarization ($CR = \frac{I_{\parallel}}{I_{\perp}}$), of 60 at 260 nm. Additionally, the selection of materials

for the Kerr medium is limited, as only special materials exhibit the required UV transmission. For the Kerr window three different media, fused silica, CaF_2 , and LiF , were tested. Due to the higher damage and white light threshold fused silica proved to be best suited and was used for all experiments.

Figure 5.22 shows the schematic setup of the UV Kerr gate build around the setup described in chapter 4.1. After focusing the laser on the sample, the scattered light is collected in a 90° -geometry with a parabolic collection mirror (CM) with a focal length of $f = 19 \text{ mm}$. The collimated light is polarized horizontally by the first polarizer P1 and focused into the Kerr windows by a parabolic mirror with a focal length of $f = 152.4 \text{ mm}$ (6"). Inside of the Kerr window the scattered light pulse is spatially and temporally overlapped with second laser pulse, the so called Kerr pulse, which is obtained from the second output of the PHAROS laser system ($\lambda = 1030 \text{ nm}$, cf. chapter 4.1). This Kerr pulse will introduce a temporary change of the refractive index of the Kerr window, which consequently turns the polarization of the scattered light which is overlapped with the Kerr pulse. After the Kerr window, the light is recollimated by parabolic mirror PM2 with the same focal length as PM1. The second polarizer P2 is turned perpendicular to P1 and serves as an analyzer. In this way, only the light which is temporally and spatially overlapped with the Kerr pulse and consequently had its polarization changed, should be able to pass the second polarizer P2. Finally, the light is focused into the spectrometer by a third parabolic mirror PM3 with a focal length of $f = 101.6 \text{ mm}$ (4"). The focal length of PM3 was chosen to match the f-number of the spectrometer.

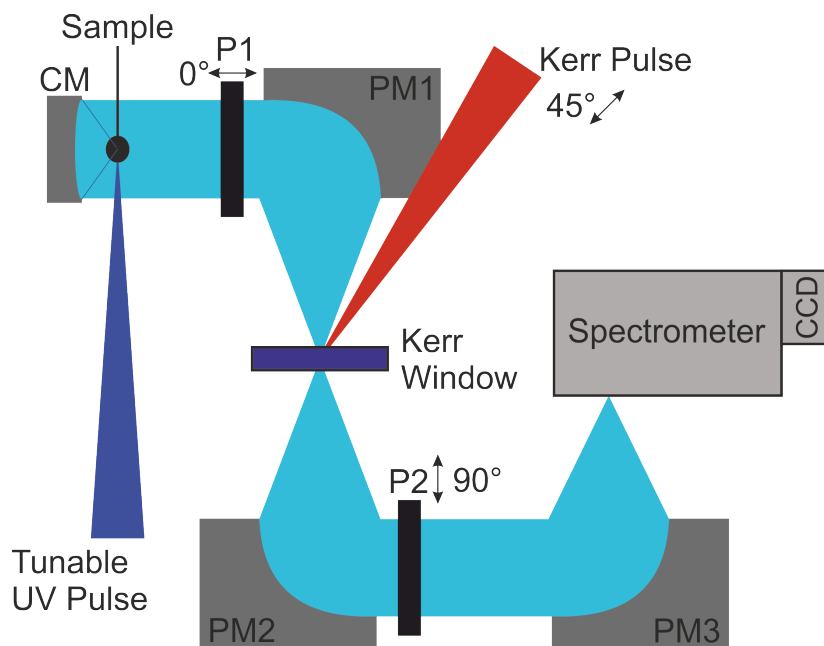


Figure 5.22: Schematic setup of the UV Kerr gate for fluorescence suppression in UVRR; CM: concave mirror; P: wire grid polarizer; PM: parabolic mirror.

To test the performance of the Kerr gate, a solution of ca. 9 mM toluene in acetonitrile (mixture of 1:1000 vol-%) was measured in different states of the Kerr gate. Toluene serves as a model system for a fluorescent aromatic system. Since the polarizers' contrast ratio and transmission decreases with lower wavelengths, the performance only needs to be tested for the lowest wavelength at which it is supposed to operate. Here a wavelength of 280 nm was chosen, as this should allow for

fluorescence suppression when the autofluorescence of GCP becomes relevant (cf. figure 5.13). The measured spectra are shown in figure 5.23. At first the spectrum was acquired with both polarizers in parallel and without the Kerr pulse (green). This essentially means, there is no influence on the acquired spectrum. In this case, the signal intensity is very high (2×10^6 counts), but the spectrum is mostly featureless as expected from fluorescence signal. In the second state, the polarizers are crossed, but the Kerr pulse is still turned off (red), therefore it is also referred to as the "Off" state. This tests the extinction ratio of the crossed polarizers, since without the Kerr pulse there is not temporal discrimination. In this state the signal intensity is lower by a factor of about 1000 (ca. 2000 counts) as compared to the spectrum in the first state but still featureless as expected. The third and final state is the operational or "On" state of the Kerr gate. In this state, the polarizers are crossed and the Kerr pulse is present (blue). For this state, the signal intensity is slightly higher than for state two, but in this case several clear peaks can be observed. The difference between "On"- and "Off"- state is displayed as well (black), in order to see the peaks more clearly. However, the peaks observed are ascribed to the solvent, especially the characteristic $C \equiv N$ peaks around 2250 cm^{-1} , and not to the UV chromophore toluene. Since the remaining autofluorescence still transmitted in the "OFF"-state (red) is still one order of magnitude higher than the Raman signal (black), the autofluorescence suppression efficiency of the Kerr gate in its current state yet needs to be improved by at least one order of magnitude in order to actually be able to measure the UVRR signal of the chromophore.

The necessary improvements could mainly be achieved by polarizers with a higher contrast ratio, since this is the only way to decrease the background signal from the UV-excited autofluorescence (Kerr pulse off in figure 5.23). However, this would most likely require custom designed and made polarizers, which only work in a narrow spectral region (ca. 50 nm) compared to the broadband polarizers used here.

Another way to improve the overall performance of the Kerr gate, is to find a Kerr medium with a non-linear refractive index. In the current state, the optical axis of the gated pulse is not completely turned which leads to a decrease of the transmitted signal (lower intensity in "On-Off" in figure 5.23). A higher non-linear refractive index material would lead to stronger rotation of the optical and thus more transmission of signal.

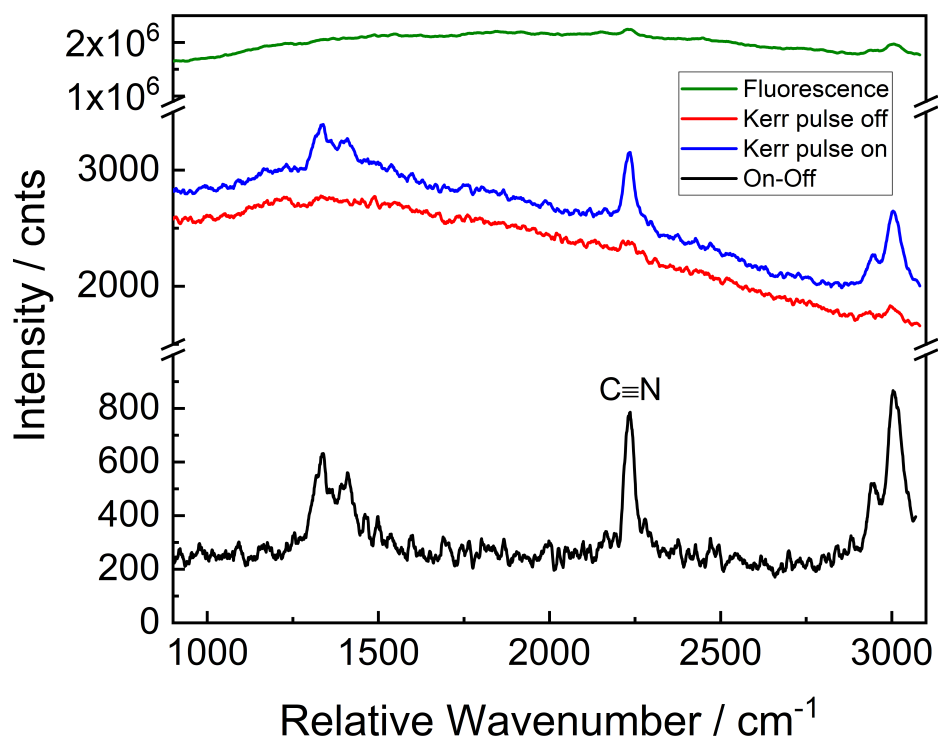


Figure 5.23: Raman spectrum of ≈ 9 mM toluene (UV-fluorescent) in acetonitrile with 280 nm pulsed laser excitation with parallel polarizers (green), crossed polarizer without Kerr pulse (red), crossed polarizers with Kerr pulse (blue) and difference between Kerr pulse on and off (black).

6 Outlook

6.1 UVRR spectroscopy on anthracene

In chapter 5.1 it was shown that we can get a reasonably well agreement of DFT calculated and experimentally acquired UVRR spectra, although for some peaks the intensities still differ considerably. These discrepancies were mostly attributed to difficulties in the proper description of the electronic structure of the highly excited state S_9 . One way to address this issue in the future, is to employ more advanced electronic structure calculations methods such as CASPT2 and EOM-CC. However this will also increase the cost of the calculations.

From the experimental point of view it is more straight forward to simply examine lower excited states, for which the current method is expected to yield better results. Looking at the UV absorption spectrum of anthracene shown in figure 6.1, three distinctive peaks between 380 nm and 325 nm can be observed. The calculations suggest that only the peak at 375 nm is an electronic resonance, namely the $S_0 \rightarrow S_1$ transition, and the other two peaks are due to vibronic coupling. Consequently, excitation studies in the spectral region from 325 nm and 380 nm seem promising to test the currently used DFT calculation methods against experimental UVRR spectra. Additionally, deuterated solvents such as d_3 -acetonitrile or d_{12} -cyclohexane, can be utilized to better separate the solvent peaks from the main anthracene peak around 1400 cm^{-1} .

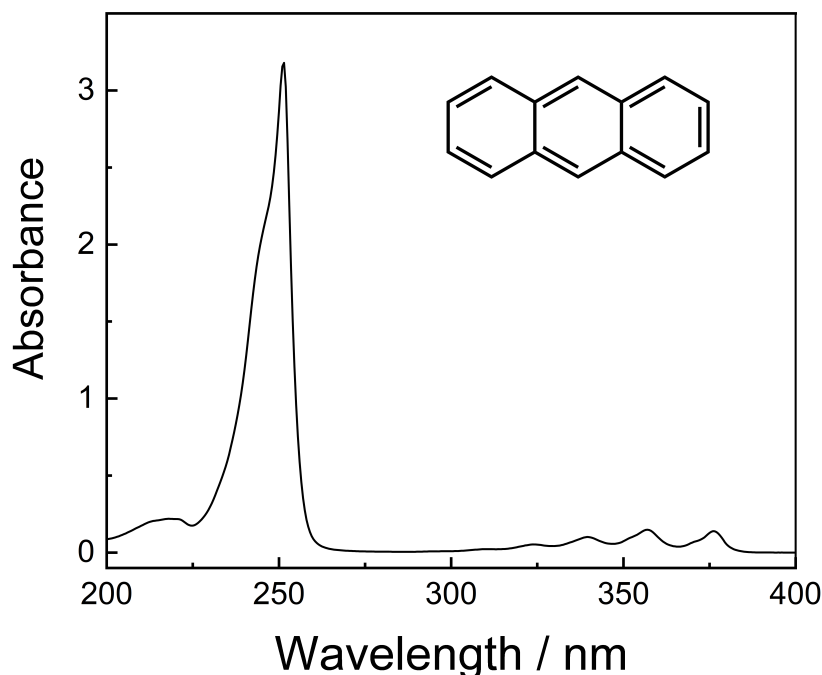


Figure 6.1: UV absorption spectrum of 100 μM anthracene in acetonitrile together with the schematic molecular structure of anthracene.

6.2 IR spectroscopy on molecular tweezers

For the molecular tweezers CLR01 it was unfortunately shown that UVRR spectroscopy is not a suitable method to monitor supramolecular binding. The background measured in UVRR spectroscopy is quite high and the vibrations of the phosphate group, which is crucial in binding, cannot be resolved. Therefore another method has to be found to monitor CLR01 binding. Figure 6.2 shows the DFT calculated and the experimental IR absorption spectrum of CLR01. The calculated spectrum is in the harmonic approximation, therefore the peaks are shifted to higher wavenumber values compared to the experimental peaks. The calculated and experimental spectrum show reasonable agreement and two peaks around 1300 cm^{-1} in the calculated spectrum which are associated with vibrations involving the phosphate group are marked by arrows. These peaks of the phosphates can also be observed in the experimental spectrum. This suggests that IR absorption spectroscopy may be an appropriate method to monitor the supramolecular binding of CLR01.

However, since IR absorption is not selective, there is also signal of the binding partner (proteins) expected in the same spectral region. Thus a sensitive measurement scheme is necessary to observe the expected small changes in the intensity of the phosphate peaks. This should be possible to achieve by direct IR spectroscopy with balanced detection of a two array spectrometer, which can actually be incorporated into the existing setup. An OPA with sequential difference frequency generation can yield tunable pulses in the wavelength range down to $16\text{ }\mu\text{m}$ (625 cm^{-1}) and it can be operated with the beamline which is currently used for the Kerr pulse.

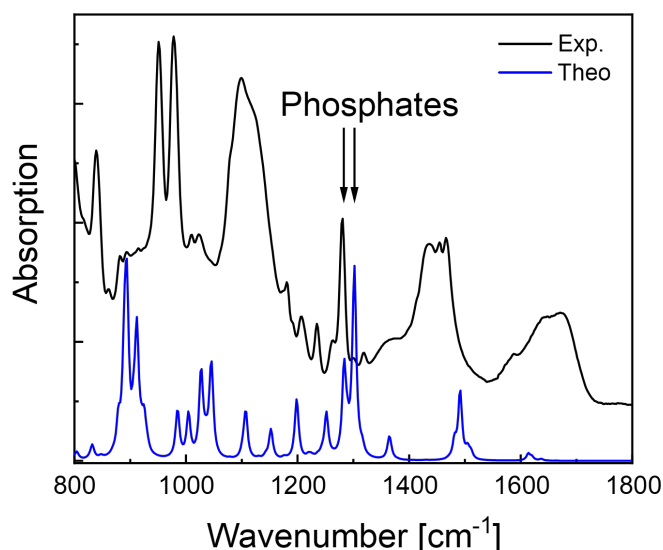


Figure 6.2: DFT calculated (blue) and experimental (black) IR-absorption spectrum of the molecular tweezers CLR01. Selected prominent peaks associated with vibrations of the phosphate group are marked by arrows.

6.3 UV Kerr gate

The proof of concept for a Kerr gate working in the UV at 280 nm could be demonstrated. However, the signal to noise ratio achieved is too low to use it for the monitoring of supramolecular binding. There are two possibilities to improve on the current setup.

The first is to utilize better polarizers for the spectral region of interest. As far as broadband polarizers for the UV are concerned, the used polarizers are the best commercially available polarizers which could be obtained. For a wavelength of 260 nm the contrast ratio is specified to be 60, meanwhile works from Siefke et al. [77] suggest that for custom made narrowband polarizers significantly higher contrast ratios are possible, e.g. circa 800 at 250 nm. The utilization of such custom made polarizers could consequently increase the background- or fluorescence- by at least one order of magnitude.

The second option is to utilize a different Kerr medium. In the current setup the polarization of the gated pulse is not rotated by 90° , which leads to a decrease in transmission. A Kerr medium with a higher non-linear refractive index would yield a higher rotation of the polarization. Interesting candidates are UV-transparent liquids, such as cyclohexane or dioxane, as they regularly exhibit a higher non-linear refractive index as compared to solid media. This is due to a nuclear contribution to the non-linear refractive index in liquids, which is generally larger than the pure electronic contribution observed for solid media. However, for liquid Kerr media nucleation, i. e. the creation of bubbles at the focus, is a limiting factor for the laser intensity which can be used, similar to the white light and damage threshold for solid media.

7 Summary

This thesis was focused on employing UV resonance Raman (UVR) spectroscopy as a powerful vibrational spectroscopic tool to monitor the binding of artificial supramolecular ligands. While the guanidiniocarbonyl pyrrole (GCP) ligand has already been previously studied with great success, two additional artificial supramolecular ligands, the molecular tweezers CLR01 and guanidiniocarbonyl indole (GCI), were studied. The main focus was on exploring two ways to deal with UV-excited autofluorescence, which can easily exceed the UVR signal in strength. Two ways to remedy the autofluorescence issue were explored with the help of a pulsed tunable laser system: spectral separation by shifting the laser excitation wavelength and temporal separation by a so called Kerr gate. Since all UVR studies rely on a proper assignment of the vibrational modes, the current methods for calculating UVR spectra by means of time dependent density functional theory (TD-DFT) were tested against a model molecule anthracene.

To this end, a comparative study between TD-DFT calculated and experimental UVR spectra of anthracene was carried out. Excited at 251 nm (S_0 to S_9 transition), the UVR spectrum exhibits several peaks, with the most dominant being at 1401 cm^{-1} and 751 cm^{-1} and smaller peaks at 1255 cm^{-1} and 1556 cm^{-1} . While all these peaks are also observable in the normal Raman spectrum, an additional peak is observed at 1791 cm^{-1} . To achieve reasonable agreement between experiment and theory, the calculations have to consider the full Herzberg-Teller vibronic coupling (FCHT) and not only the Franck-Condon (FC) terms. Anharmonic corrections have to be included for good agreement in the wavenumber position of less than 4 cm^{-1} as compared to more than 30 cm^{-1} in the harmonic approximation. The peak around 1791 cm^{-1} is also reproduced when allowing a second vibrational quantum to be present in the calculations revealing it as a combination mode. Considering that only a double- ζ basis set (SNSD) and B3LYP functional was utilized for the calculations, the agreement between calculated and measured UVR spectra is quite good. However, there is still considerable mismatch in the relative intensities for certain modes, for example, the pronounced peak around 751 cm^{-1} is underestimated in the calculations. This could be due to a poor description of the higher excited state S_9 , which in general can be problematic in TD-DFT calculations. In future studies, the $S_0 \rightarrow S_1$ with an excitation wavelength of ca. 375 nm could be examined in order to test if the description of the electronic state is problematic. Additionally, UVR spectra were acquired with laser excitation wavelength scanning across the resonance from 244 nm to 253 nm and compared to calculations. In this case, the experimental as well as the calculated spectra show an increase in certain bands for post-resonant excitation, where the wavenumber of the enhanced band (ω_{enh}) roughly coincides with difference in excitation (ω) and resonance (ω_0) frequency ($\omega - \omega_0 = \omega_{enh}$).

After this initial study of the possibilities of DFT for calculating UVR spectra, the focus was shifted to the artificial supramolecular ligands. At first the molecular tweezers CLR01 were studied. An autofluorescence-free UVR spectrum of CLR01 was acquired with a laser

excitation wavelength of 244 nm and Raman bands at 903 cm^{-1} , 1227 cm^{-1} , 1291 cm^{-1} , and 1604 cm^{-1} could be observed. DFT calculations reveal all these bands to be associated with vibrations of the organic backbone of CLR01. Unfortunately, no bands connected to vibrations of the phosphate groups, which are expected to show more pronounced changes upon binding, could be observed. This makes UVRR spectroscopy seem unsuited to monitor binding of CLR01, however, in the IR spectrum strong bands assigned to the phosphate groups are observed around 1280 cm^{-1} . This can be used as a starting point to use IR spectroscopy, as an alternative vibrational spectroscopic technique, to monitor binding, similar to how it has already been employed for GCP in reference [10].

For GCP ethyl amide an excitation study was carried out with laser excitation wavelengths between 244 nm and 310 nm in order to determine an optimal laser excitation wavelength to achieve a strong UVRR signal with little to no influence from autofluorescence of the ligand. Below 266 nm the resonance enhancement is not sufficient to acquire clear UVRR spectra. Between 266 nm and 275 nm a clear UVRR signal is observable with little influence from autofluorescence, mostly in the wavenumber region above 1300 cm^{-1} . The best signal to background ratio is achieved for a laser excitation wavelength of 266 nm. From 280 nm to 289 nm there is still a discernible UVRR signal, however, it is dominated by the autofluorescence. For laser excitation wavelengths above 289 nm, only the autofluorescence signal can be observed. This implies that for the GCP ligand binding studies with laser excitation wavelengths below the aromatic autofluorescence limit are not possible. Therefore, either chemical changes to GCP are necessary in order to change the optical properties to allow for efficient excitation below to aromatic autofluorescence, or a means of active fluorescence suppression like a Kerr gate. Both were explored in this thesis.

First, a chemically modified version of GCP was studied for which the pyrrole in GCP was exchanged with an indole: guanidiniocarbonyl indole (GCI). The absorption bands of GCI are red-shifted to 244 nm and 320 nm as compared to 215 nm and 298 nm for GCP, while the binding pocket is largely unchanged. With an excitation wavelength of 244 nm a virtually background-free UVRR spectrum of GCI ethyl amid was acquired with several observable bands. From DFT calculations, six vibrational modes could be assigned, which involve the binding pocket. Therefore the modes at 1028 cm^{-1} , 1355 cm^{-1} , 1405 cm^{-1} , 1490 cm^{-1} , 1616 cm^{-1} , and 1690 cm^{-1} are expected to change upon binding. To test which changes are induced upon binding, mixtures with two different binding partners were examined. First, with benzoic acid, as a model system for an aromatic binding partner, and second, with the tripeptide RGD, as a model for a biological peptide. For both binding partners 1:1 mixture spectra with GCI ethyl amide were acquired and compared to the UVRR spectra of GCI ethyl amide and the respective neat binding partner. The UVRR spectrum of the mixture exhibited a small increase in the peak intensity for most bands, most pronounced for the band at 1355 cm^{-1} and 1490 cm^{-1} . For the mixture with RGD stronger changes compared to the benzoic acid mixture were observed across the entire spectrum, which is most likely due to the availability of two carboxy groups for binding in RGD as compared to the one of benzoic acid.

Additionally, preliminary binding tests with the proteins bovine serum albumin and Survivin were carried out with a laser excitation wavelength of 244 nm. Both proteins show resonance enhancements themselves for a laser excitation wavelength of 244 nm, where the UVRR spectrum

is dominated by amide-I like band around 1610 cm^{-1} . For both proteins, mixture spectra with GCI ethyl amide exhibit small intensity changes, compared to the neat GCI ethyl amide spectrum. However, contrary to the test with benzoic acid and RGD, the intensity is decreasing and it is unclear if these changes are simply due to stronger reabsorption because of the proteins. Multi-armed ligands could improve this problem in future studies, as they should yield a stronger signal per molecule which would allow for measurements at lower concentrations, minimizing the influence of reabsorption.

Lastly, a Kerr gate operating in the UV spectral region was setup to reject the disturbing autofluorescence. The Kerr gate was constructed with two wire grid UV broadband polarizers and fused silica as the Kerr medium. All other optics were reflective optics in order to minimize dispersion. The Kerr gate was demonstrated for an excitation wavelength of 280 nm and a approximately 9 mM mixture of toluene in acetonitrile was excited. For parallel polarizers, a fluorescence signal from toluene was measured with ca. 6 million counts. For crossed polarizers the fluorescence signal decreases to ca 2 000 counts, which means an extinction of ca. 1000 is achieved with the polarizers. In operation, with the Kerr-pulse present, Raman bands can be observed with ca. 600 counts signal strength. However, the Raman bands are assigned to the solvent acetonitrile and not the analyte toluene, as the extinction ratio is not high enough at 280 nm. Consequently, the extinction is likely not high enough for application to supramolecular ligands. The extinction could in the future be improved with custom designed and built narrowband polarizers. Additionally, the use of a different Kerr medium with higher non-linear refractive index could improve the transmittance of the instantaneous Raman signals, thus increasing the signal to noise ratio. This should allow for autofluorescence-free measurements with arbitrary laser excitation wavelengths and arbitrary binding partners.

8 Bibliography

- [1] Suckling, C. J. *Experientia* **1991**, *47*, 1139–1148.
- [2] Jimenez, R.; Salazar, G.; Baldrige, K.; Romesberg, F. *Proc. Natl. Acad. Sci.* **2003**, *100*, 92–97.
- [3] Pawson, T.; Nash, P. *Genes Dev.* **2000**, *14*, 1027–1047.
- [4] Schmidtchen, F. P.; Berger, M. *Chem. Rev.* **1997**, *97*, 5, 1609–1646.
- [5] Lehn, J.-M. *Acc. Chem. Res.* **1978**, *11*, 2, 49–57.
- [6] Schmuck, C. *Chem. Commun.* **1999**, 843–844.
- [7] Fokkens, M.; Schrader, T.; Klärner, F.-G. *J. AM. Chem. Soc.* **2005**, *127*, 14415–14421.
- [8] Küstner, B.; Schmuck, C.; Wich, P. R.; Jehn, C.; Srivastava, S. K.; Schlücker, S. *Phys. Chem. Chem. Phys.* **2007**, 4598–4603.
- [9] Niebling, S.; Kuchelmeister, H. Y.; Schmuck, C.; Schlücker, S. *Chem. Commun.* **2011**, *47*, 568–570.
- [10] Niebling, S.; Kuchelmeister, H. Y.; Schmuck, C.; Schlücker, S. *Chem. Sci.* **2012**, *3*, 3371.
- [11] Zakeri, B.; Niebling, S.; Martínéz, A. G.; Sokkar, P.; Sanchez-Garcia, E.; Schmuck, C.; Schlücker, S. *Phys. Chem. Chem. Phys.* **2018**, *20*, 1817–1820.
- [12] Teale, F. W. J.; Weber, G. **1957**, 476–482.
- [13] Fischer, E. *Ber. Dtsch. Chem. Ges.* **1894**, *27*, 2985–2993.
- [14] Koshland Jr., D. E. *Proc. Natl. Acad. Sci. U.S.A.* **1958**, *44*, 2, 98–104.
- [15] Lehn, J.-M. *Science* **1985**, 4689.
- [16] Moreira, I. S.; Fernandes, P. A.; Ramos, M. J. *Proteins* **2007**, *68*, 803–812.
- [17] Giese, M.; Niemeyer, J.; Voskuhl, J. *ChemPlusChem* **2020**, *85*, 985–997.
- [18] Moiania, D.; Cavallotti, C.; Famulari, A.; Schmuck, C. *Chem. Eur. J.* **2008**, *14*, 5207–5219.
- [19] Rether, C.; Sicking, W.; Boese, R.; Schmuck, C. *Beilstein J. Org. Chem.* **2010**, *6*, 3.
- [20] Rether, C.; Schmuck, C. *Eur. J. Org. Chem.* **2011**, *2011*, 1459–1466.
- [21] Schmuck, C.; Wienand, W. *J. Am. Chem. Soc.* **2003**, *125*, 452–459.

- [22] Schmuck, C.; Heil, M. *Org. Biomol. Chem.* **2003**, *1*, 633–636.
- [23] Vallet, C.; Aschmann, D.; Beuck, C.; Killa, M.; Meiners, A.; Mertel, M.; Ehlers, M.; Bayer, P.; Schmuck, C.; Giese, M.; Knauer, S. K. *Angew. Chem. Int. Ed.* **2020**, *59*, 5567–5571.
- [24] Holtum, T.; Kumar, V.; Sebens, D.; Voskuhl, J.; Schlücker, S. *Beilstein J. Org. Chem.* **2020**, *16*, 2911–2919.
- [25] Schrader, T.; Bitan, G.; Klärner, F.-G. *Chem. Commun.* **2016**, *52*, 11318–11334.
- [26] Bier, D.; R., R.; Bravo-Rodriguez, K.; Bartel, M.; Ramirez-Anguaita, J. M.; Dutt, S.; Wilch, C.; Klärner, F.-G.; Sanchez-Garcia, E. Schrader, T.; Ottmann, C. *Nat. Chem.* **2013**, *5*, 234–239.
- [27] Bier, D.; Mittal, S.; Bravo-Rodriguez, K.; Sowislok, A.; Guillory, X.; Briels, J.; Heid, C.; Bartel, M.; Wettig, B.; Brunsveld, L.; Sanchez-Garcia, E.; Schrader, T.; Ottmann, C. *J. Am. Chem. Soc.* **2017**, *139*, 16256–16263.
- [28] Li, Z.; Siddique, I.; Hadrovic, I.; Kirupakaran, A.; Li, J.; Zhang, Y.; Klärner, F.-G.; Schrader, T.; Bitan, G. *Commun. Biol.* **2021**, *14*, 1076.
- [29] Meiners, A.; Bäcker, S.; Hadrovic, I.; Hied, C.; Beuck, C.; Ruiz-Blanco, Y. B.; Mieres-Perez, J.; Pörschle, M.; Grad, J.-N.; Vallet, C.; Hoffman, D.; Bayer, C.; Sanchez-Garcia, E.; Schrader, T.; Knauer, S. K. *Nat. Commun.* **2021**, *12*, 1505.
- [30] Smekal, A. *Naturwissenschaften* **1923**, *11*, 873–875.
- [31] Raman, C.; Kroshnan, K. *Nature* **1928**, *121*, 501–502.
- [32] Long, D. A. *The Raman effect: A unified treatment of the theory of Raman scattering by molecules*; Wiley Chichester and New York, **2002**.
- [33] Herzberg, G.; Teller, E. *Z. Phys. Chem.* **1933**, *B21*, 410–446.
- [34] Albrecht, A. C. *J. Chem. Phys.* **1961**, *34*, 1476–1484.
- [35] Franck, J. *Trans. Faraday Soc.* **1926**, *21*, 536–542.
- [36] Condon, E. *Phys. Rev.* **1926**, *28*, 1182–1201.
- [37] Kerr, J. *Lond. Edinb. Dublin Philos. Mag. J. Sci.* **1875**, *50*, 332, 337–348.
- [38] Simpson, G. J. *Nonlinear Optical Polarization Analysis in Chemistry and Biology*; Cambridge University Press Cambridge, **2017**.
- [39] Boyd, R. W. *Nonlinear Optics*; Academic Press Cambridge, **2008**.
- [40] Maker, P. D.; Terhune, R. W. *Phys. Rev.* **1965**, *137*, 3A, 802–818.
- [41] Armstrong, J. A.; Bloembergen, N.; Ducuing, J.; S., P. P. *Phys. Rev.* **1962**, *127*, 6, 1918–1939.

- [42] Hellwarth, R. W.; Owyong, A.; George, N. *Phys. Rev. A* **1971**, *4*, 6, 2342–2347.
- [43] Owyong, A.; Hellwarth, R. W.; George, N. *Phys. Rev. B* **1972**, *5*, 2, 628–633.
- [44] Hellwarth, R.; Cherlow, J.; Yang, T.-T. *Phys. Rev. B* **1975**, *11*, 2, 964–967.
- [45] López-Peña, I.; Leigh, B. S.; Schlamadinger, D. E.; Kim, J. E. *Biochemistry* **2015**, *54*, 4770–4783.
- [46] Sanchez, K. M.; Kang, G.; Wu, B.; Kim, J. E. *Biophys. J.* **2011**, *100*, 2121–2130.
- [47] Sattasathuchana, T.; Siegel, J. S.; Baldrige, K. K. *J. Chem. Theory Comput.* **2020**, *16*, 4521–4532.
- [48] Niebling, S.; Srivastava, S. K.; Herrmann, C.; Wich, P. R.; Schmuck, C.; Schlücker, S. *Chem. Commun.* **2010**, *46*, 2133–2135.
- [49] Guillory, X.; Hadrovic, I.; de Vink, P. J.; Sowislok, A.; Brunsveld, L.; Schrader, T.; Ottmann, C. *J. Am. Chem. Soc.* **2021**, *143*, 34, 13495–13500.
- [50] Lakowicz, J. R. *Principles of Fluorescence Spectroscopy*; Springer Boston, MA, **2006**.
- [51] Matousek, P.; Towrie, M.; Stanley, A.; Parker, A. W. *Appl. Spectrosc.* **1999**, *53*, 12, 1485–1489.
- [52] Appavoo, K.; Sfeir, M. Y. *Rev. Sci. Instrum.* **2014**, *85*, 055114.
- [53] Blake, J. C.; Nieto-Pescador, J.; Li, Z.; Gundlach, L. *Opt. Lett.* **2016**, *41*, 2462–2465.
- [54] Matousek, P.; Towrie, M.; Ma, C.; Kwok, W. M.; Phillips, D.; Toner, W. T.; Parker, A. W. *J. Raman Spectrosc.* **2001**, *32*, 983–988.
- [55] Wang, L. M.; Ho, P. P.; Alfano, R. R. *Appl. Opt.* **1993**, *32*, 4, 535–540.
- [56] Grosch, H.; Fateev, A.; Clausen, S. *J. Quant. Spectrosc. Radiat.* **2015**, *154*, 28–34.
- [57] Kabaciński, P.; Kardaś, M.; Stepanenko, Y.; Radzewicz, C. *Opt. Express* **2019**, *27*, 8, 11018–11028.
- [58] Adair, R.; Chase, L. L.; Payne, S. A. *Phys. Rev. B* **1989**, *39*, 5, 3337–3350.
- [59] Yu, Z.; Gundlach, L.; Piotrowiak, P. *Opt. Lett.* **2011**, *36*, 15, 2904–2906.
- [60] Burke, K. *J. Chem. Phys.* **2012**, *136*, 150901.
- [61] Frisch, M. J. *et al.* “Gaussian 16 Revision C.01”, **2016** Gaussian Inc. Wallingford CT.
- [62] Burke, K.; Werschnik, J.; Gross, E. K. U. *J. Chem. Phys.* **2005**, *123*, 062206.
- [63] Santoro, F.; Lami, A.; Imbrota, R.; Bloino, J.; Barone, V. *J. Chem. Phys.* **2008**, *128*, 224311.
- [64] Santoro, F.; Cappelli, C.; Barone, V. *J. Chem. Theory Comput.* **2011**, *7*, 1824–1839.

- [65] Egidi, F.; Bloino, J.; Cappelli, C.; Barone, V. *J. Chem. Theory Comput.* **2014**, *10*, 346–363.
- [66] Baiardi, A.; Bloino, J.; Barone, V. *J. Chem. Phys.* **2014**, *141*, 114108.
- [67] Bloino, J.; Baiardi, A.; Biczysko, M. *Int. J. of Quantum Chem.* **2016**, *116*, 1543–1574.
- [68] Duschinsky, F. *Acta Physicochim. URSS* **1937**, *7*, 551.
- [69] Santoro, F.; Improta, R.; Lami, A.; Bloino, J.; Barone, V. *J. Chem. Phys.* **2007**, *126*, 084509.
- [70] Bloino, J.; Biczysko, M.; Santoro, F.; Barone, V. *J. Chem. Theory Comput.* **2010**, *6*, 1256–1274.
- [71] Kumar, V.; Holtum, T.; Sebena, D.; Giese, M.; Voskuhl, J.; Schlücker, S. *Spectrochim. Acta A* **2021**, 119359.
- [72] “Double and triple- ζ basis sets of SNS family. Available at: <https://smart.sns.it/?pag=download>”, .
- [73] Shimanouchi, T. *Tables of Molecular Vibrational Frequencies Consolidated Volume I*; National Bureau of Standards , **1972**.
- [74] Holtum, T.; Bloino, J.; Pappas, C.; Kumar, V.; Barone, V.; Schlücker, S. *J. Raman Spectrosc.* **2021**, *52*, 2292–2300.
- [75] Kumar, V.; Holtum, T.; Voskuhl, J.; Giese, M.; Schrader, T.; Schlücker, S. *Spectrochim. Acta A* **2021**, *254*, 119622.
- [76] Srivastava, S. K.; Niebling, S.; Küstner, B.; Wich, P. R.; Schmuck, C.; Schlücker, S. *Phys. Chem. Chem. Phys.* **2008**, *10*, 6770–6775.
- [77] Siefke, T.; Kroker, S.; Pfeiffer, K.; Puffky, O.; Dietrich, K.; Franta, D.; Ohlidal, I.; Szeghalmi, A.; Kley, E.-B.; Tünnermann, A. *Adv. Opt. Mater.* **2016**, *4*, 1780–1786.

Appendix A

Example for calculating resonance Raman spectra with Gaussian

Here example files for calculating resonance Raman spectra with the Gaussian 16 program package are given for anthracene. The scripts assume already optimized structures, thus the scripts for structure optimization are omitted. In this example the SNSD basis set and B3LYP functional are used.

At first, the Raman spectrum of the ground state is calculated:

```
%nprocshared=12
%mem=20GB
%chk=\anthracene.freq1.chk
# freq=(raman,savenormalmodes) b3lyp/gen geom=connectivity 6D
```

```
anthracene.freq

0 1
C      3.66006200    0.71290100   -0.00002300
C      2.47870800    1.40615900    0.00006200
C      1.22350000    0.72167800    0.00002500
C      1.22350100   -0.72167900    0.00003000
C      2.47870900   -1.40615900   -0.00002600
C      3.66006300   -0.71289700   -0.00007700
C      0.00000000    1.40230200    0.00002900
C      0.00000100   -1.40230300    0.00003700
C     -1.22349900   -0.72168000    0.00002900
C     -1.22350100    0.72167700    0.00000400
C     -2.47870800    1.40616000   -0.00002800
H     -2.47750700    2.49352200   -0.00007300
C     -3.66006300    0.71290000   -0.00006800
C     -3.66006200   -0.71289900   -0.00000900
C     -2.47870900   -1.40616000    0.00003600
H     -0.00000700    2.49046800    0.00005800
H     4.60628500    1.24682300   -0.00005700
H     2.47750400    2.49352200    0.00011900
H     2.47750700   -2.49352100   -0.00003200
H     4.60628000   -1.24683000   -0.00014100
H     -0.00000500   -2.49047000    0.00005200
H     -4.60628200    1.24682900   -0.00010900
H     -4.60628100   -1.24682700   -0.00003000
H     -2.47751100   -2.49352200    0.00008500

1 2 2.0 6 1.5 17 1.0
2 3 1.5 18 1.0
3 4 1.5 7 1.5
4 5 1.5 8 1.5
5 6 2.0 19 1.0
6 20 1.0
7 10 1.5 16 1.0
8 9 1.5 21 1.0
9 10 1.5 15 1.5
10 11 1.5
11 12 1.0 13 2.0
12
13 14 1.5 22 1.0
14 15 2.0 23 1.0
15 24 1.0
16
17
18
```

```

19
20
21
22
23
24

-H 0
6-31++G
P 1 1.00      0.000000000000
   0.7500000000D+00  0.10000000D+01
P 1 1.00      0.000000000000
   0.1450000000D+00  0.10000000D+01
****
-C 0
6-31G
S 1 1.00      0.000000000000
   0.7500000000D+01  0.1000000000D+01
SP 1 1.00      0.000000000000
   0.5000000000D-01  0.1000000000D+01
D 1 1.00      0.000000000000
   0.8200000000D+00  0.1000000000D+01
D 1 1.00      0.000000000000
   0.3180000000D+00  0.1000000000D+01
****
-N 0
6-31G
S 1 1.00      0.000000000000
   0.1260000000D+02  0.1000000000D+01
SP 1 1.00      0.000000000000
   0.5300000000D-01  0.1000000000D+01
D 1 1.00      0.000000000000
   0.1015000000D+01  0.1000000000D+01
D 1 1.00      0.000000000000
   0.1500000000D+00  0.10000000D+01
****
-O 0
6-31G
S 1 1.00      0.000000000000
   0.1510000000D+02  0.1000000000D+01
SP 1 1.00      0.000000000000
   0.6500000000D-01  0.1000000000D+01
D 1 1.00      0.000000000000
   0.1190000000D+01  0.1000000000D+01
D 1 1.00      0.000000000000
   0.1800000000D+00  0.1000000000D+01
****

```

Then in a second step, the eigenmodes of the excited state of interest, here S_9 , are calculated:

```

%nprocshared=12
%mem=20GB
%chk=\anthracene_td_freq9.chk
# freq=savenormalmodes td=(root=9) b3lyp/gen geom=connectivity 6D

```

anthracene.TD_freq9

```

0 1
C      3.68397800  -0.71519600  -0.00000100
C      2.48676700  -1.41272100  -0.00000600
C      1.23538700  -0.73245800  -0.00000300
C      1.23538700   0.73245800   0.00000100
C      2.48676700   1.41272100   0.00000800
C      3.68397800   0.71519500   0.00000800
C      0.00000000  -1.41355000  -0.00000200
C      0.00000000   1.41355000  -0.00000200
C     -1.23538700   0.73245800  -0.00000400
C     -1.23538700  -0.73245800   0.00000000
C     -2.48676700  -1.41272100   0.00000600
H     -2.48790300  -2.50049700   0.00001100
C     -3.68397800  -0.71519600   0.00000500
C     -3.68397800   0.71519500  -0.00000400
C     -2.48676700   1.41272100  -0.00000800
H      0.00000000  -2.50178700  -0.00000200
H      4.62822700  -1.25248700  -0.00000200
H      2.48790300  -2.50049700  -0.00001000
H      2.48790400   2.50049700   0.00001500
H      4.62822800   1.25248600   0.00001300
H      0.00000000   2.50178800  -0.00000200
H     -4.62822700  -1.25248700   0.00001100
H     -4.62822800   1.25248600  -0.00000600
H     -2.48790400   2.50049700  -0.00001300

```

```

1 2 2.0 6 1.5 17 1.0
2 3 1.5 18 1.0
3 4 1.0 7 1.5
4 5 1.5 8 1.5
5 6 2.0 19 1.0
6 20 1.0
7 10 1.5 16 1.0
8 9 1.5 21 1.0
9 10 1.0 15 1.5
10 11 1.5
11 12 1.0 13 2.0
12
13 14 1.5 22 1.0
14 15 2.0 23 1.0
15 24 1.0
16
17
18
19
20
21
22
23
24

-H 0
6-31++G
P 1 1.00 0.000000000000
0.7500000000D+00 0.10000000D+01
P 1 1.00 0.000000000000
0.1450000000D+00 0.10000000D+01
****
-C 0
6-31G
S 1 1.00 0.000000000000
0.7500000000D+01 0.1000000000D+01
SP 1 1.00 0.000000000000
0.5000000000D-01 0.1000000000D+01
D 1 1.00 0.000000000000
0.8200000000D+00 0.1000000000D+01
D 1 1.00
0.3180000000D+00 0.1000000000D+01
****
-N 0
6-31G
S 1 1.00 0.000000000000
0.1260000000D+02 0.1000000000D+01
SP 1 1.00 0.000000000000
0.5300000000D-01 0.1000000000D+01
D 1 1.00 0.000000000000
0.1015000000D+01 0.1000000000D+01
D 1 1.00 0.000000000000
0.1500000000D+00 0.10000000D+01
****
-O 0
6-31G
S 1 1.00
0.1510000000D+02 0.1000000000D+01
SP 1 1.00 0.000000000000
0.6500000000D-01 0.1000000000D+01
D 1 1.00 0.000000000000
0.1190000000D+01 0.1000000000D+01
D 1 1.00 0.000000000000
0.1800000000D+00 0.1000000000D+01
****

```

Finally, the resonance Raman spectrum is calculated based on both the checkpoint files from the previous calculations:

```

%nprocshared=12
%mem=20GB
%Chk=anthracene_freq1.chk !checkpoint file of the ground state
# freq=(FC,ReadFC,ReadFCHT) b3lyp/gen geom=AllCheck 6D

TimeIndependent
Spectroscopy=ResonanceRaman
Spectrum=(Lower=0.,Upper=2000.,Broadening=50) !relative wavenumber range of the calculated spectrum
Intermediate=Source=Chk
RR=(OmegaMin=39000,OmegaMax=40000,OmegaStep=100) !desired excitation frequencies in absolute wavenumber, at resonance if no values are

```

Appendix A Example for calculating resonance Raman spectra with Gaussian

anthracene_td_freq9.chk !checkpoint file of the excited state

```
0 1
C      3.66006200   0.71290100  -0.00002300
C      2.47870800   1.40615900   0.00006200
C      1.22350000   0.72167800   0.00002500
C      1.22350100  -0.72167900   0.00003000
C      2.47870900  -1.40615900  -0.00002600
C      3.66006300  -0.71289700  -0.00007700
C      0.00000000   1.40230200   0.00002900
C      0.00000100  -1.40230300   0.00003700
C     -1.22349900  -0.72168000   0.00002900
C     -1.22350100   0.72167700   0.00000400
C     -2.47870800   1.40616000  -0.00002800
H     -2.47750700   2.49352200  -0.00007300
C     -3.66006300   0.71290000  -0.00006800
C     -3.66006200  -0.71289900  -0.00000900
C     -2.47870900  -1.40616000   0.00003600
H     -0.00000700   2.49046800   0.00005800
H      4.60628500   1.24682300  -0.00005700
H      2.47750400   2.49352200   0.00011900
H      2.47750700  -2.49352100  -0.00003200
H      4.60628000  -1.24683000  -0.00014100
H     -0.00000500  -2.49047000   0.00005200
H     -4.60628200   1.24682900  -0.00010900
H     -4.60628100  -1.24682700  -0.00003000
H     -2.47751100  -2.49352200   0.00008500
```

```
1 2 2.0 6 1.5 17 1.0
2 3 1.5 18 1.0
3 4 1.5 7 1.5
4 5 1.5 8 1.5
5 6 2.0 19 1.0
6 20 1.0
7 10 1.5 16 1.0
8 9 1.5 21 1.0
9 10 1.5 15 1.5
10 11 1.5
11 12 1.0 13 2.0
12
13 14 1.5 22 1.0
14 15 2.0 23 1.0
15 24 1.0
16
17
18
19
20
21
22
23
24
```

-H 0

6-31++G

```
P 1 1.00 0.000000000000
   0.7500000000D+00 0.10000000D+01
P 1 1.00 0.000000000000
   0.1450000000D+00 0.10000000D+01
```

-C 0

6-31G

```
S 1 1.00 0.000000000000
   0.7500000000D+01 0.1000000000D+01
SP 1 1.00 0.000000000000
   0.5000000000D-01 0.1000000000D+01
D 1 1.00 0.000000000000
   0.8200000000D+00 0.1000000000D+01
D 1 1.00
   0.3180000000D+00 0.1000000000D+01
```

-N 0

6-31G

```
S 1 1.00 0.000000000000
   0.1260000000D+02 0.1000000000D+01
SP 1 1.00 0.000000000000
   0.5300000000D-01 0.1000000000D+01
D 1 1.00 0.000000000000
   0.1015000000D+01 0.1000000000D+01
D 1 1.00 0.000000000000
   0.1500000000D+00 0.10000000D+01
```

```
-O 0
6-31G
S 1 1.00
  0.1510000000D+02 0.1000000000D+01
SP 1 1.00 0.0000000000
  0.6500000000D-01 0.1000000000D+01
D 1 1.00 0.0000000000
  0.1190000000D+01 0.1000000000D+01
D 1 1.00 0.0000000000
  0.1800000000D+00 0.1000000000D+01
****
```

Appendix B

Calculated normal Raman spectra for GCI

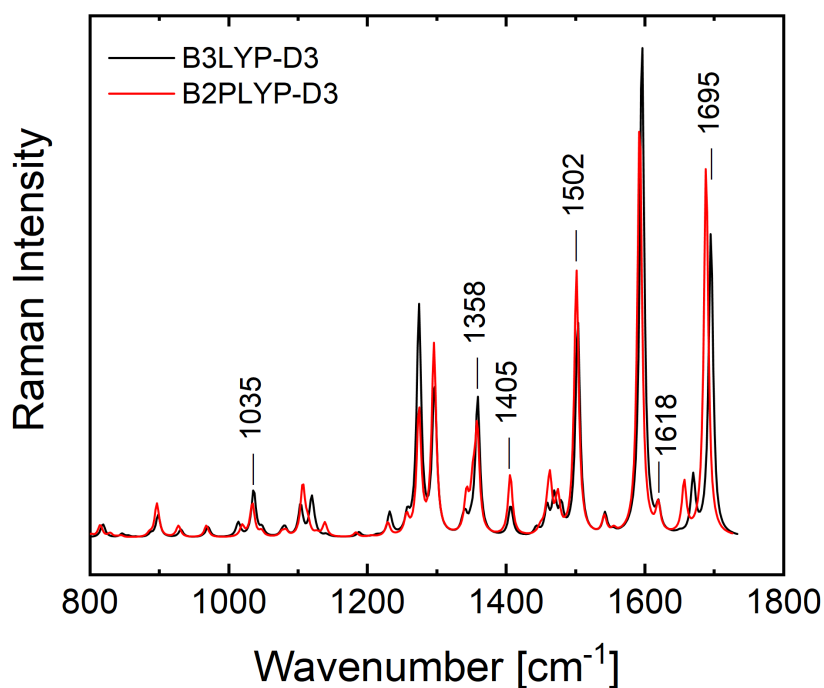


Figure B.1: Computed Raman spectrum of GCI ethyl amide in the fingerprint region 800-1800 cm^{-1} , calculated at the B3LYP-D3/6-311++G(d,p) and B2PLYP-D3/6-311++G(d,p) level of theory. Taken from reference [24].

Table B.1: Calculated Raman spectrum of GCI ethyl amide in the single protonated form. Level of theory: B3LYP-D3/6-311++G(d,p) and B2PLYP-D3/G-311++G(d,p)

Mode	B3LYP-D3		B2PLYP-D3	
	Wavenumber [cm^{-1}]	Raman activity	Wavenumber [cm^{-1}]	Raman activity
1	19.48	1.650	22.56	1.857
2	36.23	2.199	37.39	2.455
3	41.13	2.368	42.92	2.573
4	46.44	3.180	46.89	2.895
5	60.56	1.389	60.66	1.324
6	73.76	1.081	70.48	0.948
7	86.71	1.478	87.15	1.367

Appendix B Calculated normal Raman spectra for GCI

Mode	Wavenumber [cm ⁻¹]	Raman activity	Wavenumber [cm ⁻¹]	Raman activity
8	119.78	0.187	111.99	0.926
9	140.21	2.560	131.24	2.393
10	169.97	1.194	168.00	0.993
11	203.40	0.577	196.19	0.736
12	218.96	4.264	217.09	6.302
13	254.10	6.136	229.33	8.079
14	257.77	0.205	250.85	2.605
15	272.11	2.126	253.84	0.567
16	276.35	0.812	272.22	0.647
17	297.11	2.149	290.47	4.896
18	312.57	6.133	293.77	6.009
19	328.64	1.071	324.94	0.981
20	362.50	1.251	354.45	0.818
21	387.30	2.255	380.69	2.587
22	407.20	4.323	401.72	7.257
23	421.46	2.672	406.81	2.777
24	459.21	2.524	434.76	1.154
25	471.14	1.205	456.26	1.678
26	481.28	11.412	465.27	1.040
27	484.08	9.582	483.51	21.404
28	502.38	5.236	493.68	5.021
29	533.87	2.244	522.52	1.435
30	584.91	2.130	572.50	3.959
31	589.17	4.033	585.82	4.151
32	603.06	7.906	596.31	7.477
33	614.22	4.644	611.77	4.061
34	666.93	29.087	655.34	5.020
35	689.16	6.086	663.70	21.355
36	705.35	8.833	671.54	12.714
37	723.32	1.879	693.78	8.293
38	739.28	0.573	723.94	0.789
39	746.57	2.597	725.57	3.438
40	774.83	16.557	769.92	13.046
41	784.71	4.784	780.33	3.424
42	817.87	11.777	801.62	5.651
43	819.32	15.825	814.89	24.967
44	846.48	7.412	829.19	8.057
45	855.83	2.907	838.54	0.944
46	866.71	1.123	844.94	3.677

Appendix B Calculated normal Raman spectra for GCI

Mode	Wavenumber [cm ⁻¹]	Raman activity	Wavenumber [cm ⁻¹]	Raman activity
47	887.68	6.525	885.87	6.720
48	898.35	45.927	896.60	69.450
49	931.17	15.989	926.07	2.193
50	962.74	0.969	927.82	21.909
51	970.20	22.033	967.93	24.435
52	1013.84	30.355	1019.52	23.145
53	1036.03	100.442	1034.13	72.298
54	1048.10	16.370	1047.45	11.570
55	1076.98	9.311	1076.81	9.791
56	1081.14	18.446	1082.25	12.124
57	1103.62	69.065	1106.82	113.040
58	1119.63	83.512	1113.93	27.110
59	1123.71	9.408	1127.13	6.597
60	1140.56	4.772	1138.65	30.739
61	1187.80	9.951	1183.44	9.895
62	1213.58	2.904	1205.34	2.310
63	1232.10	51.645	1229.34	30.302
64	1257.45	39.564	1256.48	40.743
65	1274.30	512.863	1274.30	282.310
66	1296.71	340.337	1295.87	429.881
67	1337.18	15.908	1342.55	69.137
68	1340.76	37.363	1344.11	18.332
69	1349.29	17.612	1352.06	95.731
70	1358.90	317.856	1358.26	236.080
71	1372.96	0.635	1376.22	0.552
72	1406.46	70.380	1405.92	142.007
73	1442.67	11.561	1448.84	11.242
74	1445.31	7.473	1452.04	7.271
75	1458.79	62.794	1458.73	29.875
76	1465.77	4.625	1462.90	127.130
77	1469.42	85.093	1473.34	11.261
78	1479.42	60.892	1474.55	75.608
79	1503.22	516.891	1501.26	629.622
80	1542.27	49.245	1541.42	42.261
81	1554.53	6.601	1555.04	10.480
82	1595.78	1213.020	1592.44	1018.563
83	1619.38	58.509	1619.18	67.806
84	1649.87	3.792	1655.08	6.583
85	1669.50	140.290	1656.61	120.609

Appendix B Calculated normal Raman spectra for GCI

Mode	Wavenumber [cm ⁻¹]	Raman activity	Wavenumber [cm ⁻¹]	Raman activity
86	1695.06	755.304	1688.11	923.291
87	2913.48	276.720	2928.48	194.390
88	2914.39	112.570	2933.32	158.137
89	2969.10	62.663	2989.04	66.470
90	2995.96	149.947	3013.22	61.384
91	2997.05	45.912	3015.20	108.538
92	3063.23	50.762	3071.45	51.893
93	3073.02	90.382	3081.17	86.851
94	3092.48	151.471	3099.40	155.391
95	3129.27	72.422	3133.62	72.461
96	3263.04	91.461	3285.21	124.052
97	3445.49	32.851	3446.00	40.914
98	3460.42	44.814	3456.11	55.482
99	3463.26	134.171	3467.97	122.943
100	3483.90	65.572	3485.52	66.280
101	3525.30	81.355	3534.45	68.328
102	3570.94	63.089	3580.53	55.943

Acknowledgments

First, I would like to thank Prof. Dr. Sebastian Schlücker for the opportunity to work in his group, as well as all the constructive discussions and other support which made this work possible.

Also I would like to thank my co-supervisor Prof. Dr. Thomas Schrader for his help with his deep knowledge and enthusiasm for supramolecular chemistry.

My sincere thanks are also to the CRC 1093 for providing a great framework and fruitful collaborations. I want to especially thank my collaboration partners from organic chemistry Daniel Sebena and Philipp Rebmann and from biology, Annika Meiners and Alexander Höing.

I also want to thank all current and former members of the AG Schlücker for all the fruitful discussions and the help I received from all of you at one time or another. A special mention here for our unofficial „astrophysics“ group which consisted of Thomas Keller, Vikas Kumar, Sebastian Küpper and Jesil Jose, for all the discussions about the universe and pretty much everything else. Lastly a special thanks to Roland Grzeschik for having the patients to read and correct (not only) my thesis.

Curriculum Vitae

The CV is not included in the online version due to data privacy limitations.

Der Lebenslauf ist in der Online-Version aus Gründen des Datenschutzes nicht enthalten.

Publications

Holtum, T.; Bloino, J.; Pappas, C.; Kumar, V.; Barone, V.; Schlücker, S. „Ultraviolet resonance Raman spectroscopy of anthracene: Experiment and theory“ *J. Raman Spectrosc.*, **2021**, 52, 2292-2300.

Kumar, V.; Holtum, T.; Voskuhl, J.; Giese, M.; Schrader, T.; Schlücker, S. „Prospects of ultraviolet resonance Raman spectroscopy in supramolecular chemistry on proteins“ *Spectrochim. Acta A*, **2021**, 254, 119622.

Kumar, V.; Holtum, T.; Sebens, D.; Giese, M.; Voskuhl, J.; Schlücker, S. „Ultraviolet resonance Raman spectroscopy with a continuously tunable picosecond laser: Application to the supramolecular ligand guanidiniocarbonyl pyrrole (GCP)“ *Spectrochim. Acta A*, **2021**, 250, 119359.

Holtum, T.; Kumar, V.; Sebens, D.; Voskuhl, J.; Schlücker, S. „UV resonance Raman spectroscopy of the supramolecular ligand guanidiniocarbonyl indole (GCI) with 244 nm laser excitation“ *Beilstein J. Org. Chem.*, **2020**, 16, 2911-2919.

Grzeschik, R.; Schäfer, D.; Holtum, T.; Küpper, S.; Hoffmann, A.; Schlücker, S. „On the Overlooked Critical Role of the pH Value on the Kinetics of the 4-Nitrophenol NaBH₄-Reduction Catalyzed by Noble-Metal Nanoparticles (Pt, Pd, and Au) “ *J. Phys. Chem.*, **2020**, 124, 2939-2944.

Kalupka, C.; Holtum, T.; Reininghaus, M. „Ultrafast dynamics of material excitation of dielectrics with ultrashort pulsed Bessel beams“ *Proc. SPIE 10520*, **2018**, Laser-based Micro- and Nanoprocessing XII, 105200G.

Reininghaus, M.; Kalupka, C.; Faley, O.; Holtum, T.; Finger, J.; Stampfer, C. „Dynamics of ultrashort pulsed laser radiation induced non-thermal ablation of graphite“ *Appl. Phys. A*, **2014**, 117, 1873-1878.

Conference contributions

- 2021 CRC 1093 4th Graduate Student Symposium (Poster + Talk)
- 2021 CRC 1093 4th International Symposium (Poster)
- 2021 International conference on advanced vibrational spectroscopy (ICAVS) (Flash presentation)
- 2019 CRC 1093 3rd International Symposium (Poster)